Novel Mixed Conducting Oxides for Solid Oxide Fuel Cells (SOFC's) Applications

Thesis submitted in accordance with the requirements of the University of Liverpool for the degree of Doctor in Philosophy

by

Carlos Bernuy-López.

August 2008

A mis abuelos, en especial a
Luis y Carmen, quienes lucharon
para que yo llegara hasta aquí.

Abstract

This thesis describes the search for new mixed conductors as potential anodes and cathodes for applications in Solid Oxide Fuel Cells.

Several compounds have been synthesised and characterised by means of different diffraction techniques (X-Rays, neutrons and electrons), high resolution electron microscopy and electrical measurements (AC Impedance Spectroscopy and DC resistivity measurements).

Chapter 3 describes a study of $Sr_2MgMoO_{6-\delta}$ which is shown to adopt a $\sqrt{2}\ a_p \times \sqrt{2}\ a_p \times 2\ a_p$ superstructure of the simple perovskite cell, derived from an $a^0a^0c^-$ tilt system via distortion of the Mg- and Mo-centred octahedra. It is also shown that the reduction of $Sr_2MgMoO_{6-\delta}$ appears to be correlated with antisite disorder at either point or extended anti-phase defects. In chapter 4, it is shown that $Sr_2MgMoO_{6-\delta}$ undergoes a phase transition at high temperature (200-300 °C) from a triclinic $I\bar{1}$ structure to a cubic $Fm\bar{3}m$ one. Upon reduction above 900 °C, $Sr_2MgMoO_{6-\delta}$ begins to decompose into a reduced material modelled as an n = 2 R-P phase $Sr_3(Mg_xMo_{1-x})_2O_{7-\delta}$. Chapter 5 describes attempts to synthesise this phase which were ultimately unsuccessful though it was produced as the majority phase ($Sr_3Mg_{0.5}Mo_{1.5}O_{7-\delta}$) in the presence of $Sr_2MgMoO_{6-\delta}$ and the pseudo-perovskite $Sr_{11}Mo_4O_{23}$. High resolution electron microscopy (HREM) showed the presence of numerous defects in the n = 2 R-P phase matrix. In chapter 6, $Sr_{11}Mo_4O_{23}$ was reported as a new pseudo-perovskite type structure phase which seems to adopt a complex triclinic structure at room temperature and HREM showed the presence of numerous defects and twining phenomena which could explains the complexity of this structure. It was also shown to undergo a structural transition at 600 °C to a cubic $Fd\bar{3}m$ structure. The material is an ionic conductor over the 500-600 °C temperature range, affording an oxide ion conductivity of 10^{-3} S cm^{-1}.

Chapter 7, investigates doping in the system $La_{1+x}Sr_{1-x}Ni_xAl_{1-x}O_4$ for values $0 \leq x \leq 0.2$. $La_{1.1}Sr_{0.9}Ni_{0.1}Al_{0.9}O_4$ (LSNAO_0.1) and $La_{1.2}Sr_{0.8}Ni_{0.2}Al_{0.8}O_4$ (LSNAO_0.2) adopt an I4/mmm tetragonal structure. Both materials were shown to be electric conductors with only a very low ionic contribution. Finally in Chapter 8 the synthesis of both $Bi_8Cr_7O_{22.5}$ and $Bi_{17}Cr_8Sr_7O_{44.5}$ is presented. These are described as fluorite-type structure with numerous extended defects in their structure. $Bi_8Cr_7O_{22.5}$ was shown to be an electrical conductor without any ionic contribution and $Bi_{17}Cr_8Sr_7O_{44.5}$ was shown to have a small ionic contribution to the overall conductivity at 453 °C.

Contents

List of Figures

List of Tables

Acknowledgments

This thesis has been carried out between the University of Liverpool (UK) and the "Laboratoire" CRISMAT-CNRS in Caen (France) under the support of the European Commission and under the Marie Curie Early Stage Researcher Training initiative (MEST-CT2004/51437 (NOVELOX)).

First of all, I would like to thank John B. Claridge, Denis Pelloquin, Matthew J. Rosseinsky and Bernard Raveau who have given me the opportunity to introduce myself in the Solid State Chemistry world. Matt and Bernard, thank you to give me the opportunity to carry out my PhD between ones of the best laboratories in Europe. Thank you for your support, your smart ideas and comments. John and Denis, thank you for your daily support, encourage and patience in so many moments when, for instance, "John, this refinement doesn't work..." or "Denis, le microscope ne marche pas...": Muchas gracias!

This thesis would not have been possible to carry out without all the advices of many postdoctoral researchers and permanent researchers who have given me the opportunity to broad my knowledge during my thesis. Thanks to Xiaojun and Honjun for their advices and help with the Impedance Spectroscopy; Craig for his help with the glove box and Amy for her kindness every time.

I would also like to thank other people who have given me all their help and support when it was necessary. Thanks Barbara and Marie France for all their help in every moment; Rob for his efficiency with the

instrumentation every time; Phillipe pour son aide avec les microscopes et Marie, Delphine, Sylvie et Laurence pour leur aide à la salle de manipulations.

Then, I would like to thank all the people I have met in Liverpool. Thanks to Laurent, Stephen, Romain, Calum, Phil, Ben, Alexy, Lei, Lili, Gary, Chris,... Thanks to all the family from the "Norfolk and Good" team: Vaidhya, Foggy, Andrew, Rob, Jamie (thanks for the "crazy" nights), Mike (thanks for your squash lessons), Mathieu and Matthew. Aussi merci beaucoup à Jean-Noel pour sa bonne humeur en tout moment (a poil !).

También quería acordarme de mi particular "Spanish Liverpool". Quería agradecer a Jorge y Covi por todo lo que hicieron por mi cuando llegué a Liverpool. Muchas gracias tíos! También me quiero acordar de Bea, o "Esmeralda" para los amigos, y ese viaje por Escocia, y sin olvidarme de gente como Gloria, entre otros.

Dans ce moment, je voudrais me rappeler de Mathieu et Laetitia. Merci pour m'avoir accueilli chez vous, de m'avoir fait découvrir la Normandie et surtout merci beaucoup pour votre amitié. Mathieu, merci beaucoup pour m'avoir fait découvrir le monde de la microscopie et pour tes discussions de foot tous les lundi matin.

I would also like to thank very specially Helen and Paul for all their kindness every time and without no reason. Helen, thank you very much for all the help in the lab and outside the lab. You have done that Liverpool will always be part of my life.

Finally, form the Liverpool family, I would like to thank Matthew for all his help with the research and his patience to teach me everything he

knows (Science and no Science). Cheers mate for your friendship!! It's hard to have you far away…

Apres de la famille "Liverpoolienne", je voudrais me rappeler et remercier à toute la famille Caennaise. Merci beaucoup à Herve, Jean-François (ou Jennifer), Carlos, Eeva, Gaetan (Moumoute), Nicolas, Nadia, Maria, Chris, Xavier, Manu, Bruno, Radu, Mirca, Hélène et tous les autres doctorants, post-doctorants, techniciens et permanents (merci Christine pour avoir partagé le bureau avec moi) avec lesquels j'ai partagé cette année et demie.

Muchas gracias a todos aquellos que han formado parte de nuestras famosas "soires espagnoles": Tato (gracias por enseñarnos el concepto de "pueblo"), Anna (gracias por vivir esa Eurocopa conmigo como una forofa mas), Ulrike, Montse, Irene, Clément y Esther.

Merci beaucoup à Clara et Yohann pour leur barbecues au bord de la mer et pour m'avoir fait découvrir le pays du Bocage en vélo.

Merci beaucoup aussi à Antoine pour avoir partagé avec moi le bureau et pour avoir passé avec moi autant de bons moments en face d'une bière, d'un ballon de foot (ou basket) ou en regardant les lundi les buts du week-end d'avant sur « Rojadirecta ».

Muchísimas gracias a Fanfan y Natalia. Fanfan, merci beaucoup pour ton hospitalité, ton aide et ta introduction au monde du FC Basly. Natalia, muchas gracias por todo, por tus ayudas como interprete cuando llegue a Caen, por tu disponibilidad en todo momento, por tus cursos de magnetismo y, sobretodo, porque de esta tesis uno de las mejores cosas que me llevo es tu amistad.

Et pour finir avec la famille Caennaise, et non pas parce que c'est la moins importante sinon tout le contraire, je voudrais remercier très spécialement Mélanie tout son amour et sa patience qu'elle me donne chaque jour. Merci beaucoup pour partager avec moi tous ces moments de ma vie surtout parce qu'après ces trois années, tu es la meilleure chose qui me soit arrivé.

Y por ultimo me gustaría acordarme de mi gente de España. En primer lugar todos mis amigos que me han apoyado y animado a hacer esta tesis: Pili, Elena, Ana, Ana, Rafa, Toribio, Miriam, Eva (gracias por tu apoyo cuando mas lo he necesitado), Nora (gracias por ese fin de semana en Liverpool inolvidable), Nacho (gracias por esas visitas tanto a Liverpool como a Caen y por ayudarme a conocer un poco mejor "la Belgique"), Jorge (gracias por tus charlas por teléfono, por esas visitas a Liverpool y por disfrutar conmigo con la Eurocopa desde la distancia), Carlos (gracias por hacerme descubrir la Beamish, de hacer de Liverpool mucho mas cercana de casa y de tu apoyo y ánimos incondicionales) y Esther (gracias por seguir luchando por aquel Nobel, por estar siempre ahí y por hacer de Liverpool una parte común de nuestras vidas). Muchas gracias a todos, que a menudo la distancia se hace muy dura y se os echa mucho de menos.

Por ultimo quería agradecer el apoyo de toda mi familia: a mis "hermanos" Daniel y Guillermo (por hacerme sentir orgulloso de ellos), a mi abuela Marichu (por siempre creer en mi), a mi hermana Sara (por darme siempre todo su amor), a Paloma (por toda su pedagogía y paciencia) y muy especialmente a mi madre y a mi padre (por hacerme lo que soy). Muchas gracias a todos!!

Chapter 1:

Introduction

1.1. Solid Oxide Fuel Cells (SOFC's): history and limits.

During recent decades, the future of power generation has been an active concern around the world. The rapid development of populous third-world countries such as China, India and other South-East Asian countries have increased the international demand which it has mainly come from the fossil energy resources. Fossil fuel power generation is becoming unsustainable due to the limited sources of fossil fuels and the environmental problems associated such as global warming. Renewable energy sources and the development of new technologies such as fuel cell are crucial in order to find an alternative to these limited fossil fuels. Fuel cells are currently thought to be a good alternative for power production. They can use hydrogen as fuel which gives to the world an alternative and clean power source with many diverse applications.

The first reports in the literature on this subject date back more than a century. In 1839, Sir Williams Grove[1] reported a hydrogen fuel cell which

is considered the first fuel cell constructed from ceramic materials. Then, in the late 19th and early 20th centuries[2-4], the Nernst lamps were demonstrated which were the first devices to utilise an oxide ion conducting material. Later, in the 1930s, a large amount of research on solid electrolytes was carried out and a solid electrolyte fuel cell was presented by Baur et al[5]. However, it was not until the 1960s that generation of electricity from a "solid electrolyte fuel cell"[6] was demonstrated by what is now known as Siemens.

The Solid Oxide Fuel Cell (SOFC) is an electrochemical conversion device which permits the generation of electric energy from the oxidation of a fuel[7,8]. An SOFC cell consists of ceramic materials: cathode, electrolyte, anode and interconnect. Figure 1 shows a schematic of a solid oxide fuel cell showing the different elements that form these devices. The oxidant is admitted to one side of the cell and comes into contact with the cathode. Here the reduction of oxygen to O^{2-} ions takes place. These ions then diffuse through the electrolyte to the anode where they can electrochemically oxidize the fuel. If hydrogen is used as the fuel, water and two electrons are produced. These electrons then flow through an external circuit where they can generate the desired electrical energy and reduce oxygen at the cathode.

The cells, represented in Figure 1, are only a few millimetres thick. Each cell generates only a few volts and therefore, hundreds of these cells are connected together in order to form what is known as a "SOFC stack". Another important factor is the temperature these devices need to operate at. In order to obtain good performance they typically need to run between 600 °C and 1000 °C in order to become sufficiently electrically and ionically

conducting and electrochemically active in order to efficiently generate electricity.

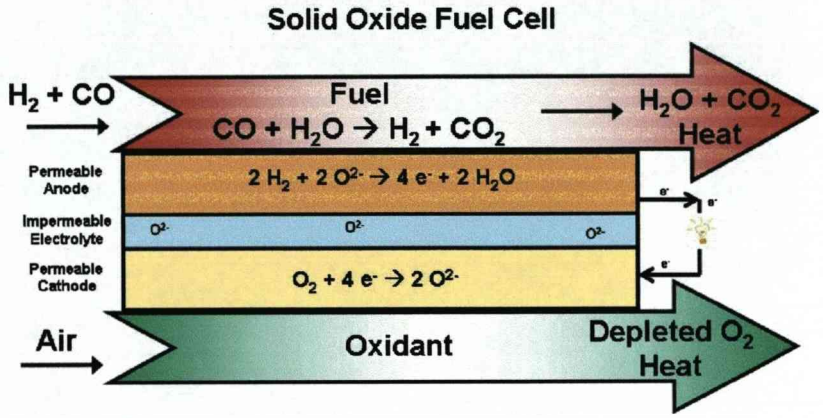

Figure 1. *Schematic of a solid oxide fuel cell (SOFC) showing the different parts and the path that the electrons follow in order to obtain the electric energy.*

1.1.1. Applications.

Many applications of SOFCs have been suggested[9]. Of these most are energy-related applications which have been widely reported. Amongst these many examples[10] of application of SOFC for stationary energy sources

or to generate electric power for transport. The demand for electricity around the world is calculated to be double in the next 20 years[11] due to the increase in the worldwide population and the economic development of new economies discussed previously. This technology could provide electric energy to many facilities such as homes, hospitals, schools, etc... Nowadays, there are many companies working on developing the solid oxide fuel cells, e.g. Siemens[6] and Ceramic Fuel Cells.

Another sector where Solid Oxide Fuel Cells could have an important role is transport. There are about 600 millions vehicles around the world and it is calculated that this number will increase by 30 % in the next 10 years[12] due to the same factors discussed previously. Furthermore, nowadays there is increasing concern about the environmental impact of the current emissions of this sector. SOFC technology could contribute to create less polluting cars by means of, for instance, auxiliary power units (APU). Car manufacturers such as Volvo & BMW are investing significant amounts in order to develop this technology.

1.1.2. Components.

The Solid Oxide Fuel Cell was previously defined as a chemical device made of four components: cathode, electrolyte, anode and interconnect. In the next sections, we will describe the function of each part,

their required properties and examples of materials reported as promising for SOFC components.

1.1.2.1. The cathode.

The cathode of the Solid Oxide Fuel Cells devices is where the oxygen reduction occurs. This reaction can be written as follow:

$$\frac{1}{2}O_2 + V_O^{\bullet\bullet} + 2e^- \Leftrightarrow O_O^x$$

where V states for a vacancy site, $\cdot$ for a single charged and X for null charged.

Promising cathode materials must be chemically stable under the cell operating temperature conditions and under the oxidising atmosphere environment present on the cathode side of the cell. It must also be a good electronic conductor and have fast oxygen reduction kinetics. In addition, it is also required to be compatible with the other cell components. The electrode itself must have a stable porosity in order to allow effective diffusion of oxygen.

The most commonly applied material as the cathode material is the perovskite-based material $La_{1-x}Sr_xMnO_3$[13]. The best electronic conductivity and compatibility with the other SOFC components have been found for values between x = 0.2 - 0.3, although is insufficient for operation at

temperatures below 800 °C[14]. In order to solve this problem mixed electronic conducting materials such as the perovskite $La_{0.6}Sr_{0.4}Co_{0.2}Fe_{0.8}O_{3-\delta}$[15,16] (LSCF) have been developed. It has a very good diffusion of the oxygen to the electrolyte; although reacts with the typical yttria stabilised zirconia (YSZ) electrolyte material to form some non-conductive phases. These materials also display very high oxide ion diffusivities: although reaction with the (YSZ) electrolyte material to form non-conductive phases is a barrier to their application[17]. Other examples of materials reported as good cathodes are $Ba_{0.5}Sr_{0.5}Co_{0.8}Fe_{0.2}O_{3-\delta}$[18], the perovskite $Sm_{0.5}Sr_{0.5}CoO_3$[19] or the Ruddlesden-Popper phases $La_{2-x}Sr_xNiO_{4-\delta}$[20].

1.1.2.2. The electrolyte.

The oxide ion is transported from the cathode to the anode through the electrolyte. The electrolyte materials must be good ionic conductors but have a low electronic conductivity in order to obtain low resistive losses. They must be stable under a large range of oxygen partial pressures: reducing atmospheres in the anode side ($pO_2 \approx 10^{-21}$ atm) and oxidizing atmospheres in the cathode side ($pO_2 \approx 0.2$-1 atm). As has been mentioned for the cathode, the electrolyte must be chemically compatible with the other components of the cell. They must also be dense materials in order to avoid all possible loss of gas.

Yttrium stabilized zirconia (YSZ)[21] is the most widely applied electrolyte material due to its pure ionic conduction and its chemical stability in both oxidised and reduced atmospheres[22]. However, its performance is not so good at a temperature range lower than 700 °C where its ionic conductivity decreases. Gadolinium doped ceria compound (GDC)[23] has also been suggested as an electrolyte materials due to its very good ionic conduction[24], although these compounds present electric conduction under reduced atmosphere due to the formation of Ce^{3+}[25].

Many other materials have been suggested as alternatives to YSZ[26,27] amongst the most promising are the Sc-stabilised-Zirconia, $Sc_xZr_{1-x}O_{2-x/2}$ with an ideal doping level of x = 0.08-0.11[28], the perovskite oxide $La_{0.8}Sr_{0.2}Ga_{0.8}Mg_{0.2}O_3$ (LSGM)[29] or systems based on the brownmillerite Ba_2InO_5[30]. All these materials have been reported to have conductivity at intermediate temperatures, good chemical stability and negligible electronic conduction over a large range of oxygen partial pressures.

1.1.2.3. The anode.

The anode of the Solid Oxide Fuels Cell is where the oxidation of the fuel takes places. As it is shown in Figure 1, the reactions that take places at the anode can be written as follow:

$$H_2 + O_O^X \Leftrightarrow H_2O + V_O^{\bullet\bullet} + 2e$$

where V states for a vacancy site, $\cdot$ for a single charged and X for null charged.

Anode materials must be stable in reduced atmospheres. They must also have a good electronic conductivity and good electrochemical kinetics in order to provide low polarization resistance at the operating temperatures. As with the electrolyte and cathode materials, the anode materials must be chemically compatible with them and stable at both the operating and fabrication temperature. In the same manner than the cathode, the anode must have a good porosity in order to allow the gas access through it.

Cermets are composite materials constituted of a ceramic part and a metallic part. The most widely described are Ni-YSZ[31,32] cermets which show good performance at high temperatures (≈1000 °C). However, these materials have several disadvantages: the formation of carbon deposits when hydrocarbon fuels are used and sulfur poisoning of the anode. In order to find a solution to this problem other Co or Ru-based cermets[33] have been suggested. Although they have good properties they are too expensive for practical applications. Several attempts to find cheaper materials for novel anode have been reported in the literature such as Ceria, particularly doped with Gd_2O_3 or Sm_2O_3[25,34] and some perovskite structures materials such as some doped-$LaCrO_3$ oxides[35,36], $Sr_2Mg_xMn_{1-x}O_{6-\delta}$ oxides[37], $La_{0.75}Sr_{0.25}Cr_{0.5}Mn_{0.5}O_3$[8,38] and $La_2Sr_4Ti_6O_{19-\delta}$[39].

1.1.2.4. The interconnect.

The interconnect is also a crucial part in the Solid Oxide Fuel Cells. It links the hundreds of SOFCs cells into stacks. It must be stable in both reduced and oxidised atmospheres, must have a good electronic conduction and a high thermal conduction coefficient in order to prevent temperature gradients in the cell.

The most common material used for this component of the Solid Oxide Fuel Cells is lanthanum chromite ($LaCrO_3$) doped[40] with some alkaline-earth elements in order to improve its electronic conductivity. Some other materials can be found in the literature reported as good interconnect material such as the spinel $Mn_{1.5}Co_{1.5}O_4$[41].

1.2. Description of structures.

1.2.1. Perovskite structure.

Many oxides used as cathode or interface materials are related to perovskite structure. Perovskites have the general formula ABO_3 and are ideally cubic in $Pm\bar{3}m$ space group[42]. The structure can be described as a cube in which the eight vertices are occupied by the B cation, at the centre by the A cation and at the centre of the edges by the oxygens. The A-cations

are surrounded by 12 oxide ions and the B-cations are in octahedral coordination (Figure 2). The A-site is most commonly occupied by alkaline, alkaline earth ions or rare earths ions and more rarely by post-transition elements (Tl, Bi). The B-site is occupied by a transition metal. The BO_6 octahedras are linked by the vertices, forming a BO_3 network which has cavities (the perovskite holes) occupied by the A-cations.

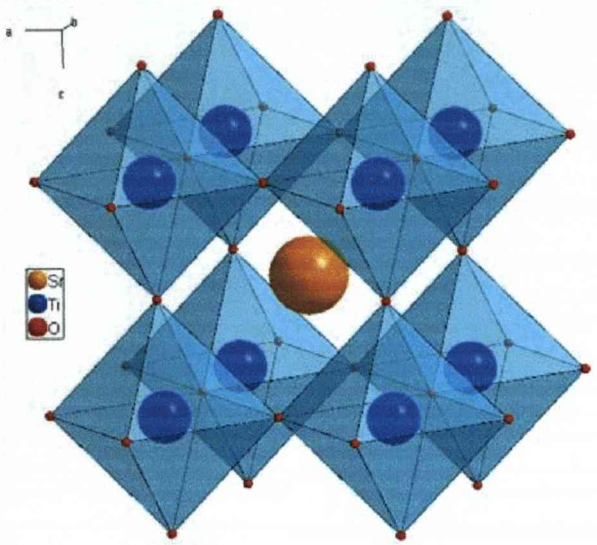

Figure 2. *Structure of the typical perovskite $SrTiO_3$. The Sr^{2+} ions are marked in orange, the Ti^{4+} ions in blue and the O^{2-} in red*[43].

The vast majority of perovskites are not actually cubic. This can be understood by considering the ionic radii of the ions. The tolerance factor given by Goldschmidt[44] defines the size limit of the cation in order to achieve a stable perovskite:

$$t = \frac{R_A + R_O}{\sqrt{2}(R_B + R_O)} = 1$$

where R_A, R_B and R_O are the ionic radii of A, B and O ions respectively. Geometry tells us that for t = 1, one would obtain and ideal cubic perovskite. However, it is still possible to obtain a stable perovskite for $0.75 < t < 1$.

The perovskite structure is so common due to its flexibility in allowing deformations of itself, in this manner a lot of substitutions in the cation-sites and non-stoichiometry by creation of oxygen vacancies in the cation and anion-sites often encountered. This is particularly common when the B-cations exhibit potentially different co ordinations (octahedral, tetragonal, pyramidal, etc).

When $t < 1$, the (M–O) bonds would be under compression and the (A–O) bonds under tension. The structure alleviates these stresses by a cooperative rotation of the $MX_{6/2}$ octahedra that lowers the space group symmetry from cubic ($Pm\bar{3}m$). Glazer[45,46] identified 15 tilt systems that are possible and their space groups. At the highest temperatures, perovskites are often cubic; transforming to a lower symmetry on cooling which introduces twins, which can make the determination of the local structure difficult.

Given their inherent compositional flexibility many compounds have interesting properties as potential anodes or cathodes for solid oxide fuel cells applications. In order to achieve these properties, the main strategy has been to dope some materials to create oxygen vacancies or interstitial oxygens. Some examples of this type of compounds are $CaTiO_3$[47], $SrTi_{1-}$

$_xFe_xO_3$[48,49], doped-$LaAlO_3$, doped-$LaScO_3$, doped-$LaInO_3$[50], $La_{0.3}Sr_{0.7}Fe(Ga)O_{3-\delta}$[51,52], $LaGa_{1-x}Ni_xO_{3-\delta}$[53], doped-$PrGaO_3$[54] and $La_{1-x}Me_xCoO_{3-\delta}$ (Me=Sr,Ca)[55] reported as good mixed conductors; $La_{1-x}Sr_xCo_{0.2}Fe_{0.8}O_3$[56,57], doped-$SrCeO_3$[58], doped-$BaCeO_3$[59] reported as good proton conductor; $La_{0.9}Sr_{0.1}Ga_{0.8}Mg_{0.2}O_{2.85}$[60] reported as a good electrolyte, doped-$LaCoO_3$[29,53,61-64] or $Sr_{0.8}Ce_{0.1}Fe_{0.7}Co_{0.3}O_{3-\delta}$[65] reported as good cathode materials and $(La_{0.75}Sr_{0.25})Cr_{0.5}Mn_{0.5}O_{3-\delta}$[66] reported as a good anode material.

1.2.2. Layered compounds: Ruddlesden-Popper (R-P) phases.

From the perovskite structure, it is possible to form complex intergrowths with the NaCl-type structure (Figure 3). When one or more layers of NaCl are present between perovskite blocks a large family of structures can be formulated as:

$$(A'O)_n^{NaCl}(AMO_{3-x})_m^p$$

where n and m represent the number of NaCl and perovskite layers respectively forming the intergrowth (M is a transition metal) .

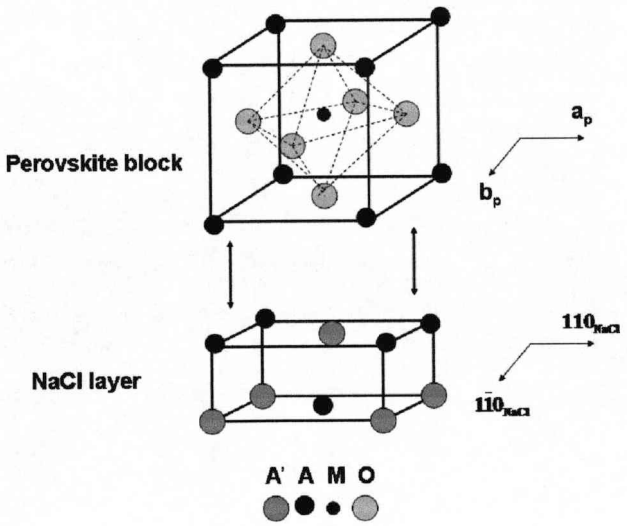

Figure 3. *Assembly of Perovskite and NaCl-type structures.*

Intergrowths of a single NaCl-type layer with a perovskite-type layer have idealised structures: where a = b ≈ 3.9 Å and $c \approx 2 \cdot (n \cdot a_p + \frac{1}{2} \cdot a_{NaCl})$. The first family of intergrowths phases formed by this structural motif were described by Ruddlesden and Popper in the family $Sr_{n+1}Ti_nO_{3n+1}$ (corresponding to $(SrO)(SrTiO_3)_n$)[67,68].

Experimentally it appears difficult to establish a long range order at large distance between the NaCl-type layer and examples with more three perovskite layers are rare. A schematic representation of the Ruddlesden-Popper type structures, corresponding to the terms n = 1, 2 and 3 in the system $Sr_{n+1}Ti_nO_{3n+1}$ is presented in the Figure 4.

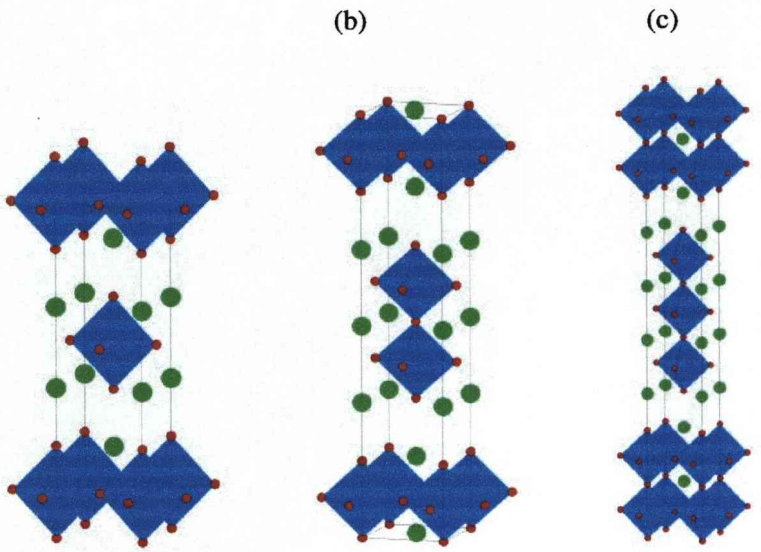

Figure 4. *Representation of the three first members of the Ruddlesden-Popper series of the* $Sr_{m+1}Ti_mO_{3m+1}$ *system: (a)* $n = 1$ Sr_2TiO_4*, (b)* $n = 2$ $Sr_3Ti_2O_7$ *and (c)* $Sr_4Ti_3O_{10}$[69].

Many of these compounds have been reported in the literature as good mixed conducting oxides. Some examples of these materials are $LaSr_3Fe_{3-x}Co_xO_{10}$ $(0 \leq x \geq 1.5)$[70], $Sr_3Fe_2O_{6+\delta}$[71], $Pr_2NiO_{4+\delta}$[72], $Na_2La_2Ti_3O_{10}$[73], $Sr_{n+1}(Ti_{1-x}In_x)_nO_{3n+1-nx/2}$ (m = 1,2 and ∞)[74], $Ca_4Mn_3O_{10}$[75-77], $Sr_{2-x}Nd_{1+x}Mn_2O_7$[78], $Sr_2LnMn_2O_7$ (Ln = Y, La, Nd, Eu, Ho)[79], $La_2NiO_{4+\delta}$[80-83].

1.2.3. Fluorite-type structure.

The Fluorite (AB_2) structure contains A ions in a cubic closest-packed arrangement with B ions occupying the tetrahedral holes (Figure 5).

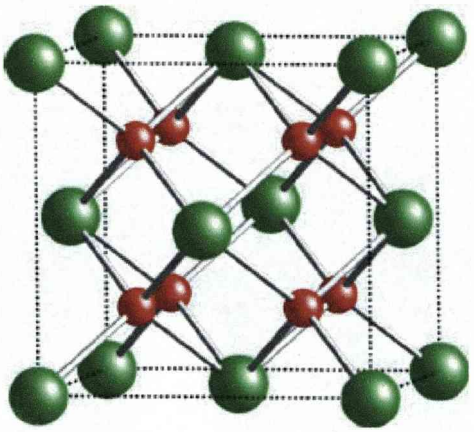

Figure 5. *Fluorite type structure with the A ions in green and the B ions in red*[84].

As with perovskite this structure type is also very flexible with respect to substitution and composition. Several compounds which exhibit this structure type have been reported in the literature as good mixed and ionic conductors and as potential anodes and cathodes for application for solid oxide fuel cells[85,86]. Some examples of these compounds are the MO_2 oxides (M = Hf^{4+}, Zr^{4+}, Ce^{4+}, Th^{4+}, U^{4+})[87], $Ce_{1-x}Gd_xO_{2-x/2}$[88], $Ce_{0.8}Nd_{0.2}O_{2-\delta}$[89]., $Ce_{0.8}RE_{0.2}O_{1.9}$ (RE = La, Nd, Sm, Gd, Dy, Y, Ho, Er and Yb)[90]. Many materials based on the high temperature form of Bi_2O_3, which also adopts the fluorite structure, such as $Bi_{0.75}Sr_{0.25}O_{1.375}$[91], Bi_3NbO_7[92] or $Bi_{5-x}Ln_xNbO_{10}$ (Ln = La, Gd and Y)[93] as good electrolyte for solid oxide fuel cells applications (Figure 6).

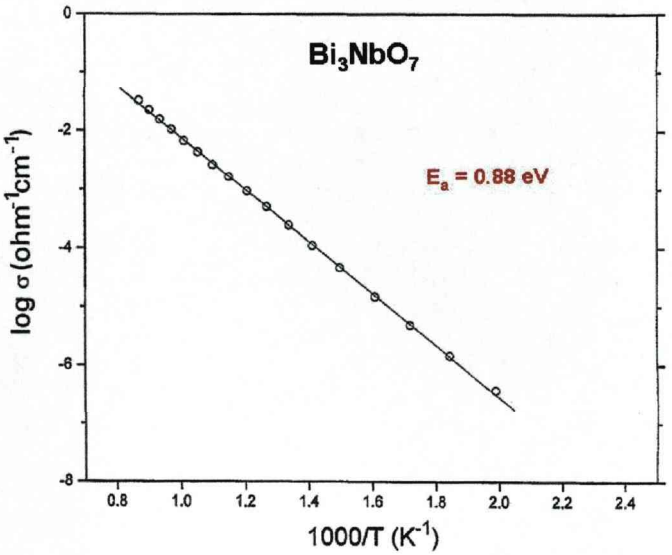

Figure 6. Logarithm of the conductivity versus the inverse of the temperature for Bi_3NbO_7.

1.3. Scope of this thesis

The objective of this thesis work is the exploration of materials with mixed conducting properties with potential for solid oxide fuel cells applications.

Chapter 1 gives an introduction to the solid oxide fuel cells: their components and main applications. This chapter also contains a description of the structures studied during this thesis. Chapter 2 presents all the experimental techniques used during this thesis.

Mo-based compounds have been investigated due to Mo's multivalent character. Studies of the structural and mixed conducting properties of Sr and Mo based perovskite oxides form the basis of Chapter 3, Chapter 4, Chapter 5 and Chapter 6. This work has been carried out with the help of Mathieu Allix (Liverpool) and Denis Pelloquin (Caen) in all the transmission electron microscopy; and Xiaojun Kuang (Liverpool) and Natalia Bellido Vera (Caen) for the physical property measurements.

One common strategy to obtain new materials with interesting properties is the doping of known materials. In the second part of this thesis, doping of Ruddlesden-Popper structures and fluorite-type structures was investigated. Chapter 7 and Chapter 8 present some doping strategies in the Ruddlesden-Popper phase $LaSrAlO_4$ & the fluorite-type material Bi_2O_3 respectively. Synthetic, chemical structure and physical characterisation details will be given for these new materials. This work has been carried out with the help of Mathieu Allix (Liverpool) and Denis Pelloquin (Caen) for the transmission electron microscopy; and Matthew Suchomel (Liverpool) and Xiaojun Kuang (Liverpool) with the physical property measurements.

1.4. References

(1) Grove, W. R. *Philos. Mag.* **1839**, *14*, 127-130.

(2) Cooper, H. C. *Science* **1898**, *8*, 710.

(3) Smith, H. M. *Science* **1898**, *8*, 689-690.

(4) Nernst, W.; Mutter, E. *Technik, Reisen und Nutzliche Naturbetrachtung in Haus und Familie.* **1899**.

(5) Baur E.; Preiss H.Z. *Z. Elektrochem* **1937**, *43*, 727.

(6) *SIEMENS, http://www.powergeneration.siemens.com/products-solutions-services/products-packages/fuel-cells/.*

(7) Minh, N. Q. *J. Am. Ceram. Soc.* **1993**, *76*, 563-588.

(8) Tao, S.; Irvine, J. T. S. *Nat. Mater.* **2003**, *2*, 320-323.

(9) Steele, B. C. H. *Mat. Sci. Eng. B-Solid* **1992**, *B13*, 79-87.

(10) Guire, E. J. D. *http://www.csa.com/discoveryguides/fuecel/overview.php.*

(11) Muneer, T.; Asif, M.; Kubie, J. *Energ. Convers. Manage.* **2003**, *44*, 35-52.

(12) *World Energy Council, http://www.worldenergy.org.*

(13) Van Herle, J.; McEvoy, A. J.; Ravindranathan Thampi, K. *Electrochim. Acta* **1996**, *41*, 1447-1454.

(14) Jiang, S. P. *J. Power Sources* **2003**, *124*, 390-402.

(15) Steele, B. C. H.; Bae, J. M. *Solid State Ionics* **1998**, *106*, 255-261.

(16) Esquirol, A.; Brandon, N. P.; Kilner, J. A.; Mogensen, M. *J. Electrochem. Soc.* **2004**, *151*, A1847-A1855.

(17) Kostogloudis, G. C.; Tsiniarakis, G.; Ftikos, C. *Solid State Ionics* **2000**, *135*, 529-535.

(18) Shao, Z.; Halle, S. M. *Nature* **2004**, *431*, 170-173.

(19) Xia, C.; Rauch, W.; Chen, F.; Liu, M. *Solid State Ionics* **2002**, *149*, 11-19.

(20) Skinner, S. J.; Kilner, J. A. *Solid State Ionics* **2000**, *135*, 709-712.

(21) Setoguchi, T.; Okamoto, K.; Eguchi, K.; Arai, H. *J. Electrochem. Soc.* **1992**, *139*, 2875-2880.

(22) Feighery, A. J.; Irvine, J. T. S. *Solid State Ionics* **1999**, *121*, 209-216.

(23) Inaba, H.; Tagawa, H. *Solid State Ionics* **1996**, *83*, 1-16.

(24) Perry Murray, E.; Barnett, S. A. *Solid State Ionics* **2001**, *143*, 265-273.

(25) Mogensen, M.; Sammes, N. M.; Tompsett, G. A. *Solid State Ionics* **2000**, *129*, 63-94.

(26) Gauckler, L. J.; Beckel, D.; Buergler, B. E.; Jud, E.; Muecke, U. P.; Prestat, M.; Rupp, J. L. M.; Richter, J. *Chimia* **2004**, *58*, 837-850.

(27) Tao, S.; Irvine, J. T. S. *Chemical Record* **2004**, *4*, 83-95.

(28) Politova, T. I.; Irvine, J. T. S. *Solid State Ionics* **2004**, *168*, 153-165.

(29) Ishihara, T.; Matsuda, H.; Takita, Y. *J. Am. Chem. Soc.* **1994**, *116*, 3801-3803.

(30) Goodenough, J. B.; Ruiz-Diaz, J. E.; Zhen, Y. S. *Solid State Ionics* **1990**, *44*, 21-31.

(31) Aruna, S. T.; Muthuraman, M.; Patil, K. C. *Solid State Ionics* **1998**, *111*, 45-51.

(32) Matsuzaki, Y.; Yasuda, I. *Solid State Ionics* **2000**, *132*, 261-269.

(33) Takeguchi, T.; Kikuchi, R.; Yano, T.; Eguchi, K.; Murata, K. *Catal. Today* **2003**, *84*, 217-222.

(34) Eguchi, K.; Setoguchi, T.; Inoue, T.; Arai, H. *Solid State Ionics* **1992**, *52*, 165-172.

(35) Sfeir, J. *J. Power Sources* **2003**, *118*, 276-285.

(36) Baker, R. T.; Metcalfe, I. S.; Middleton, P. H.; Steele, B. C. H. *Solid State Ionics* **1994**, *72*, 328-333.

(37) Huang, Y. H.; Dass, R. I.; King, Z. L.; Goodenough, J. B. *Science* **2006**, *312*, 254-257.

(38) Tao, S.; Irvine, J. T. S. *J. Electrochem. Soc.* **2004**, *151*, A252-A259.

(39) Canales-Va?zquez, J.; Tao, S. W.; Irvine, J. T. S. *Solid State Ionics* **2003**, *159*, 159-165.

(40) Fergus, J. W. *Solid State Ionics* **2004**, *171*, 1-15.

(41) Yang, Z.; Xia, G.; Stevenson, J. W. *Electrochem. Solid St.* **2005**, *8*, A168-A170.

(42) Mitchell, R. H. *Perovskites: Modern and Ancient* **2002**. Almaz Press, Thunder Bay.

(43) *http://www.princeton.edu/~cavalab/tutorials/public/structures/perovskites.html.*

(44) Goldschmidt, V. M. *Die Naturwissenschaften* **1926**, *14*, 477-485.

(45) Glazer, A. M. *Acta Crystallogr. B* **1972**, *28*, 3384-3392.

(46) Glazer, A. M. *Acta Crystallogr. A* **1975**, *31*, 756-762.

(47) Iwahara, H.; Esaka, T.; Mangahara, T. *J. Appl. Electrochem.* **1988**, *18*, 173-177.

(48) Steinsvik, S.; Bugge, R.; Gjønnes, J.; Taftø, J.; Norby, T. *J. Phys. Chem. Solids* **1997**, *58*, 969-976.

(49) Kharton, V. V.; Kovalevsky, A. V.; Viskup, A. P.; Jurado, J. R.; Figueiredo, F. M.; Naumovich, E. N.; Frade, J. R. *J. Solid State Chem.* **2001**, *156*, 437-444.

(50) Lybye, D.; Poulsen, F. W.; Mogensen, M. *Solid State Ionics* **2000**, *128*, 91-103.

(51) Kharton, V. V.; Shaulo, A. L.; Viskup, A. P.; Avdeev, M.; Yaremchenko, A. A.; Patrakeev, M. V.; Kurbakov, A. I.; Naumovich, E. N.; Marques, F. M. B. *Solid State Ionics* **2002**, *150*, 229-243.

(52) Tsipis, E. V.; Patrakeev, M. V.; Kharton, V. V.; Yaremchenko, A. A.; Mather, G. C.; Shaula, A. L.; Leonidov, I. A.; Kozhevnikov, V. L.; Frade, J. R. *Solid State Sci.* **2005**, *7*, 355-365.

(53) Yaremchenko, A. A.; Kharton, V. V.; Viskup, A. P.; Naumovich, E. N.; Lapchuk, N. M.; Tikhonovich, V. N. *J. Solid State Chem.* **1999**, *142*, 325-335.

(54) Ishihara, T.; Furutani, H.; Arikawa, H.; Honda, M.; Akbay, T.; Takita, Y. *J. Electrochem. Soc.* **1999**, *146*, 1643-1649.

(55) Zipprich, W.; Waschilewski, S.; Rocholl, F.; Wiemho?fer, H. D. *Solid State Ionics* **1997**, *101-103*, 1015-1023.

(56) Mineshige, A.; Izutsu, J.; Nakamura, M.; Nigaki, K.; Abe, J.; Kobune, M.; Fujii, S.; Yazawa, T. *Solid State Ionics* **2005**, *176*, 1145-1149.

(57) Chou, Y. S.; Stevenson, J. W.; Armstrong, T. R.; Pederson, L. R. *J. Am. Ceam. Soc.* **2000**, *83*, 1457-1464.

(58) Mather, G. C.; Islam, M. S. *Chem. Mater.* **2005**, *17*, 1736-1744.

(59) Iwahara, H.; Uchida, H.; Ono, K.; Ogaki, K. *J. Electrochem. Soc.* **1988**, *135*, 529-533.

(60) Slater, P. R.; Irvine, J. T. S.; Ishihara, T.; Takita, Y. *Solid State Ionics* **1998**, *107*, 319-323.

(61) Huang, K.; Lee, H. Y.; Goodenough, J. B. *J. Electrochem. Soc.* **1998**, *145*, 3220-3227.

(62) Huang, K.; Tichy, R. S.; Goodenough, J. B. *J. Am. Ceram. Soc.* **1998**, *81*, 2565-2575.

(63) Ishihara, T.; Honda, M.; Shibayama, T.; Minami, H.; Nishiguchi, H.; Takita, Y. *J. Electrochem. Soc.* **1998**, *145*, 3177-3183.

(64) Ishihara, T.; Yamada, T.; Arikawa, H.; Nishiguchi, H.; Takita, Y. *Solid State Ionics* **2000**, *135*, 631-636.

(65) Colomer, M. T.; Steele, B. C. H.; Kilner, J. A. *Solid State Ionics* **2002**, *147*, 41-48.

(66) Wan, J.; Zhu, J. H.; Goodenough, J. B. *Solid State Ionics* **2006**, *177*, 1211-1217.

(67) Ruddlesden, S. N.; Popper, P. *Acta Crystallographica* **1958**, *11*, 54-55.

(68) Ruddlesden, S. N.; Popper, P. *Acta Crystallogr.* **1957**, *10*, 538-540.

(69) *http://www.soton.ac.uk/~solids/popper.htm*.

(70) Armstrong, T.; Prado, F.; Manthiram, A. *Solid State Ionics* **2001**, *140*, 89-96.

(71) Prado, F.; Mogni, L.; Cuello, G. J.; Caneiro, A. *Solid State Ionics* **2007**, *178*, 77-82.

(72) Kovalevsky, A. V.; Kharton, V. V.; Yaremchenko, A. A.; Pivak, Y. V.; Tsipis, E. V.; Yakovlev, S. O.; Markov, A. A.; Naumovich, E. N.; Frade, J. R. *J. Electroceram.* **2007**, *18*, 205-218.

(73) Toda, K.; Kameo, Y.; Fujimoto, M.; Sato, M. *Nippon Seram. Kyo. Gak.* **1994**, *102*, 737-741.

(74) Shimura, T.; Suzuki, K.; Iwahara, H. *Solid State Ionics* **1998**, *113-115*, 355-361.

(75) Lago, J.; Battle, P. D.; Rosseinsky, M. J.; Coldea, A. I.; Singleton, J. *J.Phy-Condens. Mat.* **2003**, *15*, 6817-6833.

(76) Battle, P. D.; Green, M. A.; Laskey, N. S.; Millburn, J. E.; Murphy, L.; Rosseinsky, M. J.; Sullivan, S. P.; Vente, J. F. *Chem. Mater.* **1997**, *9*, 552-559.

(77) Battle, P. D.; Rosseinsky, M. J. *Curr. Opin. Solid St. M.* **1999**, *4*, 163-170.

(78) Battle, P. D.; Green, M. A.; Laskey, N. S.; Millburn, J. E.; Radaelli, P. G.; Rosseinsky, M. J.; Sullivan, S. P.; Vente, J. F. *Phy. Rev.B* **1996**, *54*, 15967-15977.

(79) Sloan, J.; Battle, P. D.; Green, M. A.; Rosseinsky, M. J.; Vente, J. F. *J. Solid State Chem.***1998**, *138*, 135-140.

(80) Rodriguez-Carvajal, J.; Fernandez-Diaz, M. T.; Martinez, J. L. *J. Phys-Condens. Mat.***1991**, *3*, 3215-3234.

(81) Tranquada, J. M.; Buttrey, D. J.; Sachan, V.; Lorenzo, J. E. *Phys. Rev. Lett.* **1994**, *73*, 1003-1006.

(82) Demourgues, A.; Dordor, P.; Doumerc, J. P.; Grenier, J. C.; Marquestaut, E.; Pouchard, M.; Villesuzanne, A.; Wattiaux, A. *J. Solid State Chem.* **1996**, *124*, 199-204.

(83) Kharton, V. V.; Viskup, A. P.; Naumovkh, E. N.; Marques, F. M. B. *J. Mater. Chem.***1999**, *9*, 2623-2629.

(84) *http://www-ssrl.slac.stanford.edu/research/highlights_archive/rockyflats.html.*

(85) Tuller, H. L. *Solid State Ionics* **1992**, *52*, 135-146.

(86) Lacorre, P.; Goutenoire, F.; Bohnke, O.; Retoux, R.; Lallgant, Y. *Nature* **2000**, *404*, 856-858.

(87) Kim, D.-J. *J. Am. Ceram. Soc.* **1989**, *72*, 1415-1421.

(88) Kudo, T.; Obayashi, H. *J. Electrochem. Soc.* **1976**, *123*, 415-419.

(89) Lin, X. M.; Li, L. P.; Li, G. S.; Su, W. H. *Mater. Chem. Phys.* **2001**, *69*, 236-240.

(90) Li, J. G.; Ikegami, T.; Mori, T.; Wada, T. *Chem. Mater.* **2001**, *13*, 2913-2920.

(91) Mercurio, D.; Champarnaud-Mesjard, J. C.; Frit, B.; Conflant, P.; Boivin, J. C.; Vogt, T. *J. Solid State Chem.* **1994**, *112*, 1-8.

(92) Castro, A.; Aguado, E.; Rojo, J. M.; Herrero, P.; Enjalbert, R.; Galy, J. *Mater. Res. Bull.* **1998**, *33*, 31-41.

(93) Wang, X. P.; Corbel, G.; Fang, Q. F.; Lacorre, P. *J. Mater. Chem.* **2006**, *16*, 1561-1566.

Chapter 2: Experimental

2.1. Synthetic methods.

The ceramic method has been used to synthesise the materials presented in this thesis[1-3]. Stoichiometric quantities of the starting materials, oxides and carbonates, were weighted and then mixed and ground using an agate mortar (Table 1). In order to improve the homogeneity of the mixture materials were mixed in acetone during grinding. For larger samples to improve the homogeneity of samples rolling mill was used. The samples were introduced into polythene bottles with yttria stabilised zirconia grinding media. Acetone was added and the bottle rotated. A cascading effect grinds the material to produce a fine powder. Generally several hours are sufficient for this effect. Once the acetone had been evaporated the mixture was pelletised into bars or pellets, with a mechanical uniaxial press to a pressure of 1 t/cm^2 in order to achieve compact materials. The dimensions of the bars were typically 2 x 2 x 10 mm^2 and for pellets diameters were 13 mm, 10 mm or 8 mm, depending on sample size and application.

The samples were then placed in alumina crucibles and calcined at high temperature. In some the cases, platinum foil to isolate the sample from the crucible and avoid reaction with the crucible at high temperature was

Table 1. *Synthetic conditions summary for all the materials synthesised in the thesis.*

Materials	Reagents	Synthetic method	Atmosphere	Max. Temp. (°C)	Max. Time (h)	Number Grinding	Quantity (g)
Sr_2MgMoO_6	$SrCO_3$, MgO, MoO_3	Solid State Reaction	Air	1350	103	3	1
$Sr_2MgMoO_{6-\delta}$	Sr_2MgMoO_6	Solid State Reaction	5 % H_2/N_2	1200	12	0	1
$Sr_3Mg_{0.5}Mo_{1.5}O_{7-\delta}$	SrO, MgO, MoO_3, Mo	Solid State Reaction	Vacuum	1200	60	0	0.5
$Sr_{11}Mo_4O_{23}$	$SrCO_3$, MoO_3	Solid State Reaction	Air	1300	60	2	1
$La_{1+x}Sr_{1-x}Ni_xAl_{1-x}O_4$	La_2O_3, $SrCO_3$, Al_2O_3, NiO	Solid State Reaction	Air	1300	80	2	1
$Bi_8Cr_7O_{22.5}$	Bi_2O_3, Cr_2O_3	Solid State Reaction	Vacuum	800	24	0	0.5
$Bi_{17}Cr_8Sr_7O_{44.5}$	Bi_2O_3, Cr_2O_3, SrO	Solid State Reaction	Vacuum	800	24	0	0.5

used. Samples were calcined under various atmospheres depending on the desired products: air, 5 % H_2/N_2, O_2.

Manipulations of air sensitive samples and reagents were carried out using Mbraun labmaster 130 dual user glove box. The system offers a working area where experiments can be carried out in a pressure controlled inert gas atmosphere. The operating gas employed was helium.

Residual water and oxygen did not exceed ~1 ppm due to a gas-purifying unit comprising of columns of molecular sieves and a copper catalyst. These were regenerated by heating under a flow of 10% hydrogen in nitrogen periodically. As a qualitative guide to the atmosphere quality, a 25 W light bulb with a hole in the outer casing was used to gauge oxygen levels within the working area. Bulb lifetimes greater than 48 hours were taken to indicate an atmosphere of sufficient quality.

In order to control the oxygen stoichiometry some materials were synthesised in sealed silica tubes under vacuum. The samples were placed in alumina crucibles in order to avoid the reaction with the silica tubes. In some of the cases it was found that the alumina crucibles reacted with the samples and therefore platinum tubes were used in order to protect the sample. The samples were then calcined at high temperatures, reactions using sealed silica tubes were heated and cooled at 1-2 ^{o}C/min to avoid potential failure of the tubes.

Repeated cycles of grinding and calcination were carried out to achieve complete reaction.

Ceramics used to perform the physical measurements were uniaxilly pressed into pellets and calcined at successively increased temperature from

250 °C to 1000 °C until a density of 85-90 % was obtained. In some of the cases, these treatments were not sufficient and pellets were formed an isostatic press. The densities of the pellets were obtained from the weight and measured dimension of the pellets.

2.2. Diffraction techniques.

2.2.1. X-Ray Diffraction.

X-rays are electromagnetic waves with much shorter wavelength than visible light. The principles of Powder X-Ray Diffraction (PXRD) are very well described in the literature[4-7], some of the key factor will be briefly described below.

Diffraction results from the periodic nature of atoms or molecules within a crystal structure. This means that a crystal can act as a three-dimensional diffraction grating to radiation of a wavelength comparable to the periodic repeat. For constructive interference to occur, Bragg's law must be satisfied (Equation 1).

$$2d_{hkl} \sin\theta = n\lambda \quad (1)$$

***Equation 1**. Bragg's Law where d_{hkl} is the interplanar spacing of the crystal, θ is the X-ray incidence angle (Bragg angle) and λ is the wavelength of the characteristic x-rays.*

The Bragg approach to diffraction is to regard crystals as series of semitransparent planes. These planes reflect some X-rays with the angle of reflection equal to the angle of incidence.

X-Ray diffractometers produce an incident beam of photons with various wavelengths via excitation on a metal target with electron. The choice of metal target within the X-Ray tube determines the resultant wavelength based on the characteristic X-ray emission wavelenghts. The most commonly used targets are cobalt, copper, chromium and molybdenum, offering incident beams with a wavelength varying from ~2.29 to 0.7 Å respectively.

Figure 1 illustrates a general laboratory X-Ray diffractometer. This diffractometer has a source of monochromatic radiation and an X-Ray detector. This detector is placed on the circumference of a graduated circle centred on the powder sample. In order to collimate the X-Ray beam and reduce background noise, divergent slits are placed between the source and the sample and receiving slits between the sample and the detector. The detector and the sample are mechanically coupled by means of a goniometer. In order to obtain monochromatic radiation a crystal monochromator can be used to select a particular emission line, in older

diffractometers an absorber was used instead with an edge chosen to remove other characteristic emission lines, these can be placed before or after the sample. The signals from the detector are converted into a continuous current and read by an output device.

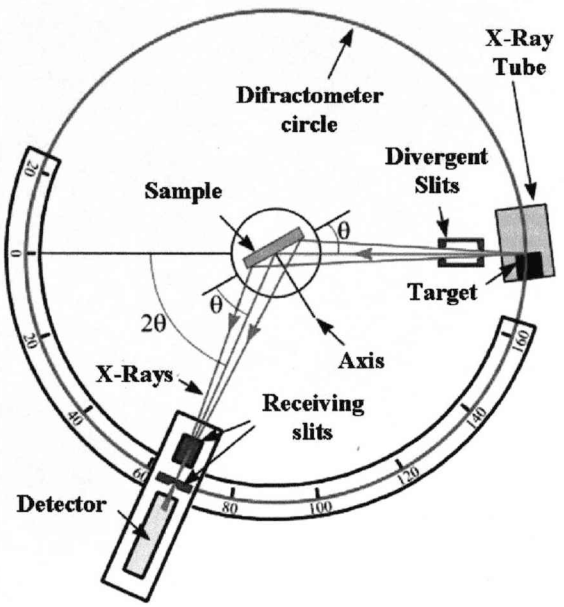

Figure 1. *General scheme of an X-Ray diffractometer*[8].

Three laboratory diffractometers have been used during this work: a STOE STADI P Bragg-Brentano geometry laboratory X-ray diffractometer with Cu $K_{\alpha 1}$ (λ = 1.5406Å) radiation, a Panalytical X-pert pro diffractometer with Co $K_{\alpha 1}$ (λ = 1.7890Å) radiation source and a Philips X'Pert pro diffractometer with Cu $K_{\alpha 1}$ and $K_{\alpha 2}$ (λ_1 = 1.5406 Å and λ_2 = 1.5443 Å) radiation.

STOE STADI P - Bragg-Brentano geometry diffractometer combined a focused Cu $K_{\alpha 1}$ divergent incident beam from a curved quartz monochromator of the Johansson-type with a position sensitive detector (PSD) or scintillation counter. The 2-circle diffractometer had an extremely high angular accuracy of better than 0.001°. The system provides high angular resolution data for powders.

The diffractometer had a computer-controlled lead covered shutter, which allowed the incident beam to travel down the beam tube and a stainless steel collimator. The sample was placed on a zero background plate, and placed on the sample stage on the goniometer. The sample was then rotated. The diffracted X-ray photons were detected by a linear PSD with a counting gas comprising of a 90% Ar and 10% methane.

The PSD collects an angular range of $2\theta = 6.5 - 7°$ and it was used to collect data in steps width of 0.1° – 1°. Signals were recorded via a delay line which comprises of a series of electrical sensors created on the counting wire. Due to the ionisation of the counting gas by incoming X-ray photons, electrical currents are induced in the delay line and move towards the ends of the conducting delay line, where the pulses arrive at different times. This time delay is measured for each incoming photon and allows the determination to its exact location on the delay line.

The Panalytical X'pert Pro Alpha^{-1} system offers the user the ability to switch the position of the ceramic Co X-ray tube with respect to the four-crystal germanium monochromator of the Johansson type. This allows several incident beam configurations, ideal for the rapid characterisation of

a range of materials. However, the data collected were measured using a monochromatic incident beam in Bragg Brentano geometry.

The diffractometer comprises of an X'Pert PRO standard resolution goniometer operating in the vertical mode and θ - 2θ configuration. With the X-ray tube in the $\alpha 1$ position, the monochromatic incident beam was collimated on the sample using a variety of fixed and programmable anti-scatter and divergence slits. The diffracted X-ray photons were collected using a real time multiple strip detector (RTMS). The diffracted beam optics could also be configured to optimise intensity using receiving slits and fixed or programmable anti-scatter slits.

The RTMS X'celerator detector operates as if there are arrays of over a hundred detectors at work simultaneously. RTMS technology offers direct X-ray detection over a wide 2θ range and the ability to efficiently process high-count rates. This reduces measurement times for normal powder diffraction.

Samples were mounted on an off axis cut silicon wafer zero background holder and mounted on a sample spinner. Capillary and a fixed flat plate bracket could also be used allowing a wide variety of sample types to be measured.

The Philips X-pert Pro diffractometer is a theta to theta goniometer system operating in Bragg-Brentano geometry. This allowed the use of a furnace with controlled atmosphere. The incident beam contained both Cu K_α components ($IK_{\alpha 2}/IK_{\alpha 1}$ = 0.483). Two detectors were employed: a high count rate (500k c/s) proportional detector in conjunction with a curved

graphite monochromator for precision measurements and a position sensitive detector for high speed measurements.

The multichannel detector had an angular aperture 2.121° and allowed data to be acquired up to 100 times faster than with the proportional detector. The primary optics could include Soller slits of 0.04 or 0.02 radians, an attenuator, a set of divergence slits of between 1/16° and 2° and a set of anti-scatter slits of between 1/16° and 2°. The secondary optic could include Soller slits of 0.04 or 0.02 rd, a K_β filter, and anti-scatter slits of between 1/16° and 2° when the proportional detector is used and between 0.1 and 5 mm when the X'Celerator detector is used.

The advantage of the Philips diffractometer is the possibility of making quick scans of fifteen minutes approximately. All these scans are good enough to test the quality of the sample, to refine the cell parameters and to see the presence of possible impurities with the utilisation of the X'Pert HighScore software from PANanalytical.

Standard identification scans were performed in the angular range between 4° and 90° with a step of 0.017° and took fifteen minutes. These scans were used for phase ID and indexing. In order to perform structural refinements long scans were collected in the angular range between 5° and 140° with a step of 0.017° and duration of 4-5 h.

2.2.2. Synchrotron X-Ray Diffraction.

X-rays produced by a synchrotron source can be used for high-resolution powder diffraction experiments. In a synchrotron electrons are

accelerated close to the speed of light. At the SRS the synchrotron comprises of a 2 GeV electron storage ring, operating at circulating currents up to 250 mA and a lifetime of up to 24 hours. In the storage ring the electrons are maintained in an approximately circular path by a series of magnets. When the electrons are deflected by one of these magnets, they emit intense radiation tangential to the ring over a wide range of energies including X-ray wavelengths. The synchrotron light spectrum emitted from bending magnets and insertion devices such as high field superconducting wigglers produces white beams in varying spectral ranges ideal for a variety of experimental applications.

Synchrotron X-Ray data[9] were collected for some of the samples at the Station 9.1 of the SRS[10], Daresbury Laboratories (UK). The Station has two principle modes of operation as a conventional 2-circle powder diffractometer or using an image-plate for time resolved measurements. Only the former was used during the work described in the thesis. The monochromator is a Si (111) channel-cut crystal maintained at a temperature of 30°C providing a wavelength range from 0.4 Å to 1.7 Å. Due to the absorbing nature of the samples wavelengths of 1.0 Å or shorter were typically used.

2.2.3. Neutron diffraction.

Neutron diffraction is a powerful technique used to determine the structure of the materials. Since, neutrons are uncharged particles, they have considerable penetrating power. The atomic scattering factors for X-Rays

increase proportionally to the number of electrons while this is not the case for neutrons. For neutrons, although there is a small increase of nuclear scattering factor with the mass number of the element, this is largely obscured by resonance effects which vary in a random manner for the different nuclei. The difference between the relative size of cross-sections (scattering factor) for X-Ray and neutron is illustrated in Figure 2.

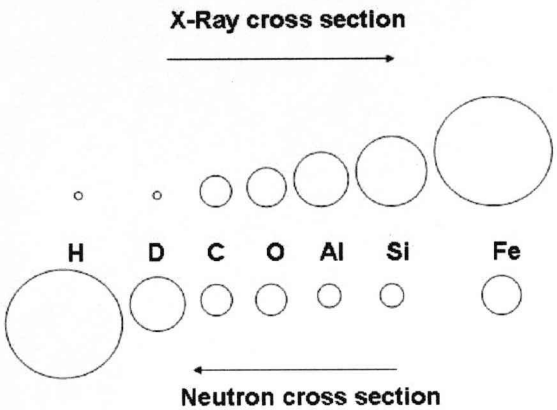

Figure 2. *Difference between the relative sizes of the cross-sections between X-Ray and neutron for some elements.*

As a consequence, neutron diffraction is more sensitive to the lighter elements like oxygen or hydrogen than X-Ray diffraction. In this respect, these two techniques are complementary. Another main difference between X-ray and neutron is related to the size of the electron cloud/nucleus. While the electron cloud has dimensions of about 1 Å, which is comparable with the X-ray wavelength, the radius of a nucleus is about 4 orders of magnitude smaller. Thus the nucleus may be considered a point scatterer giving rise to

no decrease with scattering angle of the neutron scattering factor. Additionally the neutron carries a spin allowing it interact with spins in the material and give information on the magnetic properties of materials.

Neutron diffraction data have been collected on two neutron diffractometers at ISIS[11] at Rutherford Appleton Laboratory (UK): HRPD (High Resolution Powder Diffraction)[12] and POLARIS[13].

HRPD, is almost 100m from target station one at ISIS, this long flight path provides good energy resolution target and in turn a $\Delta d/d$ resolution of $\sim 4 \times 10^{-4}$ which is effectively constant over the wide *d*-spacing range available. The main advantage of HRPD is its ability to resolve peaks resulting from small crystallographic distortions and due to its constant resolution as a function of d allowing peaks be resolved from complex materials at shorter *d*-spacing, where short wavelength neutrons from the ISIS target allow the collection of data at *d*-spacing below 0.6 Å.

POLARIS is the medium resolution, high intensity powder diffractometer, and is the ideal complement to HRPD. POLARIS is optimised for the rapid characterisation of structures, when small amounts of materials are available (≤ 1 mm^3), or when the collection multiple data sets is required (with data collection times down to ~5 minutes), where the ability of time-of-flight powder diffraction to collect an entire diffraction pattern at a single, fixed scattering angle is very useful.

2.3. Transmission Electron Microscopy (TEM) techniques.

During this work microstructural studies by Transmission Electron Microscopy (TEM) techniques have carried out in order to complement the X-Ray and Neutron diffraction studies. From single phases, a structural model can be obtained by means of direct methods and the refinement of X-ray and Neutron diffraction data. Nevertheless, for nearly pure samples or materials including complex microstructural effects (for instance extended defects) an initial model is needed in order to start this structural analysis. Electron microscopy combining electron diffraction (ED), image contrasts (HREM) and local chemical analysis (EDS) modes is a very useful technique to obtain initial compositions and structural information, the final structural analysis is a result of combining both microscopy and diffraction techniques[14].

Four electron microscopes have been used during this work: JEOL 200CX, JEOL 2010, JEOL 2000FX and JEOL 2010 FEG. The electron beam is produced from a LaB_6 crystal (heat gun) in the three first cases and for a metal gun under field (cold gun) in the case of the JEOL 2010 FEG (field emission gun) microscope, all heated under vacuum and accelerated under a potential of 200 kV to produce an electron beam with a wavelength of about 0.027 Å.

The electrons interact with the sample in several ways (Figure 3). In transmission electron microscopy, mainly the elastically scattered electrons

are used, either for diffraction mode or for image mode. Electrons absorbed by the sample are exploited using energy dispersive spectroscopy (EDS) to analyses the X-rays emitted for the sample. These X-Rays are produced due to the excitation produced by the beam in the sample.

Thus the microstructural and local chemical studies of the materials can be probed using the three functions of the TEM: electron diffraction (ED), high resolution images (HREM) and energy dispersive spectroscopy (EDS) analysis. Intergrowth mechanism, ordered and disordered structural defects and the building of structural models in the cases of large structures have been widely explored using this technique.

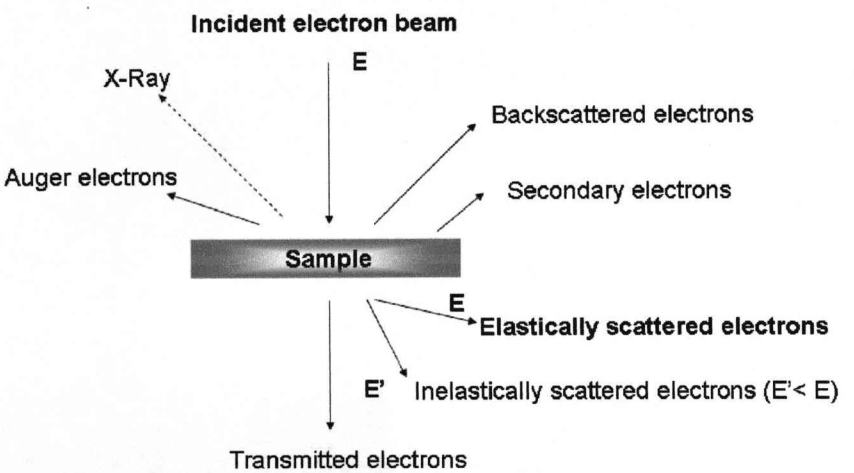

Figure 3. *Different radiation electron-matter interaction. In the case of the inelastically scattered electrons, a part of the energy is transferred to the sample.*

Another advantage of the TEM is that it is possible to examine individual crystallites in a polycrystalline sample and to detect the presence of secondary phases by analysing the sample on the scale of individual

crystallites. Diffraction studies are also powerful in revealing the presence of other diffraction phenomenon such as diffuse scattering, satellite peaks of low intensity and the presence of domain structures. This technique is a particularly powerful tool in order to determine the structure of the layered compounds studied in this thesis. It is important to notice that, like in all the microscopic techniques, in order to correlate observations to macroscopic properties a statistically valid number of crystals need to be studied to be representative of the bulk material.

2.3.1. Experimental Conditions.

The samples are ground under n-butanol. A drop of the suspension containing microcrystals was deposed onto a copper or nickel grid previously coated with a porous carbon film. This grid was then introduced into a sample-holder.

The majority of the electron diffraction studies were performed on a JEOL 200CX equipped with a eucentric plate (inclination ± 60°) and a tilt-rotation sample-holder. The high resolution images have been recorded from a JEOL 2011 FEG (resolution of 2.3 Å) microscope equipped with a eucentric plate (inclination ± 45°) and a tilt-rotation sample holder. Both microscopes operate at 200 kV.

2.3.2. Diffraction mode.

The diffracted electrons are focused at the focal plane of the objective lens (Figure 4). This image of the focal plane magnified by some intermediate lens leads to the electron diffraction pattern.

The formation of the Ewald Sphere in the reciprocal space is used in order to describe electron diffraction. If we consider a sphere with $r = 1/\lambda$, the Bragg condition will be satisfied for each reciprocal lattice point of the sphere. As the wavelength of the electrons is smaller (typically $\lambda = 0.025$ Å at 200 KV), the Ewald Sphere's radius is large. Therefore, the electron diffraction patterns are to a first approximation undistorted projections of the reciprocal planes (Figure 5). Studying several of these planes together allows the study of reciprocal space and therefore it allows to define of the cell parameters, the reflection conditions and in consequence the space groups.

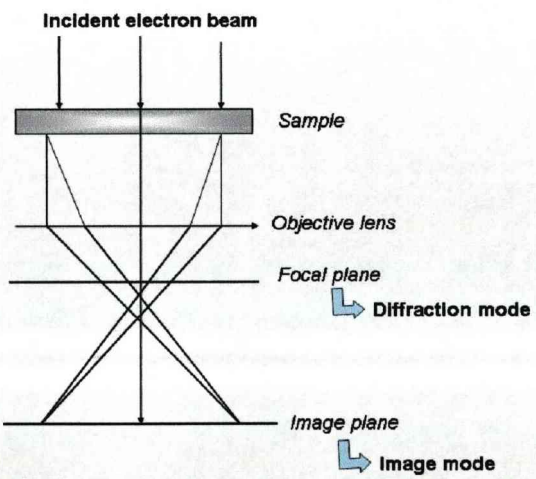

Figure 4. *Path of the diffracted electrons into a transmission electron microscope.*

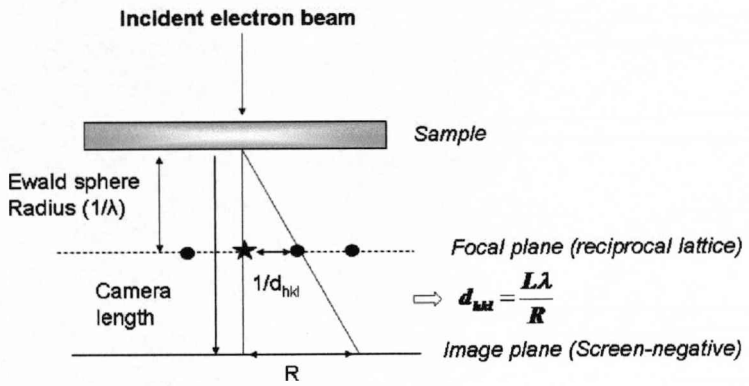

Figure 5. *Scheme showing the relation between the interplanar distances and the distance (R) measured in the film.*

2.3.3. High Resolution Mode.

High Resolution Electron Microscopy (HREM) is a technique which allows to obtain image contrasts at atomic resolution. These images are obtained by multiple interferences in the image plane between the incident beam and a set of diffracted beams. These beams are selected by an objective aperture placed at the level of the focal plane of the objective lens (Figure 4). This aperture allows the control of the nature and the number of beams used to form the image. As the contrast is complex, it is generally by studying a through focus series that it is possible to study the contrasts of phases and to connect them to the crystal structure.

The contrast analysis of experimental images was done with respect to the simulated images. The lattice images are calculated from a theoretical or refined model taking in account the experimental conditions (microscope parameters, defocus values and microcrystal thickness). Simulation presented in this work were performed using Mac Tempas[15].

2.3.4. Energy Dispersive Spectroscopy (EDS) analysis.

As highlighted previously, electrons interact in several ways with matter (Figure 3). In particular, many excited atoms are created which emit X-rays characteristic of the chemical element. The analysis of different energy peaks allows the quantification of the chemical elements detected in the studied area (due to the soft X-rays emitted from the light elements this is only reliable for atomic numbers above 11) by determination of the relative intensities of the lines of each element.

The main application of this technique is to define within a few percent the relative proportions of the elements present in the structure, and it also allow detection of secondary phases presents in the materials (sometimes unknown and/or unidentifiable by X-ray diffraction data). This technique is generally applied to a number of crystals (> crystals) in order to be statiscally valid.

2.4. Structural refinement: Rietveld Method.

Structural information was obtained from X-Ray and Neutron diffraction data by the line profiles method established by Rietveld[16,17]. In this method the crystallographic model is refined against the whole pattern rather than the individual Bragg peaks intensities. Fullprof[18] and GSAS[19] have been utilised for the data analysis. These calculations need a starting structural model obtained previously by direct methods, simulated annealing methods or TEM observations.

In the refinement process, non-structural parameters need to be considered:

- The background pattern,
- The shift between the origin and the scale factor,
- The cell parameters,
- The peak profiles which describes the intensity distribution around the Bragg position, 2θ, for a particular peak. This is done using various mathematical functions and refinable parameters to describe the peak. For instance, in the case of the Pseudo-Voigt function[20], the Gaussian components U, V, W are parameters which give an angular dependence to the full width half maximum of: $H = U\tan^2\theta + V\tan\theta + W$.
- Asymmetry parameters introduced to describe various experimental corrections to the peak shape at low angles.

In addition to these, structural parameters are also refined:

- The atom positions,

- The displacement atoms factors,
- The occupancy level of the crystallography sites,

In general the examination of the difference is the most reliable measure of the quality of a fit, however several reliable factors are extracted from the fit:

The profile factors $R_p = \frac{\sum |y_i - y_{ci}|}{\sum y_i}$ and the weighted profile

$R_{wp} = \left(\frac{\sum w_i (y_i - y_{ci})^2}{\sum w_i y_i^2} \right)^{1/2}$; where y_i is the intensity observed at $2\theta_i$; y_{ci} the calculated intensity at $2\theta_{ci}$ and w_i the weight attributed to each individual intensity y_i.

- The Bragg factor $R_{Bragg} = \frac{\sum_K |I_k - I_k^{calc}|}{\sum_K |I_K|}$; where I_k and I_K^{calc} are the observed integrated intensity and K^{th} reflection intensity integrated respectively.

The agreement between the weighted profile factor and the experimental profile R_{exp} is given for the χ^2 value which will be close to one in the best of the cases, this is the quantity minimised during the refinement.

$\chi^2 = \left[\frac{R_{wp}}{R_{exp}} \right]^2$ with $R_{exp} = \left[\frac{N - P + C}{\sum_i w_i Y_i^2} \right]^{1/2}$; where N is the number of points of the pattern; P is the number of refined parameters and C is the number of constraints between the refined parameters.

2.5. Physical property measurements.

In order to perform some physical measurements materials were ground again and uniaxilly pressed under 300MPa pressure into pellets and bars as appropriate. The pellets and bars were sintered as described previously. Generally measurements were performed on materials of > 70-80 % density.

Table 2. *Summary of the densities for the materials characterised in the thesis.*

Materials	Density (%)
$Sr_{11}Mo_4O_{23}$	>90
$La_{1+x}Sr_{1-x}Ni_xAl_{1-x}O_4$	>90
$Bi_8Cr_7O_{22.5}$	>80
$Bi_{17}Cr_8Sr_7O_{44.5}$	>70

2.5.1. Two-probe method: AC Impedance Spectroscopy.

Two probe AC Impedance Spectroscopy measurements were performed using a Solartron 1255 B Frequency Response analyser and a Solartron 1297 electrochemical interface over the a frequency range of 10^{-1}-10^6 Hz. Prior to these measurements, the pellets were coated with platinum paste on opposite faces and mounted in a simple jig which was then

mounted in a furnace. This was then heated to 1073 K for 30 min to burn off the organic compounds and form platinum electrodes. Experiments were carried out in air from ambient temperature to 1073 K.

Impedance can be defined as the opposition of the material to alternative current. Impedance plots for electroceramic materials can be very complex, however for most of the cases studied two different components will be identified as intragrain (or bulk) and intergrain (or grain boundary) contributions. These contributions are most readily modelled as parallel resistanors (R) and capacitors (C) with the various components in series (Figure 6). Impedance data is generally presented as plots of the imaginary part, (Z'' which represents the capacitive part) versus the real part, (Z' which represents the resistive part) of the impedance. In the ideal case, each component mentioned above leads to a semicircular response.

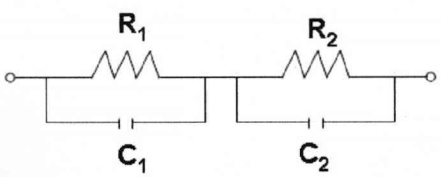

Figure 6. Schematic represenatation of the RC circuits studied in the materials.

R is defined as the resistance and C as the capacitance and they can be deduced from these Z" vs Z' plots. R is the intercepts on the Z' axis and C is obtained from the following relation:

$$\omega_{max} RC = 1 \qquad (2)$$

where ω is the frequency at the maximum of the semicircle.

Once the R and C have been determined, in order to assign the origin of the values it is generally useful in the first instance to compare the capacitance values with the values commonly found for various components (Table 3). The capacitance is also related to the relative permittivity and sample geometry by the relationship below:

$$C = \varepsilon' e_0 \frac{A}{l} \qquad (3)$$

where e_0 is the permittivity of free space, 8.854 x 10^{-14} F cm^{-1}.

Table 3. *Capacitance values and their possible interpretation*[21].

Capacitance (F)	Phenomenon Responsible
10^{-12}	bulk
10^{-11}	minor, second phase
10^{-11} - 10^{-8}	grain boundary
10^{-10} - 10^{-9}	bulk ferroelectric
10^{-9} - 10^{-7}	surface layer
10^{-7} - 10^{-5}	sample-electrode interface
10^{-4}	electrochemical reactions

For a material with unit dimensions (i.e. l/A = 1 cm^{-1}) and a typical relative permittivity of ~ 10 a capacitance value of ~ 1 x 10^{-12} F would be expected. This is indeed a typical value for the bulk capacitance of a sample.

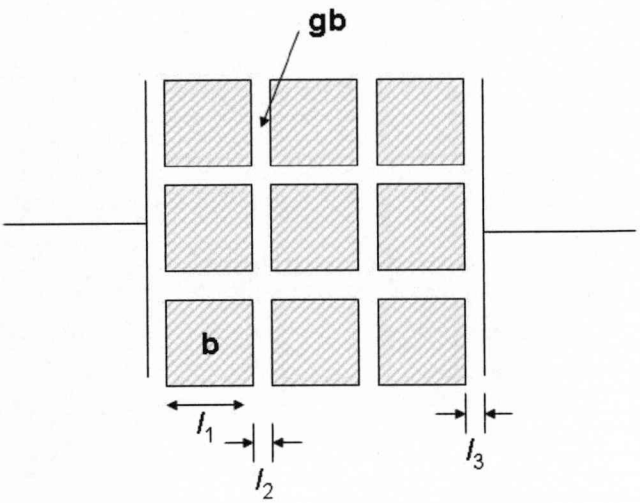

Figure 7. *Brickwork model of grain and grain boundary regions in a ceramic placed between metal electrodes*[21].

On the other hand, the grain boundary response is associated with capacitance values of 10^{-11}-10^{-8}. In order to understand this response, it is necessary to consider what an idealised ceramic with grains and grain boundaries would look like. Figure 7 shows the commonly accepted "brickwork" model in its most simple form it is made up of cube-shaped grains of dimensions l_1, separated from each other by a boundary of thickness l_2. It can be shown C_b and C_{gb}, the bulk and grain boundary capacitance respectively, are related by the following relation (assuming the relative permittivity is the same for the grain boundary and bulk):

$$\frac{C_b}{C_{gb}} = \frac{l_2}{l_1} \tag{4}$$

Thus a wide range of capacitance values from the grain boundary can be expected due to sample processing; relatively high capacitance values are expected for well sintered samples comprising large grains and few grain boundaries and low capacitance values from poorly sintered samples with small grains and many grain boundaries. These empirical relationships between the capacitance values and the origin of components can be very useful when assigning more complex plots where the individual components are not clearly separated.

2.5.2. Resistivity measurements.

The resistivity measurements were done using a four-probe method with a fixed current using a Solartron 1255 B Frequency Response analyser and a Solartron 1297 electrochemical interface. Prior to the DC resistivity measurements, the bars were mounted in a simple jig with four platinum electrodes (Figure 8) and placed into a furnace, which was heated to 1073 K for 30 min to burn off the organic compounds and form platinum electrodes.

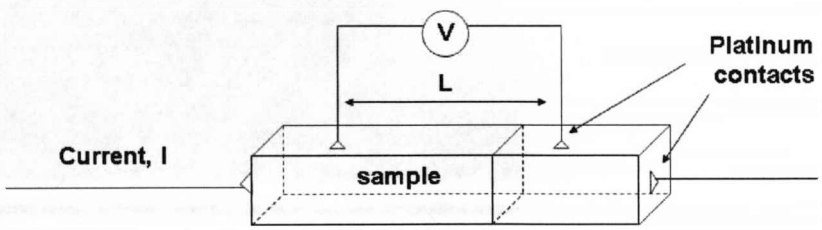

Figure 8. *Diagram showing the contacts used to do the resistivity measurements.*

The platinum wires under these contacts allow the current transit and measuring the induced voltage it is possible to calculate the resistance via Ohm's Law (Equation 5). The resistivity was measured in air from ambient temperature to 1073 K.

$$V = R \times I \tag{5}$$

$$\rho = \frac{A \times R}{L} \tag{6}$$

The resistivity is determined with the Equation 6 where A is the sample section (cm^2), L is the distance between the voltage contacts (cm) and R is the resistance (Ω).

2.6. Thermogravimetric Analysis (TGA).

Thermogravimetric analyses were performed in order to determine the materials' oxygen content or to monitor this as a function of temperature and oxygen partial pressures by monitoring the sample weight as a function of temperature. Measurements were carried out in oxidising atmospheres (O_2) or reducing atmospheres (5 % H_2/N_2).

Thermogravimetric analysis (TGA) was carried out for the materials on a differential thermal analysis instrument (EXSTAR6000). This instrument was calibrated using ZrO_2 as standard material.

2.7. X-ray Absorption Spectroscopy (XAS).

X-ray Absorption Spectroscopy (XAS) gives information about the oxidation states and the local environment of the atoms in the materials. XAS describes several techniques which involve the absorption by atoms of a particular element of X-rays with energies close to an absorption edge. The absorption is measured as a function of the incident photon energy.

EXAFS (Extended X-Ray absorption fine structure) spectroscopy uses the fine structure after the edge to obtain information about the quantity and type of atoms that are neighbours of the absorbing atoms. XANES (X-Ray absorption near edge structure) on the other hand uses the position of the edge and any pre-edge features to obtain information about the oxidation state of the elements.

X-ray absorption spectroscopy (XAS) was carried out on station 7.1 at the SRS, Daresbury Laboratories, UK[22]. The experiments were done at room temperature. The materials were mixed and ground with cellulose and the measurement performed in transmission mode. Standard samples were collected at regular intervals.

2.8. References

(1) Hagenmuller, P. *C. R. Acad. Sci II C.* **1999**, *2*, 537-545.

(2) Schaak, R. E.; Mallouk, T. E. *Chem. Mater.* **2002**, *14*, 1455-1471.

(3) Segal, D. *J. Mater. Chem.* **1997**, *7*, 1297-1305.

(4) *Matter website, Univeristy of Liverpool, http://www.matter.org.uk/diffraction/x-ray/x_ray_diffraction.htm*

(5) Harris, K. D. M.; Tremayne, M. *Chem. Mater.* **1996**, *8*, 2554-2570.

(6) Warren, B. E. *X-ray Diffraction; Dover Publications Inc* **1990**.

(7) Woolfson, M. W. *An Introduction to X-ray Crystallography; Cambridge University Press* **1997**.

(8) *http://pubs.usgs.gov/of/2001/of01-041/htmldocs/xrpd.htm.*

(9) Moron, M. C. *J. Mater. Chem.* **2000**, *10*, 2617-2626.

(10) *SRS Daresbury Laboratory website http://www.srs.ac.uk/srs/*

(11) *ISIS Rutherford Appleton Laboratory website http://www.isis.rl.ac.uk/.*

(12) Ibberson, R. M.; David, W. I. F.; Knight, K. S. *The High Resolution Neutron Powder Diffractometer (HRPD) at ISIS - A user guide* **1992**, Report RAL-92-031.

(13) Hull, S.; Smith, R. I.; David, W. I. F.; Hannon, A. C.; Mayers, J.; Cywinski, R. *Physica B: Phys Condens Matter* **2007**, 1000-1002.

(14) *Matter website, Univeristy of Liverpool, http://www.matter.org.uk/tem/default.htm.*

(15) Kilaas, R. *EMAT Laboratory, University of Antwerp, Belgium* **1996**.

(16) Rietveld, H. M. *Acta Crystallogr.* **1967**, *22*, 151-&.

(17) Rietveld, H. M. *J. Appl. Crystallogr.* **1969**, *2*, 65-&.

(18) Rodriguez-Carvajal, J. *Meeting, Toulouse, France* **1990**, *127*.

(19) Toby, B. H. *J. Appl. Crystallogr.* **2001**, *34*, 210-213.

(20) Sears, V. F. *Atomic Energy of Canada Limited, AECL (Report)* **1984**.

(21) Irvine, J. T. S.; Sinclair, D. C.; West, A. R. *Adv. Mater.* **1990** *2*, 132-138.

(22) SRS Daresbury Laboratory Station 7.1 website *http://srs.dl.ac.uk/xrs/stations/7.1.html.*

Chapter 3:

$Sr_2MgMoO_{6-\delta}$: structure, phase stability and cation site order control of reduction

3.1. Introduction.

Solid oxide fuel cells are of importance for stationary and distributed power generation at high thermodynamic efficiency, offering opportunities for efficient utilisation of both natural gas / hydrocarbons or hydrogen as a fuel. Current active materials chemistry research themes include reducing the cathode overpotential by enhancing oxide catalytic activity for oxygen reduction, identifying oxide ion conductors operating at low temperatures to reduce materials compatibility problems and identifying mixed oxide ion conductors with suitable chemical stability to reduction in H_2 or CH_4 at high temperature to function as anodes[1-4]. The double perovskite Sr_2MgMoO_6

has recently been shown to offer excellent performance as a fuel-cell anode[5-8] combining the required chemical stability, electronic and ionic conductivity and electrocatalytic activity in the highly reducing atmosphere of the fuel cell anode with resistance to poisoning by sulfur impurities in the fuel, a severe problem when considering the use of methane in the form of natural gas. The chemical and structural factors controlling the extent to which oxygen can be removed from Sr_2MgMoO_6 are important as removal of O under reducing conditions is required both for the introduction of anion vacancies to permit ionic conduction and for reduction of $5d^0$ Mo(VI) to $5d^1$ Mo(V) to generate electronic carriers. The original report shows Sr_2MgMoO_6 is a rock-salt B–site ordered double perovskite with Mo (VI) surrounded by six Mg^{2+} neighbors.

The work described in this chapter was undertaken in order to report the detailed structural chemistry of this material, particularly the chemical and structural changes which take place on reduction. This reveals the limited extent to which oxygen loss is possible in the pure material, and the interplay between structure and chemistry which permit reduction to occur. This work has been published[9].

3.2. Experimental.

Sr_2MgMoO_6 was prepared by direct reaction of MoO_3, MgO and $SrCO_3$ at 950°C for 15h. The powder was reground, pressed into pellets and refired at 1250 °C for 44h, with a second regrinding and pelletising and firing at 1350 °C for 44h (Sample I). Sample II was prepared by reduction in 5% H_2/N_2 at 800 °C for 18 h. Reduction of sample I at 1200 °C for 12 h in a flow of 5% H_2/N_2 gave samples III and IV which were brown/black in colour - IV was prepared on a smaller (1g) scale than III (5g). These conditions are similar to those used by Huang et al.[6,10] for the initial preparation of $Sr_2MgMoO_{6-\delta}$.

Structural characterisation of the materials were carried out using laboratory Power X-Ray Diffraction data (PXRD) collected on a Panalytical X'pert system using Co $K\alpha_1$ radiation in Bragg Brentano geometry. Time-of-flight (TOF) Power Neutron Diffraction data (PND) data were collected at ambient temperature on HRPD[11] and POLARIS[12] at ISIS. Data were refined by the Rietveld method[13,14] using the GSAS software package and EXPGUI interface[15]. In the case of all samples separate refinements were carried out against PXRD and the highest resolution TOF bank. Because of strong pseudo symmetry the least square refinements were carried out using the Levenberg-Marquardt algorithm rather than the Gauss-Newton algorithm, in order to obtain better convergence. The Stephens approach[16]

was applied to the anisotropic peak shapes in all cases. In the X-ray refinements, thermal parameters were fixed at 0.01Å^2 as was the oxygen content but Mg/Mo antisite disorder and a surface roughness absorption correction were refined. In the neutron refinements Mg/Mo antisite disorder was fixed at the value obtained for the X-ray refinement and the isotropic thermal parameters and anion vacancy concentrations were refined.

Samples for transmission electron microscopy were prepared by crushing the powder in *n*-butanol and the small crystallites in suspension were deposited onto a holey carbon film, supported by a copper grid. The electron diffraction (ED) study was carried out with a JEOL 2000FX electron microscope. Energy dispersive spectroscopy (EDS) analyses were systematically carried out during the ED study, the JEOL 2000FX being equipped with EDAX analyser. Thermal analysis (TGA) was performed using a Seiko SII-TG/DTA 6300 thermal analyzer.

3.3. Results.

In the case of sample I of Sr_2MgMoO_6 (air-fired), the powder X-ray diffraction data indicated the formation of a B-site ordered perovskite plus a trace amount of strontium molybdate ($SrMoO_4$). The sample was greenish white. Prior to the final anneal, significantly more strontium molybdate together with other unidentified impurities were present.

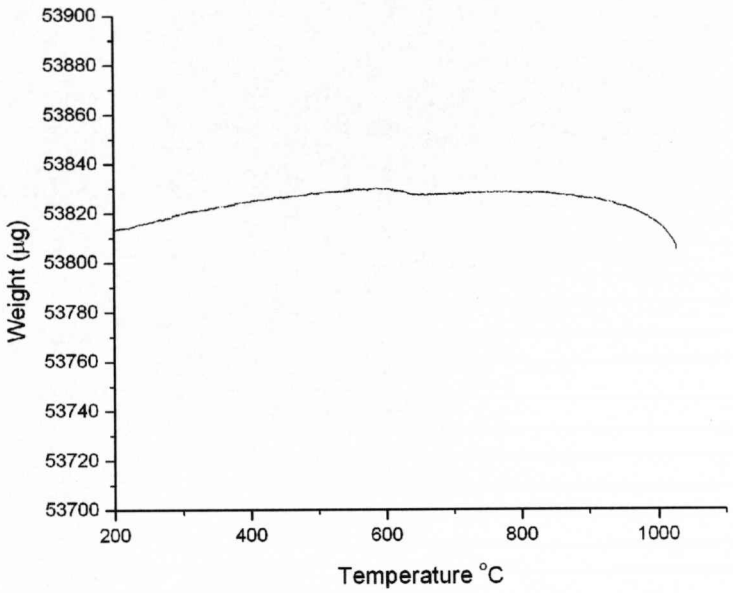

Figure 1. *Thermogravimetric analysis plot of the reduction for Sr_2MgMoO_6 in 5% H_2 in N_2.*

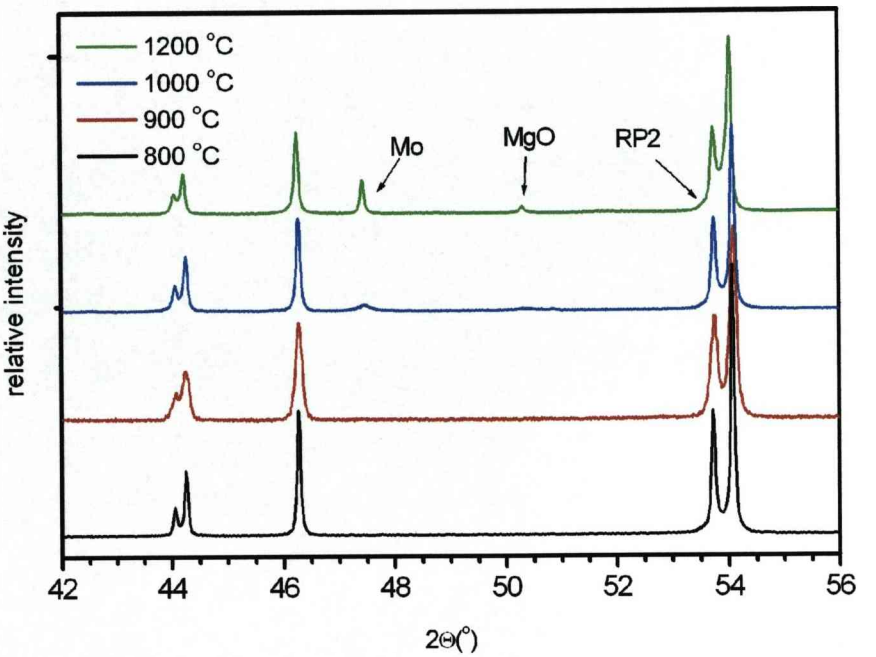

Figure 2. *Power X-Ray diffractograms for Sr_2MgMoO_6 reduced for 12h in flowing 5% H_2/N_2 between 800°C and 1200 °C. Peaks attributed to MgO and Mo are marked. The shoulder marked RP2 will be discussed below.*

Initial inspection of the PXRD data for sample III (reduced at 1200 °C for 12 hours) indicated that a degree of decomposition had occurred (peaks attributed to MgO and Mo were present in the pattern), therefore reduction at lower temperatures was investigated, initially by TGA measurement in a reducing atmosphere. Figure 1 shows that there was only a very minor weight loss starting at ~ 800 °C observed and that the reduction proceeded relatively slowly even up to 1100 °C, with a total of ~ 0.03 oxygen per Sr_2MgMoO_6 formula unit being lost in 1 hour. PXRD

showed that both the samples reduced at 800 °C and 900 °C did not contain any apparent MgO or Mo impurity peaks (Figure 2). In the light of this observation and the reported reduction of Sr_2MgMoO_6 at 800°C[6], a further sample was prepared by reduction in 5% H_2/N_2 at 800°C for 18 h (Sample II). Sample II was a darker green than the initial sample I but much paler than sample III.

Analysis of sample I (Sr_2MgMoO_6) by EDS confirmed its homogeneity and that the correct cation composition had been maintained in the synthesis. Reconstruction of the reciprocal space of Sr_2MgMoO_6 by electron diffraction revealed a cell of dimensions $\sqrt{2}a_p$ x $\sqrt{2}a_p$ x $2a_p$ with the body centering h + k + l = 2n reflection condition (Figure 3) inconsistent with the initially reported space group of $P2_1/n$ (0k0 k = 2n, h0l h + l = 2n). However due to the metrically tetragonal symmetry of the observed electron diffraction patterns, this leaves a large number of candidate space groups.

Identification of the correct structural description of Sr_2MgMoO_6 required comparative analysis of possible tetragonal, orthorhombic, monoclinic and triclinic models against the high resolution neutron powder diffraction data. This procedure is challenging due to the very pronounced pseudocubic symmetry. Refinement in I4/mmm, I4/m and Immm (χ^2=12.2) were all unsatisfactory. It was possible to converge a satisfactory refinement in I2/m (χ^2=1.7) but the model was inadequate from a crystal chemical viewpoint – analysis with isotropic displacement parameters in this space group only converges to χ^2 = 2.86, so anisotropic displacement parameters

are needed to match the observed intensities. This description produces a large discrepancy in the size and shape of the displacement ellipsoids of the two crystallographically distinct oxide anion sites in the I2/m structural description, with O2 having an equivalent isotropic ellipsoid four times the size of that of O1. This suggested that in I2/m O2 was accounting for more than one distinct anion site in the true structure. Refinements in I2 and Im were unsatisfactory, but analysis in $I\bar{1}$ (Figure 4 and Tables 1 & 2) gave superior agreement ($\chi^2 = 1.47$) as has been previously observed in a number of cases where the MO_6 octahedra are distorted[17,18], with only isotropic displacement parameters required at each site. The origin of this improvement is the splitting of the O2 site in I2/m to O2 and O2b in $I\bar{1}$. Attempts to model this instead by splitting the O2 site in I2/m yield less of an improvement than the $I\bar{1}$ model ($\chi^2 = 1.79$ *vs.* 1.47, 12 parameters refined in I2/m vs 52 parameters in $I\bar{1}$).

It is important to note that the unit cell of Sr_2MgMoO_6 is metrically tetragonal (all the angles are 90° within error; (b-a)/a is 10^{-4}, whereas (c-a)/a is 0.6×10^{-2}) so it is the intensities which decide the appropriateness of a structural model.

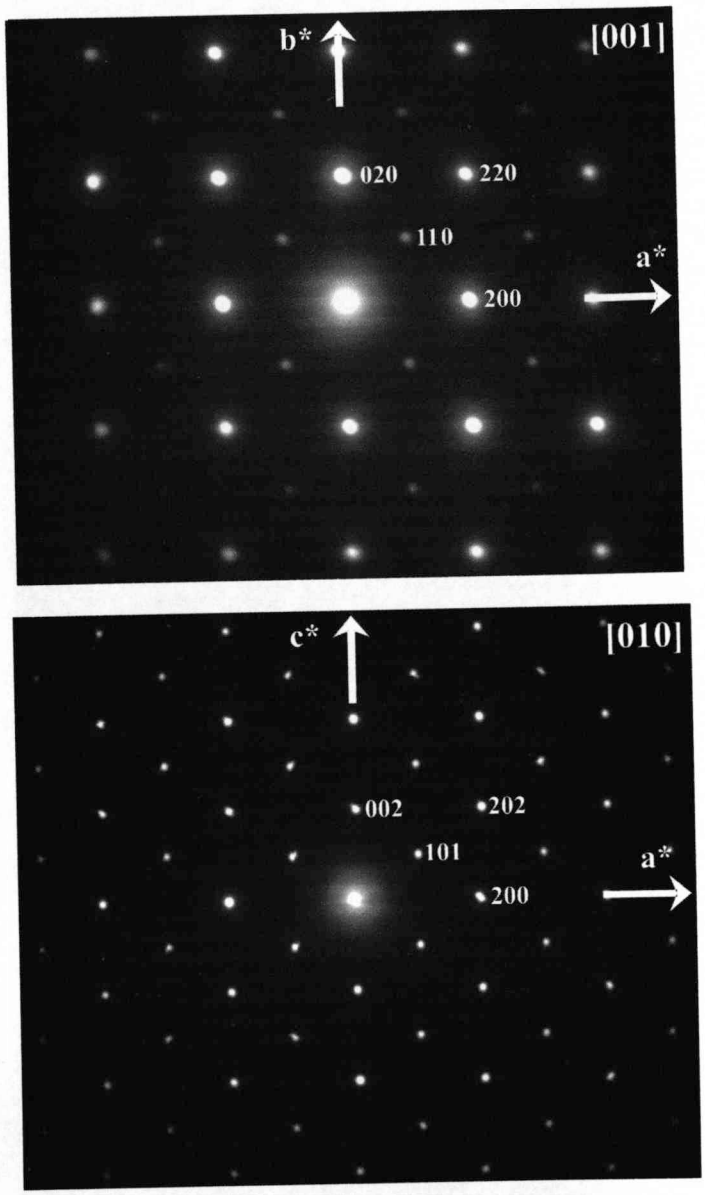

Figure 3. *Selected area electron diffractograms of the [001] and [010] projections of* Sr_2MgMoO_6*, showing systematic absences consistent with an I-centered cell.*

Neutron powder diffraction data are relatively insensitive to antisite disorder of Mg and Mo. The strong differences in X-ray scattering power makes X-ray powder diffraction more suitable to define the extent to which the strict alternation of Mg and Mo on the B sites is violated and thus a separate refinement against X-ray data was carried out. The results of both refinements are summarized in Tables 1 and 2.

In the case of sample II (800°C 5% H_2 in N_2) again there is a dominant double perovskite phase, in the PXRD data weak peaks for $SrMoO_4$ are visible but these are lost in the noise in the TOF neutron data and were thus not refined (Figure 5).

In the case of sample III (1200°C 5% H_2 in N_2) the powder X-ray diffraction data indicated the formation of a B-site ordered perovskite plus MgO, Mo and an unidentified impurity that appears as shoulders on some of the perovskite peaks (Figure 6). These impurity peaks are more prominent in the case of sample IV produced on a smaller scale under more reducing conditions (Figure 7). Analysis of the sample by EDS in the TEM for samples III and IV confirmed the presence of MgO and the homogeneity of the remaining crystallites indicating that $Sr_2MgMoO_{6-\delta}$, Mo and the new phase are intimately mixed on the EDS length scale (~ 100nm). Reconstruction of the reciprocal space of $Sr_2MgMoO_{6-\delta}$ by electron diffraction in the TEM revealed a cell of dimensions $\sqrt{2}a_p$ x $\sqrt{2}a_p$ x $2a_p$ with only the body centering h+k+l=2n reflection condition as for sample I prepared in air. In some crystallites, (Figure 8(a)) extra reflections were

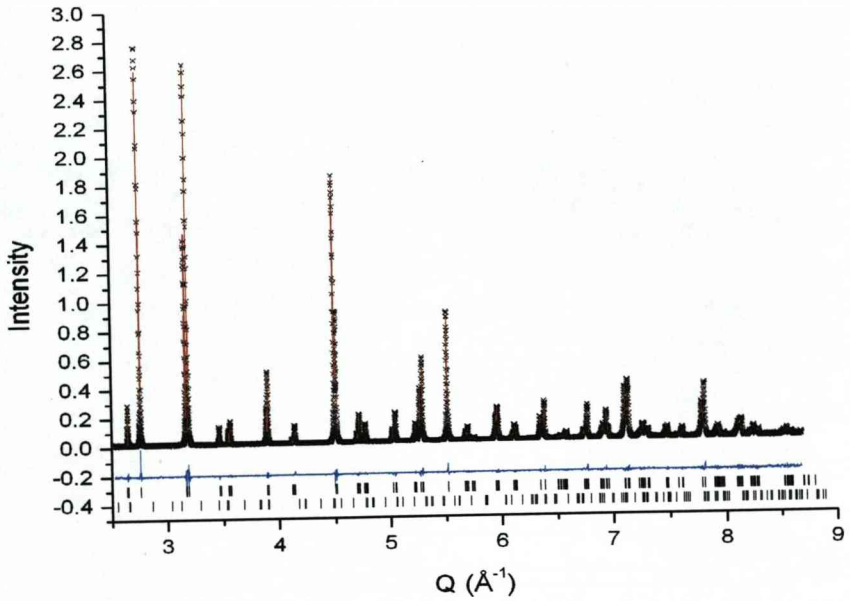

Figure 4. *Rietveld refinement of the backscattering bank neutron diffraction data from HRPD of sample I of Sr_2MgMoO_6. Crosses are observed data, the solid red line is the calculated pattern and the blue line is the difference. The upper set of tick marks correspond to the positions of the Bragg peaks for Sr_2MgMoO_6, and the lower set the positions of the Bragg peaks of the $SrMoO_4$ impurity.*

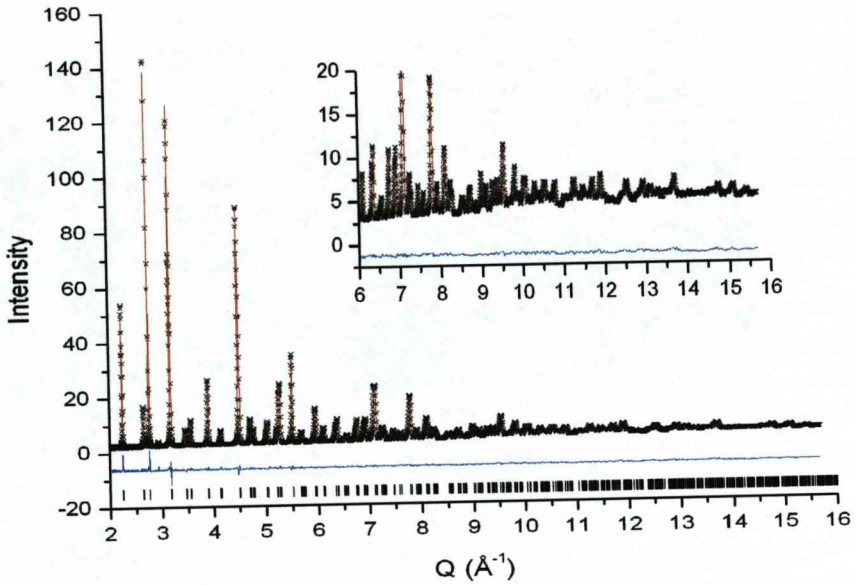

***Figure 5**. Rietveld refinement of the backscattering bank neutron diffraction data from Polaris of sample II of $Sr_2MgMoO_{6-\delta}$. The tick marks mark the positions of the Bragg peaks for $Sr_2MgMoO_{6-\delta}$. The inset shows the fit at high Q.*

Table 1. *Refinement parameters, refined cell constants and phase fractions (quoted in weight %) for the* $Sr_2MgMoO_{6\pm\delta}$ *present.*

	I			II			III	
	X-ray	**HRPD**		**X-ray**	**Polaris**		**X-ray**	**HRPD**
χ^2	4.118	1.469	χ^2	2.878	4.475	χ^2	5.777	5.088
R(F^2) (%)	4.34	4.55	**R(F^2) (%)**	5.11	4.93	**R(F^2) (%)**	4.3	6.59
***a*(Å)**	5.569321(14)	5.56666(2)	***a*(Å)**	5.56980(2)	5.56903(4)	***a*(Å)**	5.57151(1)	5.57299(3)
***b*(Å)**	5.569448(23)	5.56612(2)	***b*(Å)**	5.56958(2)	5.57042(4)	***b*(Å)**	5.57773(4)	5.57745(4)
***c*(Å)**	7.923445(24)	7.91916(2)	***c*(Å)**	7.92380(2)	7.92406(5)	***c*(Å)**	7.92034(4)	7.92129(5)
***α*(deg)**	89.961(1)	89.991(2)	***α*(deg)**	89.988(1)	89.977(6)	***α*(deg)**	89.892(1)	89.940(1)
***β*(deg)**	89.989(1)	89.972(1)	***β*(deg)**	89.999(2)	90.009(4)	***β*(deg)**	89.923(1)	90.024(1)
***γ*(deg)**	90.013(1)	89.996(2)	***γ*(deg)**	90.005(2)	90.0016(3)	***γ*(deg)**	89.923(1)	89.953(1)
***V*(Å^3)**	245.770(1)	245.373(1)	***V*(Å^3)**	245.808(1)	245.819(3)	***V*(Å^3)**	246.135(2)	246.218(3)
Phase fraction $Sr_2MoMgO_{6\pm\delta}$	98.866(1)	98.927(3)	**Phase fraction $Sr_2MoMgO_{6\pm\delta}$**	98.027(2)	100	**Phase fraction $Sr_2MoMgO_{6\pm\delta}$**	84.56(2)	86.24(3)
Phase fraction $SrMoO_4$	1.13(3)	1.07(3)	**Phase fraction $SrMoO_4$**	1.97(2)		**Phase fraction Mo**	1.47(2)	0.89(3)
						Phase fraction MgO	2.31(7)	1.17(2)
						Phase fraction $Sr_3(Mo_{(1-x)}Mg_x)_2O_{7-\delta}$	11.65(9)	11.13(9)

Table 2. *Refined atomic parameters for the $Sr_2MgMoO_{6\pm\delta}$ phase in samples I, II and III (fixed parameters are in italic)*[a].

	I		II		III	
	X-ray	**HRPD**	**X-ray**	**Polaris**	**X-ray**	**HRPD**
Sr1						
x	0.5026(5)	0.5019(5)	0.4946(3)	0.5023(4)	0.4894(2)	0.4955(4)
y	–0.0020(5)	–0.0009(8)	0.0050(3)	0.0016(3)	0.0025(2)	–0.0122(3)
z	0.2475(6)	0.2486(5)	0.2534(2)	0.2501(5)	0.2470(3)	0.2451(3)
U	0.0066(1)	0.01453(9)	*0.01*	0.00969(4)	*0.01*	0.0116(2)
Mo1						
U	0.0037(1)	0.00565(21)	*0.01*	0.00520(3)	*0.01*	0.0069(3)
F	0.992(1)	*0.992*	0.987(1)	*0.987*	0.933(1)	*0.933*
Mg1						
U	0.0037(1)	0.01635(31)	*0.01*	0.00520(3)	*0.01*	0.0097(4)
F	0.992(1)	*0.992*	0.987(1)	*0.987*	0.933(1)	*0.933*

[a]*Mo1 is on 2a (0,0,0) and Mg1 on 2b (1/2,1/2,0). The refined model has a total octahedra site occupancy of 1.00, with the difference from the refined fraction F quoted here made up by the occupancy of 1-F of Mg on Mo1 and Mo on Mg1.*

Table 2 cont. *Refined atomic parameters for the $Sr_2MgMoO_{6\pm\delta}$ phase in samples I, II and III (fixed parameters are in italic)*[a].

	I		II		III	
	X-ray	**HRPD**	**X-ray**	**Polaris**	**X-ray**	**HRPD**
O1						
x	–0.0274(9)	–0.0119(5)	–0.0266(14)	–0.006(1)	–0.015(2)	0.0006(9)
y	0.0013(10)	0.0065(9)	0.0249(15)	–0.0153(2)	0.009(3)	0.0127(5)
z	0.2414(4)	0.2448(2)	0.2404(3)	0.2470(3)	0.2311(7)	0.2464(5)
U	*0.01*	0.01687(7)	*0.01*	0.01193(7)	*0.01*	0.0143(3)
O2						
x	0.2577(9)	0.2733(3)	0.2854(8))	0.2665(2)	0.225(1)	0.2749(4)
y	0.2090(10)	0.2143(3)	0.2194(9)	0.2263(2)	0.281(2)	0.2207(4)
z	–0.0079(4)	–0.0044(5)	0.0092(18)	–0.0080(2)	0.023(1)	–0.0012(5)
U	*0.01*	0.01687(7)	*0.01*	0.01269(8)	*0.01*	0.0143(3)
O2b						
x	–0.2193(11)	–0.2237(3)	–0.2164(10)	–0.2147(1)	–0.261(1)	0.2249(4)
Y	0.2857(10)	0.2665(4)	0.2443(10)	0.2751(2)	0.220(1)	0.2525(5)
Z	–0.0159(13)	0.0078(3)	0.0173(11)	–0.0080(2)	–0.021(1)	–0.011035
U	*0.01*	0.01687(7)	*0.01*	0.00520(3)	*0.01*	0.024(4)
F	*1*	*1*	*1*	0.993(2)	*1*	0.977(5)

Table 3. *Refined parameters for the $Sr_3(Mo_{1-x}Mg_x)_2O_{7-\delta}$ Ruddlesden-Popper impurity phase in sample III.*

	x	y	z	occupancy
Sr1	0	0	0.5	1
Sr2	0	0	0.3005(5)	1
Mo1	0	0	0.1058(5)	0.784(12)
O1	0	0	0	0.49(3)
O2	0	0	0.1904(6)	1
O3	0	½	0.1025(4)	1

Space group I4/mmm a = 3.9527(2)Å c = 20.436(5)Å V = 319.29(8) $Å^3$ overall U=0.01(1)$Å^2$. x = 0.215(9) δ = 0.49(3).

observed as well as streaking and diffuse features along $(001)_{perov}$ (Figure 8(b)-(d)). The strongest extra reflections in both neutron and X-ray powder data are characteristic of an n=2 Ruddlesden - Popper phase, and the observed shoulders occur close to the peak positions expected for $Sr_3Mo_2O_7$[19,20]. This is consistent with electron diffraction patterns revealing streaking along c* in the perovskite (Figure 8(b)), the coexistence of perovskite and n=2 Ruddlesden-Popper unit cells (Figure 8(c)) and patterns solely indexable by the n=2 Ruddlesden-Popper phase with streaking along the layer stacking direction (Figure 8(d)).

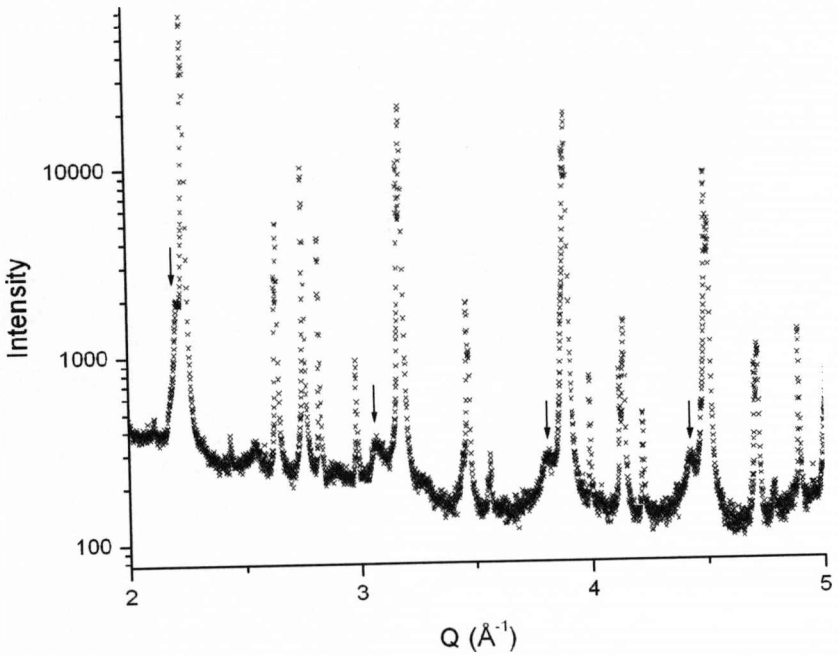

Figure 6. *Powder X-ray diffraction data for sample III of* $Sr_2MgMoO_{6-\delta}$ *reduced at 1200 °C. The arrows indicate the shoulders on peaks attributed to the n=2 Ruddlesden-Popper phase.*

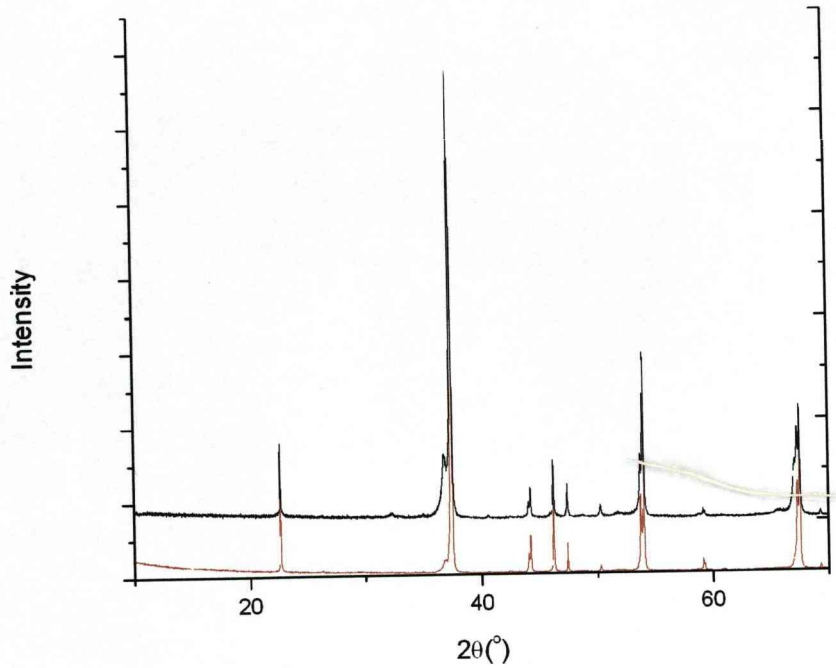

Figure 7. *Comparison of the XRD data of Sample III (red) and IV (black). Sample IV was prepared on a smaller scale and with O_2 more rigorously excluded from the reducing gas stream.*

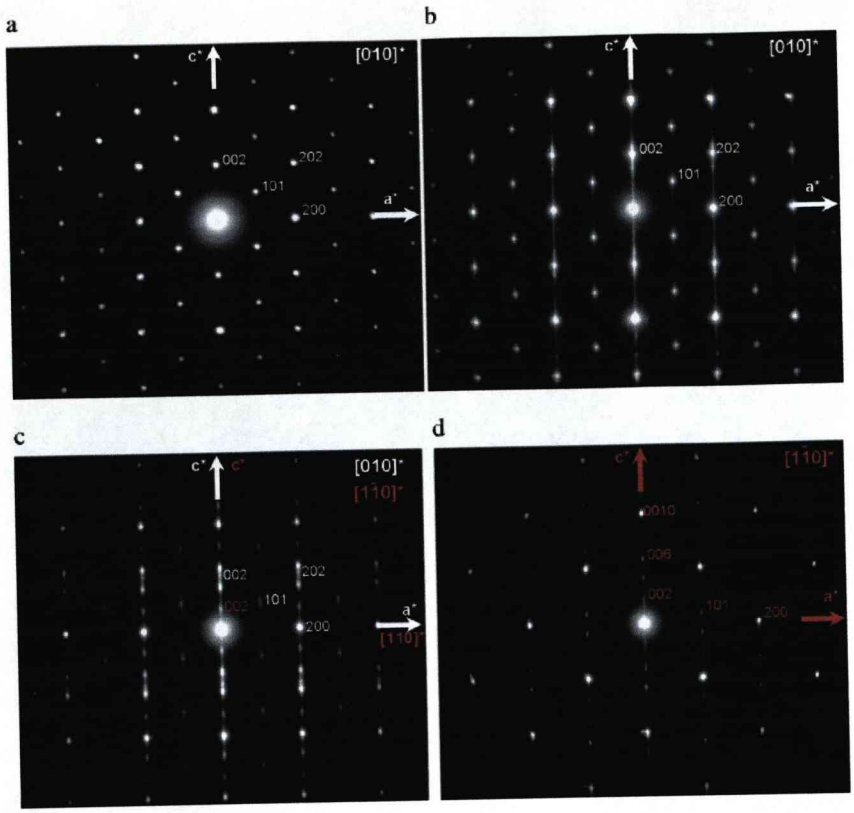

Figure 8. *Selected area electron diffractograms for $Sr_2MgMoO_{6-\delta}$ sample IV reduced at 1200 °C. White indices refer to the unit cell of the $Sr_2MgMoO_{6-\delta}$ perovskite phase and red to the RP n = 2 phases, showing:* ***(a)*** *[010] projection of $Sr_2MgMoO_{6-\delta}$ perovskite alone* ***(b)*** *[010] projection of $Sr_2MgMoO_{6-\delta}$ with prominent streaking along (001).* ***(c)*** *[010] projection of $Sr_2MgMoO_{6-\delta}$ intergrown with the [1$\bar{1}$0] projections of an RP n=2 phase. Prominent streaking along (001) in both phases is obvious.* ***(d)*** *[1$\bar{1}$0] projection of an RP n=2 phase, with streaking along (001).*

Refinements of the neutron and X-ray diffraction data from sample III which did not include the RP second phase did not give satisfactory fits. (χ^2 = 8.595 for the HRPD backscattering bank). Both X-ray and TOF neutron refinements improved on addition of the RP phase (χ^2 = 5.088 for the HRPD backscatter bank) (Figure 9). Refined parameters for the RP phase from analysis of the HRPD data are given in Table 3. An overall thermal parameter was used in both neutron and X-ray refinements, Mo/Mg ratios on the octahedral site were refined in the X-ray data and fixed in the neutron refinement, where the anion occupancies were varied. The RP phase B site cation composition in the neutron refinement was fixed at the value obtained from the X-ray data, and only the phase fractions and the anion occupancies were varied as detailed above. The refined cation ratios in the entire multiphase assemblage in sample III can be calculated from the refined phase fractions. The overall Sr:Mo:Mg ratios from the X-ray and neutron refinements were 1:0.57:0.53 and 1:0.54:0.52 respectively, close to the theoretical values of 1:0.5:0.5.

a

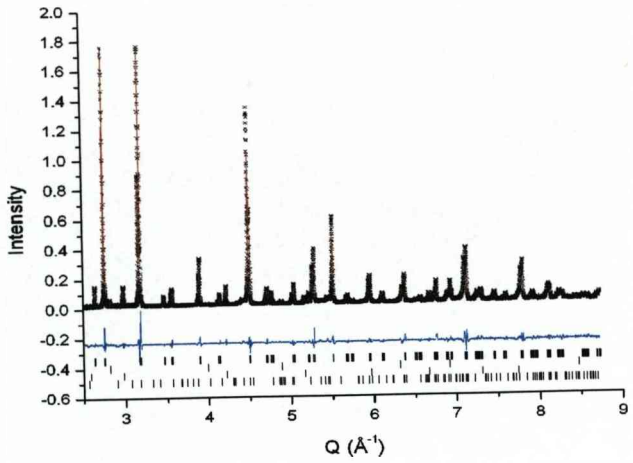

b

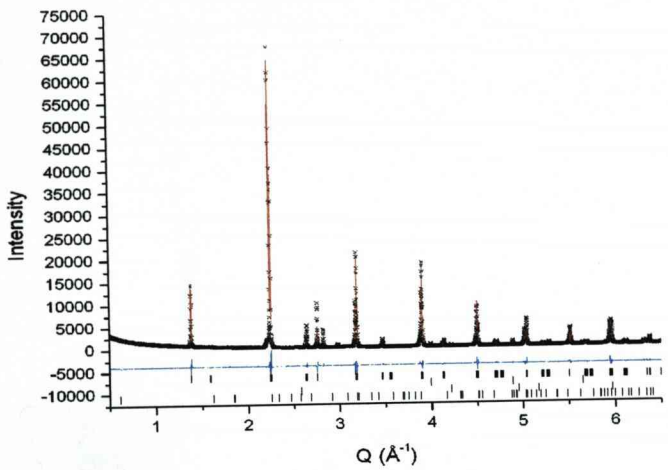

Figure 9. *Rietveld refinement plots of sample III of* $Sr_2MgMoO_{6-\delta}$ *reduced at 1200 °C (a) backscattering bank neutron diffraction data from HRPD and (b) powder X-ray diffraction data, represented as in Figure 3(a). The tick marks show the Bragg peaks for, from top to bottom,* $Sr_2MgMoO_{6-\delta}$*, Mo, MgO and the n=2 RP phase* $Sr_3(Mo_{(1-x)}Mg_x)_2O_{7-\delta}$ *(*$x = 0.215(9)$*).*

3.4. Discussion.

Figure 10 shows views down the principle axes of the cubic perovskite subcell for Sr_2MgMoO_6. Table 4 summarizes the octahedral cation bond lengths for all three samples as well as the cation bond valence sums[21] and octahedral distortion parameter ($\Sigma(r-r_{mean})^2$). It can be clearly seen that there is an obvious c^- tilt with little or no tilt on the other axes. Thus for the tilt system $a^0a^0c^-$ we would expect that the structure would adopt the tetragonal space group I4/m[22,23] in the absence of any octahedral distortions. Using the program SPUDS[22] (Table 5) it is possible to estimate the relative stability of various tilt systems. It can be seen from Table 5 one might expect either the tilt system $a^-b^+a^-$ ($P2_1/n$) or $a^-a^-a^-$ ($R\bar{3}$). However, Sr_2MgMoO_6 adopts the tilt system $a^0a^0c^-$ with octahedral distortions reducing the tetragonal tilt-based symmetry to triclinic. The underlying tilt system is consistent with the I4/m structure of the Sr-based rock-salt ordered double perovskite Sr_2FeMoO_6[24].

Sr_2MgMoO_6 appears to contain more local strain than Sr_2MnMoO_6[25] where the Mo bond valence sum is 5.77, and the mean square distortion at the Mo octahedral site is 4.27×10^{-5}. This supports the suggestion that the symmetry-lowering from I4/m is driven by octahedral distortion.

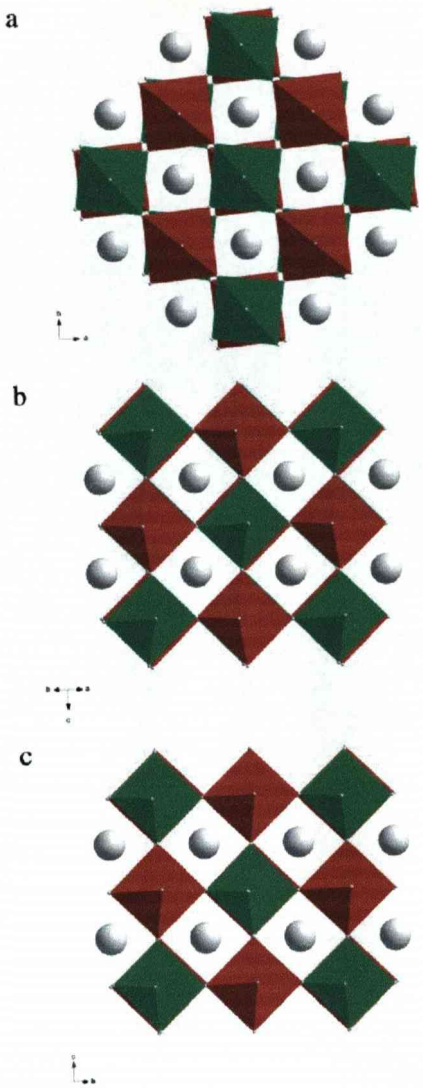

***Figure 10**. Refined structure of Sr_2MgMoO_6 (sample I) obtained from the HRPD data viewed along (a)[001], (b)[110] and (c) [$1\bar{1}0$]. Grey spheres are Sr, red octahedra are Mg-centered and green octahedra are Mo-centered.*

Table 4. *Refined bond lengths, Calculated Bond Valence Sums[21] and Octahedral Distortion ($\Sigma(r\text{-}r_{mean})^2$) at the Octahedral Sites of $Sr_2MgMoO_{6-\delta}$ (refined oxygen deficiency is given in the final row) on the Basis of Refinements against the Neutron Data*

Bond (Å)	I	II	III
Mo1_O1 x 2	1.9403(18)	1.9602(28)	1.953(4)
Mo1_O2 x 2	1.9335(19)	1.9475(10)	1.9662(23)
Mo1_O2b x 2	1.9376(20)	1.9424(9)	1.8866(27)
Mg2_O1 x 2	2.0221(17)	2.0059(28)	2.010(4)
Mg2_O2 x 2	2.0305(18)	2.0062(10)	2.0008(23)
Mg2_O2b x 2	2.0147(20)	2.0260(8)	2.0639(27)
Mo BVS	5.53(4)	5.34(4)	5.58(8)
Mg BVS	2.46(2)	2.53(2)	2.35(3)
Sr BVS	2.06(2)	2.05(2)	2.04(2)
$(\Sigma(r\text{-}r_{mean})^2)$ Mo-O	0.0000241	0.000187	0.004583
$(\Sigma(r\text{-}r_{mean})^2)$ Mg-O	0.000125	0.000392	0.00299
δ	0	0.014(2)	0.046(10)

Table 5. *Predicted tilt systems for 1:1 ordered Sr_2MgMoO_6 in the absence of octahedral distortions.*

Tilt System	Space group (undistorted octahedral)	Global Instability Index (valence units)
$a^+a^+a^+$	$Pn\bar{3}$	0.04236
$a^-b^+a^-$	$P2_1/n$	0.0003
$a^-a^-a^-$	$R\bar{3}$	0.00009
$a^0b^-b^-$	$I2/m$	0.00685
$a^0a^0c^+$	$P4/mnc$	0.02075
$a^0a^0c^-$	$I4/m$	0.02075
$a^0a^0a^0$	$Fm\bar{3}m$	0.13952

Figure 11 shows the response of Sr_2MgMoO_6 to reduction. Both the unit cell volume and the cation occupancy disorder on the octahedral site correlate well with the refined oxygen deficiency (δ = 0, 0.014(2) and 0.046(10) with corresponding values of the octahedral disorder of 0.008(2), 0.013(1) and 0.057(1) for samples I-III respectively). It should also be noted that it is a consistent feature of the Rietveld refinements that only one of the three oxygen sites (O2b) appears to be depleted. The mean square distortion at the octahedral Mo and Mg sites increases systematically with the amount of reduction.

The observation that disorder of the octahedral sites correlates almost quantitatively with the number of oxide anion vacancies is particularly interesting. This could be interpreted as the avoidance of low coordination numbers for Mg, for which coordination numbers of less than 6 are rare in oxides. If we consider only antisite disorder, each swap of cation pairs (to produce Mg on an Mo site and Mo on an Mg site) produces

five Mg-O-Mg linkages and five Mo-O-Mo linkages (Figure 12(a) and 12(b)). The creation of the Mo-O-Mo linkages thus produces oxide anions that are coordinated purely to Mo. Removal of these anions will produce only five-coordinate Mo(V), which is well-established, removing the necessity to propose the formation of five-coordinate Mg^{2+} in an oxide. The observed correlation between oxide vacancy content and cation site order is thus chemically justifiable. However, only Mo-O2b-Mo linkages appear to be reduced according to the site occupancy refinements in each case. This is consistent with the observation that the Mo-O2b distance is the most sensitive of all the Mo-O distances to reduction (Figure 13(a)).

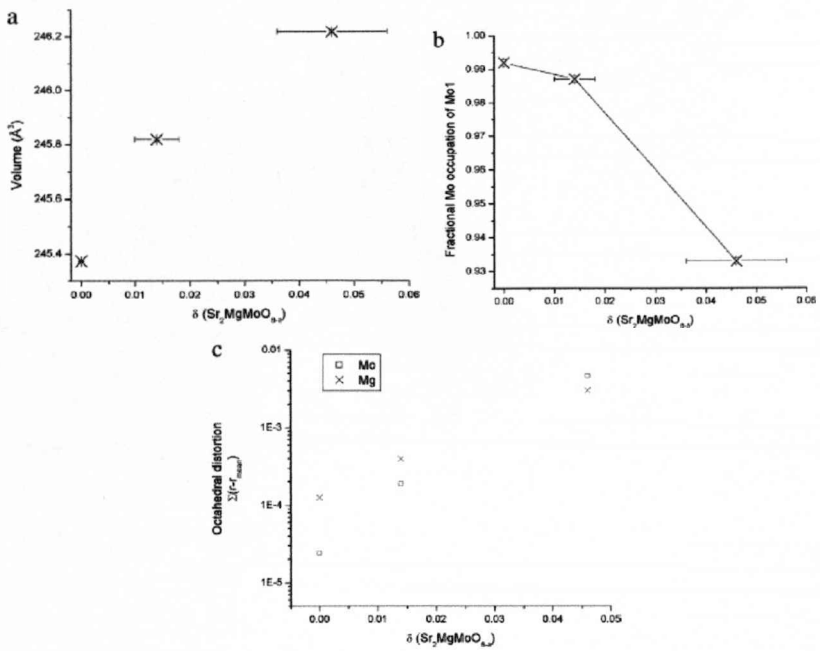

Figure 11. *Plots of the correlation of refined parameters for* $Sr_2MgMoO_{6-\delta}$ *with refined vacancy concentration* δ *(a) unit cell volume against refined oxygen content (sample I is assumed to be stoichiometric in oxygen); (b) The octahedral distortion parameter* $(\Sigma(r\text{-}r_{mean})^2$*; (c) fractional Mo occupancy of the Mo1 site vs. refined oxygen content.*

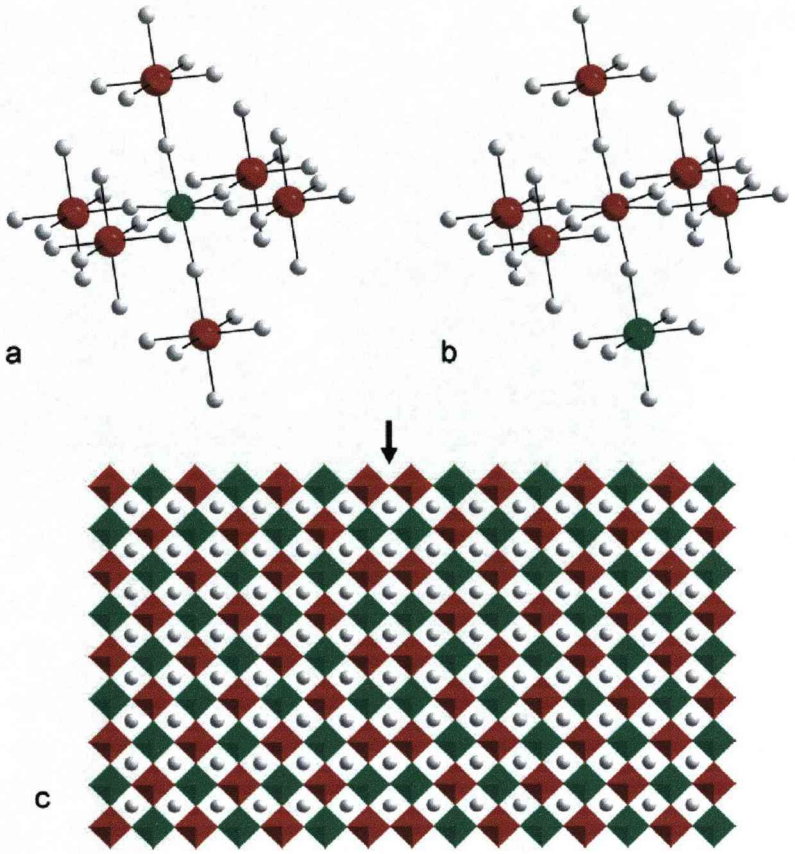

Figure 12. *Schematic illustration of models for antisite disorder in* $Sr_2MgMoO_{6\pm\delta}$ *(a) Molybdenum (green) surrounded by six next nearest neighbour magnesium (red) in a perfectly B-site ordered material; oxygens are white and strontium cations are omitted for clarity. (b) Situation after a single molybdenum-magnesium B-site swap. There are now five unfavourable next nearest neighbour interaction per cation. (c) Schematic representation of a* $[100]_{perov}$ *antiphase extended defect indicated with an arrow; red octahedra are magnesium centered and green molybdenum centred. Note that in this case only one unfavourable next nearest neighbour interaction per cation is introduced.*

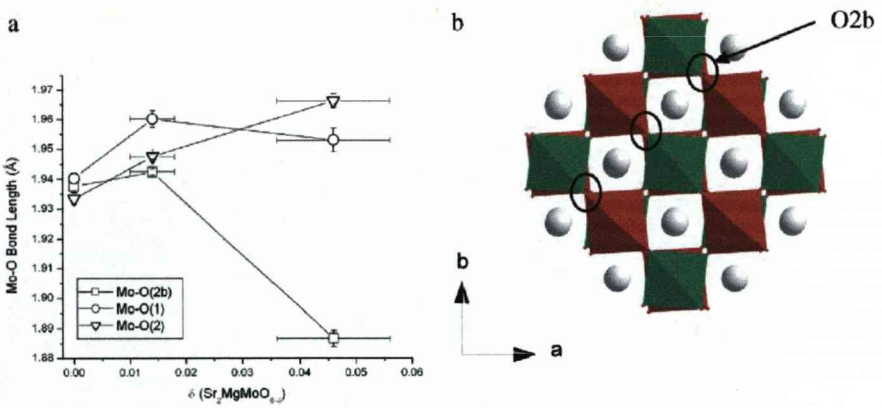

Figure 13. *(a) The three crystallographically distinct Mo-O distances in* $Sr_2MgMoO_{6-\delta}$ *versus refined oxygen stoichiometry (b) The structure of* $Sr_2MgMoO_{6-\delta}$ *viewed along [001] showing the location of O2b which lies in [100] planes within the perovskite subcell.*

It has been argued in similar B-site ordered perovskites that apparent antisite disorder is primarily due to stacking faults at which there is a phase shift in the cation occupancies and the resulting formation of antiphase domain boundaries[26]. In the case of $A_2BB'X_6$ systems[27], considered in terms of a $2a_p$ x $2a_p$ x $2a_p$ cell which for $Sr_2MgMoO_{6\pm\delta}$ would represent an $F\bar{1}$ cell ($a' = a + b$, $b' = a - b$, $c' = c$), both [100] and [110] antiphase boundaries (within this F-centred cell) conserve the cation composition whilst generating Mo-O-Mo sites where reduction would occur along the boundary where the cation pairs are concentrated. This is illustrating schematically in Figure 12(c). Extended defects of this type would reduce the number of electrostatically unfavourable interactions per cation. Note that the aggregation of oxide vacancies upon reduction to form extended defects has been used to explain the metallic conductivity of $SrTiO_3$ even at very low

degrees of reduction, as it permits a connected pathway between the reduced transition metal centers[28].

It can also be seen in Table 4 and Figure 11(c) that the octahedral distortion of both Mg and Mo increase with extent of reduction, although Mo increases more rapidly. One possible explanation for this can be seen in Figure 13(b), where the largest change in bond lengths occurs between Mo and O2b. The enhanced sensitivity of the Mo-O2b distance to the extent of reduction correlates with the enhanced vacancy concentration refined at this site. It should be noted that the O2b sites lie along one [001] plane in the $F\bar{1}$ cell. This is consistent with the removal of oxide anions in a manner correlated with the formation of extended defects within this plane. The presence of significant amounts of such [001] antiphase boundaries is also consistent with the observed streaking in Figure 8(b), in the absence of observable R-P = 2 type intergrowth superstructure spots discussed in the next paragraph. The compositional and electron diffraction evidence is thus consistent with the formation of extended arrays of antisite defects which would minimise both the formation of five-coordinate Mg and unfavorable local cation pairings due to isolated antisite disorder, whilst creating extended electronic conduction paths through the sample.

Reduction of Sr_2MgMoO_6 at high temperature produces a change in the observed phase assemblage driven by the formation of an n = 2 Ruddlesden-Popper phase. Figure 14 shows the derived structural model of $Sr_3(Mo_{(1-x)}Mg_x)_2O_{7-\delta}$ (x = 0.215(9), δ = 0.49(3)). The exact nature of this phase is unclear, in the absence of the observation of distinct grains of the segregated RP phase by EDX, and the significant broadening of the peaks

for both perovskite and RP Sr-Mg-Mo-O phases in sample III. (The Stephens anisotropic strain parameters for the perovskite phase are 5 to 10 times greater in sample III as compared to sample I). The complex streaking in the electron diffraction patterns recorded from sample III (Figure 8) indicate the true nature of the phase assemblage is more complex. It is thus likely that the secondary RP phase is significantly intergrown with the perovskite phase given the significant refined phase fraction, though the observation of distinct Bragg reflections from the n=2 RP structure in Figure 8(d) indicates that there are some coherent domains. The X-ray refinements show that these intergrowths are Mo-rich with a B-site composition of $Mo_{0.785(9)}Mg_{0.215(9)}$. Importantly, this B-site composition combined with the refined fraction for all four phases in the complex assemblage is consistent with the overall cation composition Sr_2MgMo. The neutron data show that these Ruddlesden-Popper intergrowths are significantly reduced, and accommodate reduction to a level beyond that possible in the perovskite phase: this can be attributed to the enhanced Mo content which permits the removal of oxygen without the formation of five coordinate Mg^{2+}. The refined $Sr_3(Mo_{0.785(9)}Mg_{0.215(9)})_2O_{6.51(3)}$ composition gives a molybdenum oxidation state be close to Mo^{IV}, which is chemically sensible given the existence of $Sr_3Mo_2O_7$ and the Zn^{2+}-containing phase $Sr_3Mo_{1.5}Zn_{0.5}O_{6.75}$[29]. This reduced character and oxygen deficiency lead to the expectation that the n = 2 Ruddlesden-Popper phase or intergrowths would have significant electronic and ionic conductivities. This phase is further discussed in chapter 5.

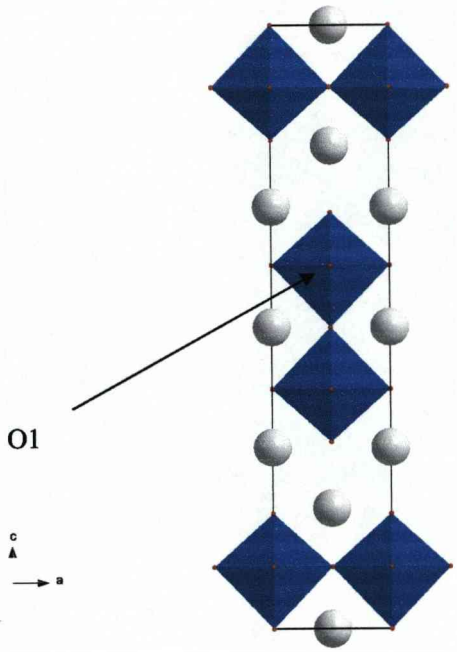

Figure 14. *Refined structure of the n = 2 Ruddlesden-Popper phase* $Sr_3(Mo_{1-x}Mg_x)_2O_{7-\delta}$ *(x = 0.215(9), δ = 0.49(3)) (sample III) obtained from the HRPD data viewed along [010]. O1 is labeled to show the location of the oxygen vacancies. (Bond lengths Mo1-O1 1 x 2.163(10) Å Mo1-O2 1 x 1.729(15)Å Mo1-O3 4 x 1.977).*

3.5. Conclusions.

Sr_2MgMoO_6 adopts an $I\bar{1}$ structure derived from an $a^0a^0c^-$ tilt system related to that of Sr_2FeMoO_6 *via* distortion of the Mg and Mo centered octahedra. Reduction of the perovskite Sr_2MgMoO_6 is possible only to a limited extent despite the stability of lower Mo oxidation states than +VI,

which is attributed to the difficulty of forming five coordinate Mg^{2+} in the perovskite structure. The extent of reduction that is possible within the perovskite appears correlated with antisite disorder of the Mo and Mg cations, which permits the removal of oxide anions while only reducing the coordination number of Mo. The assimilation of point antisite defects into extended structures analogous to anti-phase domain boundaries would minimize unfavorable electrostatic interactions arising from antisite defect formation and permit the correlated removal of oxide anions. Upon further reduction at temperatures > 900°C $Sr_2MgMoO_{6\pm\delta}$ assumes a higher O vacancy content but begins to decompose into a reduced material modeled as an n = 2 phase with a significantly higher Mo:Mg ratio, MgO and Mo, and a lower Mo oxidation state. One plausible model of the reduction would thus involve initial reduction associated with extended antisite defects followed by decomposition at these defects by excision of BO_6 octahedral layers neighboring the defect, yielding intergrowth of an RP=2 material in a perovskite matrix.

The reactivity of $Sr_2MgMoO_{6\pm\delta}$ suggests other approaches to the formation of fuel cell anodes for SOFC's. Molybdenum metal, or under some of the feed conditions tested molybdenum carbide[30] or sulphide[31], is likely to be catalytically active as potentially is the intergrowth of $Sr_3(Mo_{(1-x)}Mg_x)_2O_{7-\delta}$. In order to understand the observed behaviour of $Sr_2MgMoO_{6\pm\delta}$ cathodes further detailed studies of the phase assemblies in working electrodes are required in order to understand the exact roles of the different potential components. The temperature dependences of the structures of these phases will be discussed in the next chapter and the

synthesis of $Sr_3(Mo_{(1-x)}Mg_x)_2O_{7-\delta}$ and related Ruddlesden-Popper phases is discussed in chapter 5.

3.6. References.

(1) Lashtabeg, A.; Skinner, S. J. *J, Mater. Chem.* **2006**, *16*, 1.

(2) Shao, Z.; Haile, S. M.; Ahn, J.; Ronney, P. D.; Zhan, Z.; Barnett, S. A. *Nature* **2005**, *435*, 795-798.

(3) McIntosh, S.; Gorte, R. J. *Chem. Rev.* **2004**, *104*, 4845-4865.

(4) Tao, S.; Irvine, J. T. S. *Nature Materials* **2003**, *2*, 320-323.

(5) Huang, Y. H.; Dass, R. I.; King, Z. L.; Goodenough, J. B. *Science* **2006**, *312*, 254-257.

(6) Huang, Y. H.; Dass, R. I.; Denyszyn, J. C.; Goodenough, J. B. *J. Electrochem. Soc.* **2006**, *153*, A1266-A1272.

(7) Goodenough, J. B.; Huang, Y. H. *J. Power Sources* **2007**, *173*, 1-10.

(8) Ji, Y.; Huang, Y. H.; Ying, J. R.; Goodenough, J. B. *Electrochem. Commun.* **2007**, *9*, 1881-1885.

(9) Bernuy-Lopez, C.; Allix, M.; Bridges, C. A.; Claridge, J. B.; Rosseinsky, M. J. *Chem. Mater.* **2007**, *19*, 1035-1043.

(10) Huang, Y. H.; Dass, R. I.; Xing, Z. L.; Goodenough, J. B. *Science* **2006**, *312*, 254-257.

(11) Ibberson, R. M.; David, W. I. F.; Knight, K. S. *The High Resolution Neutron Powder Diffractometer (HRPD) at ISIS - A user guide* **1992**, Report RAL-92-031.

(12) Hull, S.; Smith, R. I.; David, W. I. F.; Hannon, A. C.; Mayers, J.; Cywinski, R. *Physica B: Phys. Condens. Matter* **2007**, 1000-1002.

(13) Rietveld, H. M. *J. Appl. Crystallogr.* **1969**, *2*, 65-&.

(14) Rietveld, H. M. *Acta Crystallogr.* **1967**, *22*, 151-&.

(15) Toby, B. H. *J. Appl. Crystallogr.* **2001**, *34*, 210-213.

(16) Stephens, P. W. *J. Appl. Crystallogr.* **1999**, *32*, 281-289.

(17) Battle, P. D.; Goodenough, J. B.; Price, R. *J. Solid State Chem.* **1983**, *46*, 234-244.

(18) Ohashi, Y.; Finger, L. W. *Am. Mineral.* **1978**, *63*, 274-288.

(19) Shirakawa, N.; Ikeda, S. I. *Physica C* **2000**, *341-348*, 783-784.

(20) Steiner, U.; Reichelt, W. *Z. Natursforsch. B* **1998**, *53*, 110-116.

(21) Brown, I. D. *Acta Crystallogr. B* **1977**, *33*, 1305-1310.

(22) Lufaso, M. W.; Barnes, P. W.; Woodward, P. M. *Acta Crystallogr. B* **2006**, *62*, 397-410.

(23) Howard, C. J.; Kennedy, B. J.; Woodward, P. M. *Acta Crystallogr. B* **2003**, *59*, 463-471.

(24) Shimada, T.; Nakamura, J.; Motohashi, T.; Yamauchi, H.; Karppinen, M. *Chem. Mater.* **2003**, *15*, 4494-4497.

(25) Azad, A. K.; Eriksson, S. G.; Ivanov, S. A.; Mathieu, R.; Svedlindh, P.; Eriksen, J.; Rundlo?f, H. *J. Alloys Compd.* **2004**, *364*, 77-82.

(26) Ting, V.; Liu, Y.; Nore?n, L.; Withers, R. L.; Goossens, D. J.; James, M.; Ferraris, C. *J. Solid State Chem.* **2004**, *177*, 4428-4442.

(27) Woodward, P.; Hoffmann, R. D.; Sleight, A. W. *J. Mater. Res.* **1994**, *9*, 2118-2127.

(28) Szot, K.; Speier, W.; Carius, R.; Zastrow, U.; Beyer, W. *Phys. Rev. Lett.* **2002**, *88*, 755081-755084.

(29) Steiner, U.; Reichelt, W.; Schmidt, M.; Schnelle, W. Z. *Anorg. Allg. Chem.* **2004**, *630*, 649-654.

(30) Claridge, J. B.; York, A. P. E.; Brungs, A. J.; Marquez-Alvarez, C.; Sloan, J.; Tsang, S. C.; Green, M. L. H. *J. Catal.* **1998**, *180*, 85-100.

(31) Osaki, T.; Horiuchi, T.; Suzuki, K.; Mori, T. *Catal. Lett.* **1995**, *35*, 39-43.

Chapter 4:

Phase transition in the double perovskite $Sr_2MgMoO_{6-\delta}$ by in situ high temperature neutron powder diffraction study

4.1. Introduction.

In the previous chapter, we reported that Sr_2MgMoO_6 adopts an $I\bar{1}$ structure derived from an $a^0a^0c^-$ tilt system via distortion of the Mg- and Mo-centered octahedra[1]. Reduction of Sr_2MgMoO_6 appears to be correlated with antisite disorder either at point or extended anti-phase defects.

Perovskite oxides may undergo several phase transitions at high temperature as has been observed in $A_{2-x}Sr_xNiWO_6$ (A = Sr, Ba, Ca), Sr_2MWO_6 (M = Ni, Zn, Co, Cu)[2,3], Sr_2FeMoO_6[4], Sr_2CoMoO_6[5] and Sr_2NiMoO_6[6]. Both first and second order phase transitions have been

observed in double perovskite. In the case of $A_{2-x}Sr_xNiWO_6$ and Sr_2MWO_6 (M = Ni, Zn, Co) a second order transition was observed from the tetragonal I4/m space group ($a^0a^0c^-$ tilt system) to the cubic $Fm\bar{3}m$ space group ($a^0a^0a^0$ tilt system). In the related compound Sr_2FeMoO_6, a transition was reported from the cubic $Fm\bar{3}m$ space group to the tetragonal I4/m space group at low temperature. The same transition was observed in the compound Sr_2CoMoO_6. However in Sr_2CuWO_6[3] compound, a second-order transition was observed from the tetragonal I4/m space group to the I4/mmm space group, at higher temperatures a first order transition was observed from this tetragonal I4/mmm space group to the cubic $Fm\bar{3}m$ space group. Several theoretical studies have been performed on these double perovskite showing the different possible symmetry changes and whether they would be expected to be first or second order transitions. Scheme 1 shows the possible transitions the possible tilt schemes for double perovskites[7,8].

Detailed understanding of the possible phase transitions in $Sr_2MgMoO_{6-\delta}$ at elevated temperatures are very important to allow a good electrolyte/anode interface to be achieved when fabricating and operating the cell at high temperature. In this chapter, it will be shown that $Sr_2MgMoO_{6-\delta}$ undergoes at high temperature phase transition to a cubic $Fm\bar{3}m$ phase at 200 °C and thermal expansion data will be presented.

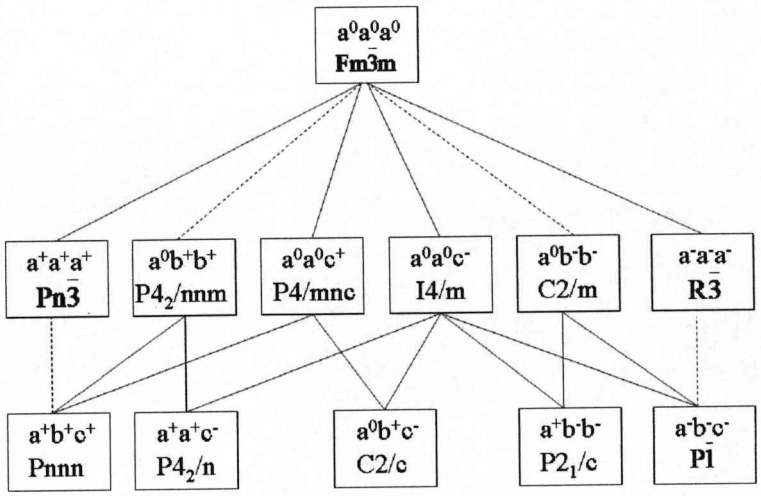

Scheme 1. *Scheme indicating the group-subgroup relationships among different tilt systems for double perovskites. "+", "0" and "−" symbols represent the tilt direction. A dashed line joining a group to its subgroup indicates that the corresponding phase transition is required by Landau theory to be first order* [9].

4.2. Experimental.

Sample preparation and analysis strategies are detailed in section 3.2. In addition the oxygen content was fixed at the value obtained previously at ambient conditions for the data collected on Polaris[10] and refined for the data collected on HRPD[11].

Measurements were performed starting at room temperature, the temperature was then increased 100 °C, and held for an hour. Data between 100 and 800 °C were then collected at 50 °C intervals to 500 °C and then

100 °C intervals until 800 °C, holding at each temperature for 1h to reach equilibrium before data collection.

4.3. Results.

In the previous chapter it was shown that $Sr_2MgMoO_{6-\delta}$ adopts a $\sqrt{2}$ a_p x $\sqrt{2}$ a_p x 2 a_p $I\bar{1}$ superstructure of the simple perovskite cell, derived from an $a^0a^0c^-$ tilt system via distortion of the Mg- and Mo- centred octahedra that adopted a I4/m space group.

Diffraction data for sample II of $Sr_2MgMoO_{6-\delta}$ indicated the formation of a B-site ordered perovskite without any other significant impurities. In the case of sample III of $Sr_2MgMoO_{6-\delta}$ XRD data showed the formation of that same B-site ordered perovskite plus some impurities peaks identified as MgO, Mo and a new Ruddlesden-Popper n=2 phase of general formula $Sr_3(Mg_xMo_{(1-x)})_2O_{7-\delta}$. It was demonstrated in that work that both materials adopts the same $I\bar{1}$ structure but they are different in their level of Mg/Mo antisite disorder and their level of oxygen vacancies. Both factors are correlated and the level of reduction is possible only to a limited extent despite the stability of lower Mo oxidation states than +VI, which is attributed to the difficulty of forming five coordinated Mg^{2+} in the perovskite structure. This correlation permits the removal of oxide anions while only reducing the coordination number of Mo.

Data were collected for Sample II and Sample III and in the temperature range of room temperature to 150 °C can be refined using the

triclinic structure for the double perovskite. The NPD pattern for sample II at 150 °C is shown in Figure 1. Figure 1(b) shows the splitting of the peaks at ~1.98 Å and ~2.38 Å characteristic of this $I\bar{1}$ structure. Lattice parameters and fit parameters are summarised in Table 1 and Table 2 for sample II and sample III respectively. The refined structure parameters for sample II are shown in Table 3. In the case of the sample III the quality of the data was not sufficient to refine the structural parameters freely though good fits were obtained using the values obtained at ambient temperature.

Table 1. *Refined parameters and refined cell constant for* $Sr_2MgMoO_{6-\delta}$ *sample II at room temperature, 100 °C, 125 °C and 150 °C.*

	RT (HRPD)	**100 °C (HRPD)**	**125 °C (HRPD)**	**150 °C (HRPD)**
wRp (%)	8.33	10.30	19.12	6.83
Rp (%)	7.32	9.34	16.17	5.93
χ^2	1.280	1.243	1.225	1.331
a (Å)	5.568691 (70)	5.577370 (50)	5.579843 (942)	5.584812 (31)
b (Å)	5.571660 (73)	5.578465 (47)	5.579872 (937)	5.584200 (30)
c (Å)	7.925181 (44)	7.923924 (50)	7.923060 (87)	7.923365 (35)
α (deg)	89.952 (2)	89.978 (3)	90.021 (11)	90.007 (4)
β (deg)	90.024 (3)	90.010 (6)	89.973 (9)	89.972 (1)
γ (deg)	90.028 (1)	90.020 (2)	90.020 (3)	90.015 (1)
V ($Å^3$)	245.893 (2)	246.538 (3)	246.683 (4)	247.104 (2)

Table 2. *Refined parameters and refined cell constant for* $Sr_2MgMoO_{6-\delta}$ *sample III at room temperature, 150 °C and 175 °C.*

	RT (HRPD)	**150 °C (HRPD)**	**175 °C (HRPD)**
wRp (%)	8.33	18.96	19.38
Rp (%)	7.31	16.14	16.73
χ^2	1.277	1.224	1.246
a (Å)	5.568694 (69)	5.582231(166)	5.585063 (170)
b (Å)	5.571659 (73)	5.587976 (179)	5.590425 (175)
c (Å)	7.925178 (44)	7.922843 (156)	7.923978 (153)
α (deg)	89.951 (2)	89.934 (3)	89.925 (3)
β (deg)	90.023 (3)	90.030 (4)	89.953 (4)
γ (deg)	90.027 (1)	89.960 (3)	89.947 (2)
V (Å^3)	245.893 (2)	247.140 (7)	247.409 (9)

a

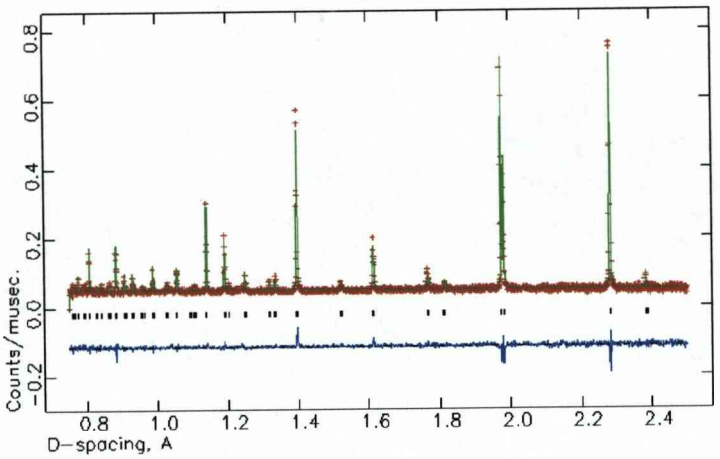

b

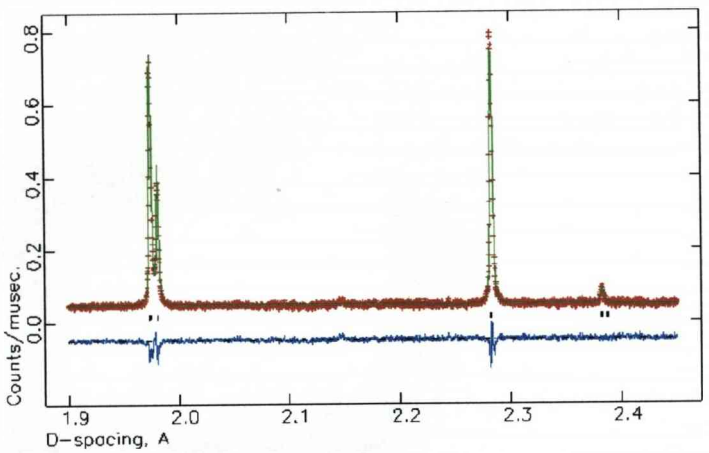

Figure 1. *(a) Rietveld refinement of the backscattering bank neutron diffraction data from HRPD of sample II of* Sr_2MgMoO_6 *measured at 150* ^oC*. Crosses are observed data, the solid red line is the calculated pattern and the pink line is the difference. The upper set of tick marks correspond to the positions of the Bragg peaks for* $Sr_2MgMoO_{6-\delta}$*. (b) Zoom of the refinement at high d-spacing showing the splitting of the peak at ~1.98 Å and showing the peak at ~2.38 Å.*

Table 3. *Refined atomic parameters for the $Sr_2MgMoO_{6-\delta}$ samples II (fixed parameters are in italic) at room temperature, 100 °C and 150 °C. Mo1 is on 2a (0,0,0) and Mg1 on 2b (1/2,1/2,0). The refined model has a total octahedral site occupancy of 1.00, with the difference from the refined fraction F quoted here made up by occupancy of 1-F of Mg on Mo1 and Mo on Mg1.*

	RT (HRPD)	**RT (Polaris)**	**100 °C (HRPD)**	**150 °C (HRPD)**
Sr1				
x	0.5052 (20)	0.5023 (4)	0.4985 (19)	0.5008 (15)
y	–0.0017 (20)	0.0016 (3)	0.0002 (32)	0.0021 (14)
z	0.2539 (14)	0.2501 (5)	0.2500 (53)	0.2506 (19)
U	0.0087 (7)	0.00969 (4)	0.0236 (3)	0.0010 (2)
Mo1				
U	0.0044 (6)	0.00520 (3)	0.0166 (3)	0.0014 (2)
F	*0.987*	*0.987*	*0.987*	*0.987*
Mg1				
U	0.0044 (6)	0.00520 (3)	0.0166 (3)	0.0014 (2)
F	*0.987*	*0.987*	*0.987*	*0.987*
O1				
x	–0.0020 (36)	–0.006 (1)	–0.0159 (13)	–0.0116 (10)
y	0.0172 (14)	–0.0153 (2)	0.0086 (24)	0.0104 (11)
z	0.2457 (11)	0.2470 (3)	0.2478 (16)	0.2467 (10)
U	0.0091 (7)	0.01193 (7)	0.0255 (2)	0.0107 (4)

***Table 3 cont.**. Refined atomic parameters for the $Sr_2MgMoO_{6-\delta}$ samples II (fixed parameters are in italic) at room temperature, 100 °C and 150 °C. Mo1 is on 2a (0,0,0) and Mg1 on 2b (1/2,1/2,0). The refined model has a total octahedral site occupancy of 1.00, with the difference from the refined fraction F quoted here made up by occupancy of 1-F of Mg on Mo1 and Mo on Mg1.*

	RT (HRPD)	RT (Polaris)	100 °C (HRPD)	150 °C (HRPD)
O2				
x	0.2709 (14)	0.2665 (2)	0.2713 (11)	0.2601 (8)
y	0.2264 (20)	0.2263 (2)	0.2274 (11)	0.2304 (6)
z	–0.0051 (15)	–0.0080 (2)	–0.0023 (29)	–0.0004 (28)
U	0.0091 (7)	0.01269 (8)	0.0255 (2)	0.0090 (4)
O2b				
x	–0.2147 (15)	–0.2147 (1)	–0.2242 (11)	–0.2184 (5)
y	0.2724 (16)	0.2751 (2)	0.2690 (13)	0.2684 (7)
z	0.0077 (19)	–0.0080 (2)	0.0096 (98)	0.0125 (5)
U	0.0091 (7)	0.00520 (3)	0.0255 (2)	0.0103 (5)
F	0.913 (14)	0.993 (2)	1.000 (7)	*0.987*

Subsequent structural refinement from neutron powder diffraction (NPD) data collected for both samples in the range of temperatures 200-300 °C shows a transition from the triclinic $I\bar{1}$ space group to the cubic $Fm\bar{3}m$ space group without any intermediate phase between those phases. Figure 2 shows cell volume at the temperature range of coexistence for both triclinic and cubic phase in Sample II. Figure 3 shows the NPD pattern for the sample II at 250 °C where it can be clearly seen how the peak at ~2.38 Å decreases in intensity and the splitting of the peak at ~1.98 Å is greatly

reduced. The refined phase fractions are listed in Table 4 for sample II. It can be seen how the cubic phase becomes richer in phase fraction as the temperature increases. Similar behaviour is also observed in sample III (Table 5). Table 6 and 7 show the refined structural parameters for the triclinic and cubic phases respectively for sample II. At 300 °C the structure parameters of the $I\bar{1}$ phase could not be refined due to its low phase fraction (5.85 % vs. 94.15 % of the cubic phase). In the case of sample III the quality of the data were not good enough to refine the structure. The atomic positions were fixed and only the cell parameters and phase fractions were refined.

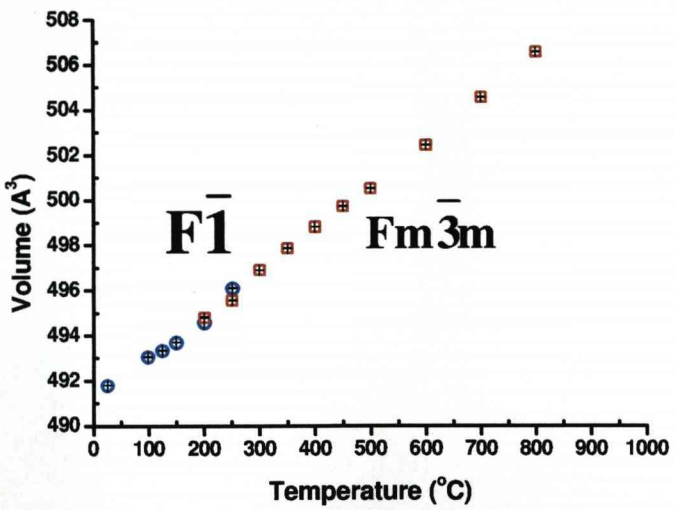

Figure 2. *Representation of the double volume versus the temperature sample II of* $Sr_2MgMoO_{6-\delta}$ *for both triclinic* $F\bar{1}$ *(blue) and cubic* $Fm\bar{3}m$ *(red) phases.*

Table 4. *Refined parameters and refined cell constant for sample II of* $Sr_2MgMoO_{6-\delta}$ *in the range of temperature where the transition was observed.*

	200 °C Triclinic phase (HRPD)	**200 °C Cubic phase (HRPD)**	**250 °C Triclinic phase (HRPD)**	**250 °C Cubic phase (HRPD)**	**300 °C Triclinic phase (HRPD)**	**300 °C Cubic phase (HRPD)**
%	91.77 (40)	8.23 (40)	48.70 (64)	51.30 (64)	5.85 (30)	94.15 (30)
wRp (%)	14.79	14.79	7.66	7.66	6.84	6.84
Rp (%)	12.45	12.45	6.93	6.93	5.91	5.91
χ^2	1.151	1.151	1.321	1.321	1.325	1.325
a (Å)	5.588611 (68)	7.911223 (283)	5.593009 (96)	7.913436 (36)	---	7.920477 (16)
b (Å)	5.585576 (62)		5.596250 (98)			
c (Å)	7.922728 (72)		7.923906 (105)			
α (deg)	90.020 (3)		89.975 (4)			
β (deg)	89.955 (2)		90.071 (2)			
γ (deg)	90.030 (2)		90.071 (2)			
V ($Å^3$)	247.313 (4)	495.143 (53)	248.017 (6)	495.559 (7)	---	496.883 (3)

Table 5. *Refined parameters and refined cell constant for sample III of* $Sr_2MgMoO_{6-\delta}$ *in the range of temperature where the transition was observed.*

	200 °C Triclinic phase (HRPD)	**200 °C Cubic phase (HRPD)**	**225 °C Triclinic phase (HRPD)**	**225 °C Cubic phase (HRPD)**	**250 °C Triclinic phase (HRPD)**	**250 °C Cubic phase (HRPD)**
%	96.32 (20)	3.68 (20)	95.58 (41)	4.42 (36)	91.46 (78)	8.54 (39)
wRp (%)	10.43	10.43	19.72	19.72	19.59	19.59
Rp (%)	8.95	8.95	16.46	16.46	16.56	16.56
χ^2	1.343	1.343	1.314	1.314	1.284	1.284
a (Å)	5.589939 (103)	7.936852 (360)	5.592795 (180)	7.937972 (543)	5.593716 (138)	7.936549 (334)
b (Å)	5.591910 (108)		5.592994 (179)		5.597630 (138)	
c (Å)	7.923536 (124)		7.922269 (224)		7.922899 (174)	
α (deg)	90.051 (3)		90.011 (23)		90.039 (4)	
β (deg)	90.016 (6)		90.020 (12)		90.040 (4)	
γ (deg)	89.966 (3)		89.986 (10)		89.963 (3)	
V (Å^3)	247.677 (7)	499.971 (68)	247.812 (13)	500.183 (103)	248.078 (10)	499.914 (63)

a

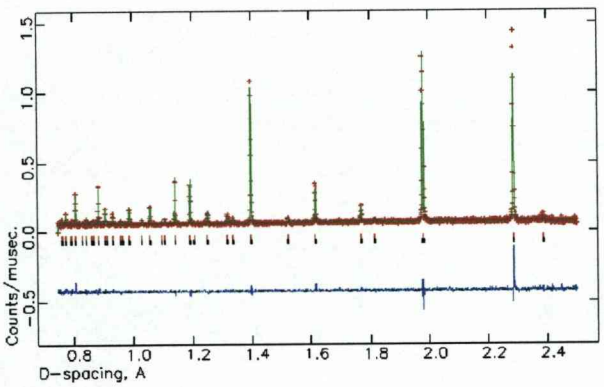

b

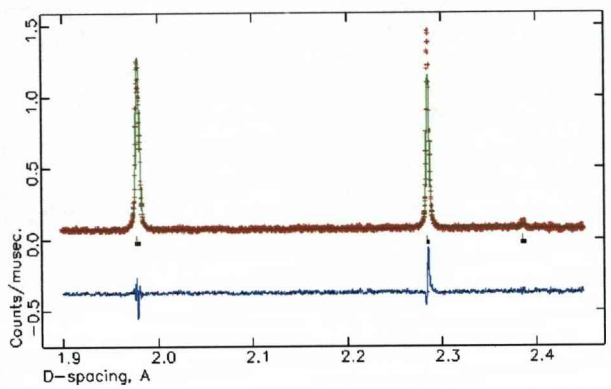

Figure 3. *(a) Rietveld refinement of the backscattering bank neutron diffraction data from HRPD of sample II of* $Sr_2MgMoO_{6-\delta}$ *at 250 °C. Crosses are observed data, the solid red line is the calculated pattern and the pink line is the difference. The upper set of tick marks correspond to the positions of the Bragg peaks for the* $Fm\bar{3}m$ *phase and the bottom set of tick marks correspond to the* $I\bar{1}$ *phase. (b) Zoom of the refinement at high d-spacing showing the loss of the splitting of the peak at ~1.98 Å and showing that the peak at ~2.38 Å is weaker than before the transition.*

Table 6. *Refined atomic parameters for the $Sr_2MgMoO_{6-\delta}$ samples II $I\bar{1}$ phase (fixed parameters are in italic) at the range of temperatures where the transitions is observed. Mo1 is on 2a (0,0,0) and Mg1 on 2b (1/2,1/2,0). The refined model has a total octahedral site occupancy of 1.00, with the difference from the refined fraction F quoted here made up by occupancy of 1-F of Mg on Mo1 and Mo on Mg1.*

	200 °C (HRPD)	**250 °C (HRPD)**
Sr1		
x	0.4990 (18)	0.5011 (27)
y	–0.0024 (24)	0.0018 (26)
z	0.2488 (27)	0.2494 (23)
U	0.0133 (4)	0.0257 (5)
Mo1		
U	0.0083 (5)	0.0073 (4)
F	*0.987*	*0.987*
Mg1		
U	0.0083 (5)	0.0073 (4)
F	*0.987*	*0.987*
O1		
x	–0.0125 (16)	–0.0213 (16)
y	0.0125 (18)	0.0172 (17)
z	0.2465 (18)	0.2493 (43)
U	0.0187 (3)	0.0294 (4)
O2		
x	0.2637 (14)	0.2706 (14)
y	0.2360 (15)	0.2324 (15)
z	–0.0062 (15)	0.0013 (56)
U	0.0187 (3)	0.0294 (4)
O2b		
x	–0.2273 (12)	–0.2238 (14)
y	0.2704 (12)	0.2727 (14)
z	0.0131 (9)	0.0058(15)
U	0.0183 (3)	0.0294 (4)
F	1.000 (11)	1.031 (14)

Table 7. *Refined atomic parameters for the $Sr_2MgMoO_{6-\delta}$ samples II $Fm\bar{3}m$ phase (fixed parameters are in italic) at the range of temperatures where the transitions is observed.*

	200 °C (HRPD)	**250 °C (HRPD)**	**300 °C (HRPD)**
Sr1			
U	0.0334 (57)	0.0238 (4)	0.0140 (3)
Mg1			
U	0.0187 (52)	0.0217 (5)	0.0035 (3)
Mo1			
U	0.0187 (52)	0.0217 (5)	0.0035 (3)
O1			
x	0.2564 (40)	0.2577 (3)	0.2593 (2)
U	0.0181 (27)	0.0234 (3)	0.0139 (2)
F	0.999 (33)	0.970 (4)	*0.95*

NPD data collected in the range of temperatures of 350-800 °C contained only a single double perovskite phase and were successfully refined in $Fm\bar{3}m$. Table 8 and Table 10 show the agreement factors and lattice for samples II and sample III respectively. Figure 4 and Figure 5 show NPD pattern at 500 °C for sample II and at 600 °C for sample III. It can be seen that the peak at ~2.38 Å has completely disappeared and the splitting of the peak at ~1.98 Å disappeared. Table 9 and Table 11 show the refined structural parameters for both sample II and sample III respectively.

Figure 6 shows the phase fractions of both samples as a function of temperature. The phase fractions for the R-P n=2 $Sr_3(Mg_xMo_{1-x})_2O_{7-\delta}$ phase observed as secondary phase in sample III remains constant at high temperature.

Table 8. *Refined parameters and refined cell constant for sample II of* $Sr_2MgMoO_{6-\delta}$ *at temperatures above the transition:*

	350 °C (HRPD)	**400 °C (HRPD)**	**450 °C (HRPD)**	**500 °C (HRPD)**	**600 °C (HRPD)**	**700 °C (HRPD)**	**800 °C (HRPD)**
wRp (%)	6.9	6.83	18.49	7.8	7.67	7.97	7.83
Rp (%)	5.94	5.87	15.63	6.88	6.51	6.78	6.7
χ^2	1.342	1.312	1.029	1.275	1.255	1.334	1.287
a (Å)	7.925602 (15)	7.930654 (34)	7.935553 (39)	7.939712 (22)	7.949841 (22)	7.960935 (50)	7.971466 (50)
V (Å^3)	497.848 (3)	498.800 (6)	499.725 (7)	500.512 (4)	502.430 (4)	504.536 (9)	506.541 (9)

Table 9. *Refined atomic parameters for the $Sr_2MgMoO_{6-\delta}$ samples II (fixed parameters are in italic) in the cubic $Fm\bar{3}m$ space group at temperatures above the transition.*

	350 °C (HRPD)	400 °C (HRPD)	450 °C (HRPD)	500 °C (HRPD)	600 °C (HRPD)	700 °C (HRPD)	800 °C (HRPD)
Sr1							
U	0.0161 (3)	0.0177 (4)	0.0154 (10)	0.0234 (8)	0.0313 (9)	0.0350 (10)	0.0316 (10)
Mg1							
U	0.0058 (3)	0.0064 (3)	0.0024 (9)	0.0112 (8)	0.0177 (9)	0.0198 (10)	0.0159 (10)
Mo1							
U	0.0058 (3)	0.0064 (3)	0.0024 (9)	0.0112 (8)	0.0177 (9)	0.0198 (10)	0.0159 (10)
O1							
x	0.2599 (2)	0.2598 (2)	0.2594 (6)	0.2593 (3)	0.2592 (3)	0.2592 (3)	0.2596 (3)
U	0.0159 (3)	0.0169 (3)	0.0133 (8)	0.0233 (10)	0.0310 (11)	0.031 (12)	0.0303 (13)
F	*0.95*	*0.95*	*0.95*	0.954 (10)	0.962 (11)	0.944 (12)	0.938 (12)

a

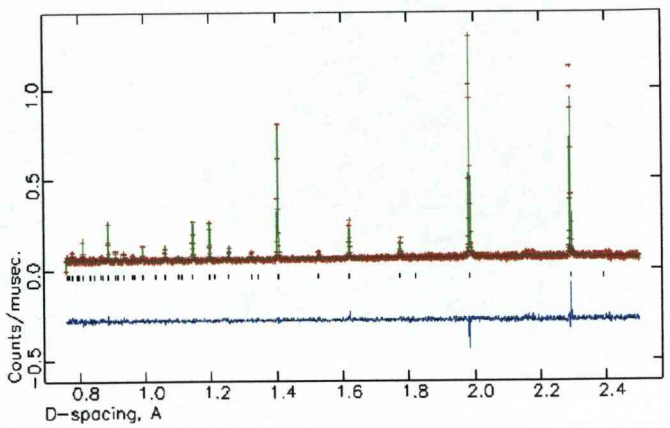

b

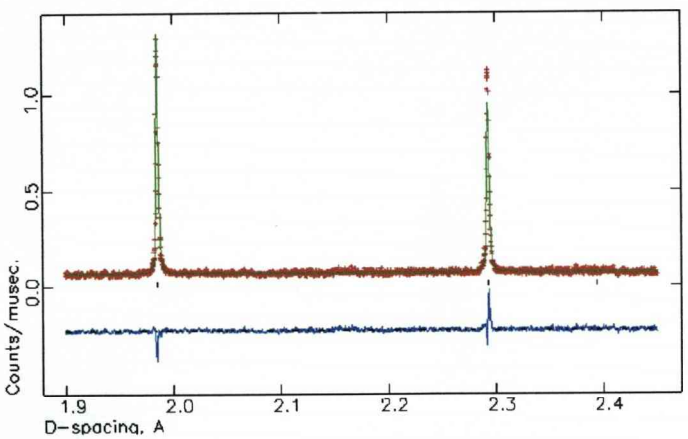

Figure 4. *(a) Rietveld refinement of the backscattering bank neutron diffraction data from HRPD of sample II of* $Sr_2MgMoO_{6-\delta}$ *at 500 °C. Crosses are observed data, the solid red line is the calculated pattern and the pink line is the difference. The set of tick marks correspond to the positions of the Bragg peaks for the* $Fm\bar{3}m$ *phase (b) Zoom of the refinement at high d-spacing showing a single peak at ~1.98 Å and showing that the peak at ~2.38 Å has disappeared.*

a

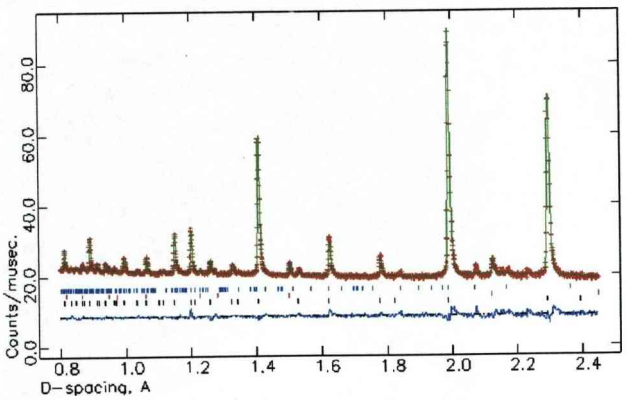

b

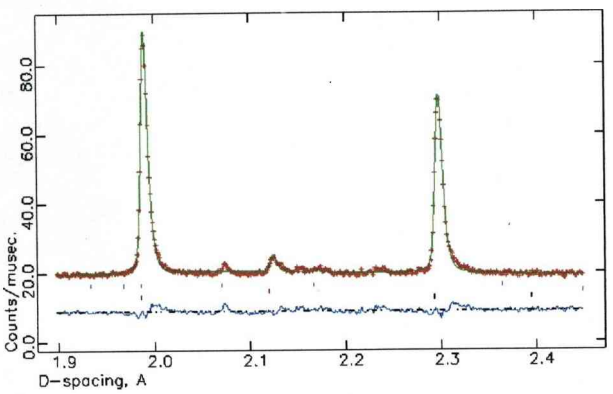

Figure 5. *(a) Rietveld refinement of the backscattering bank neutron diffraction data from Polaris of sample III of* $Sr_2MgMoO_{6-\delta}$ *at 600* ^{o}C*. Crosses are observed data, the solid red line is the calculated pattern and the pink line is the difference. The tick marks show the Bragg peaks for, from top to bottom, the n=2 Ruddlesden-Popper phase, MgO and the cubic phase of* $Sr_2MgMoO_{6-\delta}$ *(b) Zoom of the refinement at high d-spacing showing a single peak at ~1.98 Å and showing that the peak at ~2.38 Å has disappeared.*

Table 10. *Refined parameters and refined cell constant for sample III of* $Sr_2MgMoO_{6-\delta}$ *at temperatures above the transition:*

	500 °C (Polaris)	600 °C (Polaris)	700 °C (Polaris)	800 °C (Polaris)
wRp (%)	1.04	1.03	1.03	1.02
Rp (%)	1.62	1.61	1.59	1.58
χ^2	2.447	2.395	2.402	2.351
a (Å)	7.940833 (56)	7.951100 (66)	7.962535 (65)	7.972266 (69)
V (Å^3)	500.724 (11)	502.668 (12)	504.840 (12)	506.694 (13)

Table 11. *Refined atomic parameters for the* $Sr_2MgMoO_{6-\delta}$ *sample III (fixed parameters are in italic) at temperatures above the transition.*

	500 °C (Polaris)	600 °C (Polaris)	700 °C (Polaris)	800 °C (Polaris)
Sr1				
U	0.0213 (4)	0.0219 (5)	0.0229 (5)	0.0254 (3)
Mg1				
U	0.0119 (4)	0.0114 (4)	0.0107 (4)	0.0111 (2)
Mo1				
U	0.0119 (4)	0.0114 (4)	0.0107 (4)	0.0111 (2)
O1				
x	0.2577 (4)	0.2583 (4)	0.2582 (5)	0.2573 (4)
U	0.0274 (4)	0.0285 (5)	0.0288 (4)	0.0317 (2)
F	*0.91*	*0.91*	*0.91*	*0.91*

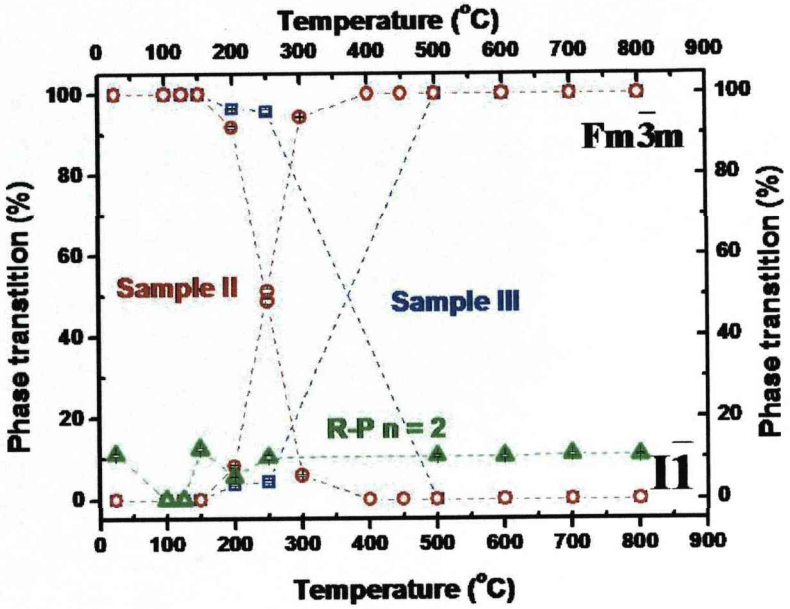

Figure 6. *Representation of the Phase Fraction against Temperature for* $I\bar{1}$ *and* $Fm\bar{3}m$ *phases in both sample II (red points) and sample III (blue points) of* $Sr_2MgMoO_{6-\delta}$ *and for the R-P n=2* $Sr_3(Mg_xMo_{1-x})_2O_{7-\delta}$ (green symbols) *present in sample III showing the transition between 175 °C and 350 °C.*

4.4. Discussion.

The perovskite phase in sample II and sample III of $Sr_2MgMoO_{6-\delta}$ were successfully refined at high temperature in the cubic $Fm\bar{3}m$ space

group. At intermediate temperatures alternative space groups were tried in order to find a suitable structural description. Several potential intermediate space groups are possible according to Kennedy et al[7,8]. Given these possible intermediate phases a number of different models were tried for the mixed temperature regime. Initially refinement in the monoclinic group $P2_1/n$ was tried but the final refinement obtained was not satisfactory. Refinement in the alternative monoclinic group I2/m and in the tetragonal space group I4/m were also unsatisfactory with refinement values of χ^2 = 17.91 and χ^2 = 9.19 respectively. Finally refinement with both cubic $Fm\bar{3}m$ space group phase and triclinic $I\bar{1}$ space group phase present gave a superior agreement than all the case tried before. In this refinement a value of χ^2 = 1.342 was reached for sample II at 350 °C.

As discussed in the previous chapter Sr_2MgMoO_6 adopts the tilt system $a^0a^0c^-$, with octahedral distortions reducing the tetragonal tilt-based symmetry to triclinic. It could be thought that the phase transition passes by an intermediate phase which would be the tetragonal I4/m. Refinements in an I4/m space group have been tried at temperatures in the transition but no satisfactory fit were obtained (χ^2 = 9.19).

It has been reported that the analogous compounds $SrMWO_6$ (M = Ni,Zn,Co)[5,6,12] have a second order phase transition from the tetragonal I4/m space group to the cubic $Fm\bar{3}m$ space group. However, in the case of $SrMWO_6$ (M = Cu)[3], a transition from the tetragonal I4/m space group to I4/mmm space group was reported. All these transitions are second

order and are consistent with the pseudo symmetry concept. On the other hand, the reported monoclinic $P2_1/n$ to the tetragonal I4/m transitions for the compounds Sr_2MWO_6 (M=Zn, Co) and a transition from the tetragonal I4/mmm space group to the cubic $Fm\bar{3}m$ space group for Sr_2MWO_6 (M = Cu) are reported to be first order transitions.

In the case of Sr_2NiMoO_6[6], the transition from the tetragonal I4/m space group to the cubic $Fm\bar{3}m$ space group was also second order. Associated with a continuous change in the rotation of the NiO_6 and MoO_6 octahedra, bond valence calculations indicate that the driving force for the phase transition is the bonding demands in the Sr A-sites cation, which adopt a distorted SrO_{12} coordination in the tetragonal structure. It has also been reported that the environment of the polarisable d^0 Mo (VI) also becomes more distorted in the tetragonal structure.

Both double perovskites Sr_2FeMoO_6 and Sr_2CoMoO_6 undergo a similar structural transition from the cubic $Fm\bar{3}m$ space group to the tetragonal I4/m space group.

The data presented above show that $Sr_2MgMoO_{6-\delta}$ does not present a continuous phase transition as might be expected by analogy with other Sr_2MMoO_6 perovskites. Figure 7 shows the cell volume versus temperature for both $I\bar{1}$ triclinic and $Fm\bar{3}m$ cubic phases. It can be seen that the different volumes do not converge as it would be expected for a continuous phase transition. In the same manner, Figure 8 shows the *a* parameter for the $Fm\bar{3}m$ cubic phase and the *c* parameter, $\sqrt{2}$ x *a* parameter and $\sqrt{2}$ x *b*

parameter for the $I\bar{1}$ triclinic phase versus temperature. Around the transition the values for the triclinic lattice parameter would be expected to converge with those of the cubic cell in the case of the continuous phase transition.

Table 12 to 14 show the refined bond lengths and calculated bond valence parameters for sample II of $Sr_2MgMoO_{6-\delta}$ at temperatures below the transition, at temperatures in low phase region and at temperatures above the transition for both triclinic $I\bar{1}$ and cubic $Fm\bar{3}m$ structures. It can be seen that the Mo-O distances decrease sharply above the transition for both samples II and III. This apparent reduction in bond length may be due to dynamic displacements in the high temperature phase.

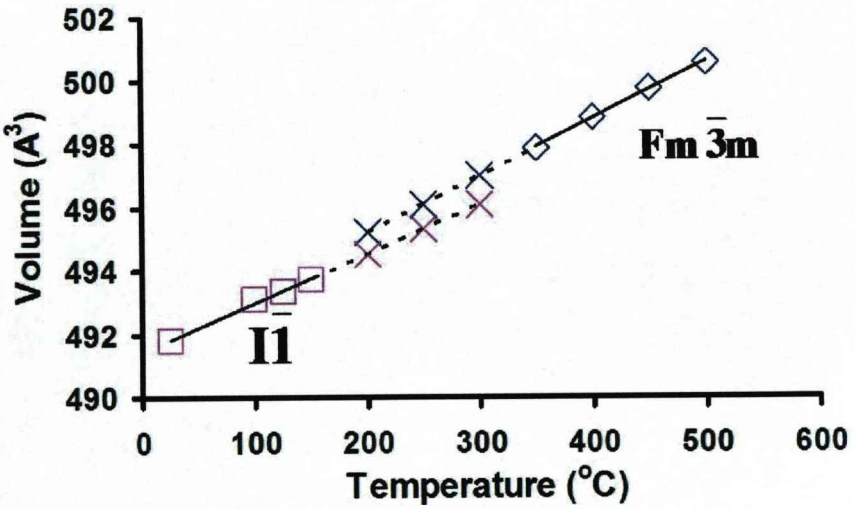

Figure 7. *Representation of the double volume for the $I\bar{1}$ phase and the volume of the cubic phase $Fm\bar{3}m$ against temperature in the region of the phase transition. The crosses show the points calculated by extrapolation of the trend in the volume for the cubic phase and the triclinic phase respectively. The differences in the slope for both volumes trend can be seen.*

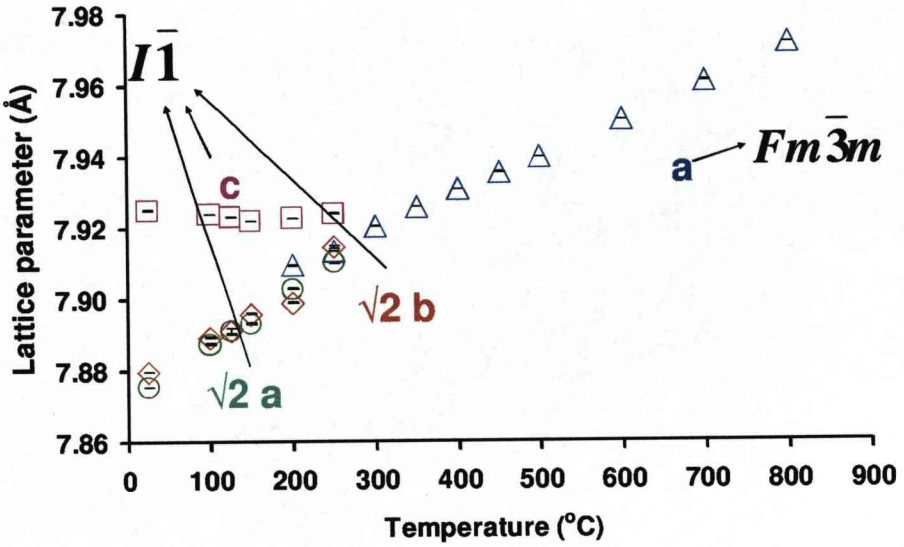

Figure 8. *Representation of the lattice parameters against temperature for sample II of* $Sr_2MgMoO_{6-\delta}$ *for both triclinic* $I\bar{1}$ *space group and cubic* $Fm\bar{3}m$ *space group phases. The graph shows both phases lattice parameter do not converge at the transition temperature.*

Table 12. *Refined bond lengths and calculated bond valence sums in the triclinic* $I\bar{1}$ *phase of II of* $Sr_2MgMoO_{6-\delta}$ *(refined oxygen deficiency is given in the final row) at temperatures below the transition. The fixed parameters are in italic.*

Bond	RT (HRPD)	100 °C (HRPD)	150 °C (HRPD)
Mo1-O1 x2/ Å	1.9602(28)	1.966 (11)	1.95645 (1)
Mo1-O2 x2 / Å	1.9475 (10)	1.975 (4)	1.94036 (3)
Mo1-O2b x2 / Å	1.9424 (9)	1.955 (4)	1.93546 (3)
Mg2-O1 x2 / Å	2.0059 (28)	2.001 (11)	2.00910 (1)
Mg2-O2 x2 / Å	2.0062 (10)	1.984 (4)	2.01494 (3)
Mg2-O2b x2 / Å	2.0260 (8)	2.008 (4)	2.03859 (3)
Mo BVS	5.34 (4)	5.13 (2)	5.43 (3)
Mg BVS	2.53 (2)	2.63 (2)	2.47 (5)
Sr BVS	2.05 (2)	2.01(9)	2.00 (7)
$\Sigma(r-r_{mean})^2$ Mo-O	1.87E-04	2.01E-04	2.22E-04
$\Sigma(r-r_{mean})^2$ Mg-O	3.92E-04	3.05E-04	4.88E-04
δ	0.014 (2)	0.001 (7)	*0.014*

Table 13. *Refined bond lengths and calculated bond valence sums in the both triclinic $I\bar{1}$ phase (a) and cubic $Fm\bar{3}m$ phase (b) of sample II of $Sr_2MgMoO_{6-\delta}$ (refined oxygen deficiency is given in the final row) at temperatures in the two phase region.*

a

Bond	200 °C Triclinic phase (HRPD)	250 °C Triclinic phase (HRPD)
Mo1-O1 x2/ Å	1.95541 (2)	1.981 (34)
Mo1-O2 x2 / Å	1.97760 (4)	1.994 (8)
Mo1-O2b x2 / Å	1.97615 (4)	1.976 (8)
Mg2-O1 x2 / Å	2.01104 (2)	1.993 (34)
Mg2-O2 x2 / Å	1.97941 (4)	1.971 (8)
Mg2-O2b x2 / Å	1.99521 (4)	2.003 (8)
Mo BVS	5.07 (1)	4.88 (5)
Mg BVS	2.65 (1)	2.70 (5)
Sr BVS	1.98 (1)	2.00 (11)
$\Sigma(r-r_{mean})^2$ Mo-O	3.08E-04	1.73E-04
$\Sigma(r-r_{mean})^2$ Mg-O	4.90E-04	5.36E-04
δ	0.010 (11)	*0.014*

b

Bond	200 °C Cubic phase (HRPD)	250 °C Cubic phase (HRPD)	300 °C Cubic phase (HRPD)
Mo-O x 6 / Å	1.88738 (4)	1.90549 (2)	1.90669 (1)
Mg-O x 6 / Å	2.06729 (4)	2.05124 (2)	2.05355 (1)
Mo BVS	6.32 (1)	6.02 (1)	6.00 (1)
Mg BVS	2.18 (1)	2.28 (1)	2.26 (1)
Sr BVS	1.91 (1)	1.89 (1)	1.89 (1)
δ	0.010 (33)	0.030 (4)	*0.05*

Table 14. *Refined bond lengths and calculated bond valence sums in the cubic* $Fm\bar{3}m$ *phase of sample II of* $Sr_2MgMoO_{6-\delta}$ *(refined oxygen deficiency is given in the final row) at temperatures above the transition.*

Bond	350 °C (HRPD)	400 °C (HRPD)	450 °C (HRPD)	500 °C (HRPD)	600 °C (HRPD)	700 °C (HRPD)	800 °C (HRPD)
Mo-O x 6 / Å	1.9031 (17)	1.9049 (18)	1.909 (5)	1.9112 (22)	1.9143 (22)	1.9171 (26)	1.9160 (27)
Mg-O x 6 / Å	2.0597 (17)	2.0604 (18)	2.059 (5)	2.0587 (22)	2.0607 (23)	2.0634 (26)	2.0697 (27)
Mo BVS	6.06 (1)	6.03 (1)	5.97 (1)	5.93 (1)	5.88 (1)	5.84 (1)	5.86 (1)
Mg BVS	2.22 (1)	2.22 (1)	2.23 (1)	2.23 (1)	2.22 (1)	2.20 (1)	2.17 (1)
Sr BVS	1.88 (1)	1.87 (1)	1.86 (1)	1.86 (1)	1.84 (1)	1.82 (1)	1.80 (1)
δ	*0.05*	*0.05*	*0.05*	0.046 (10)	0.038 (11)	0.056 (12)	0.062 (12)

Two possible explanations can be put forward to explain the observed behaviour. Firstly, this transition is first order where hysteresis is expected. In the case of Sr_2CuWO_6, a first order transition from the tetragonal I4/mmm structure to the cubic $Fm\bar{3}m$ structure was reported. No intermediate phases have been identified in the case of $Sr_2MgMoO_{6-\delta}$. In order to confirm this, refinements in several models I2/m, I4/m or I4mmm were tried without satisfactory result.

Secondly, the hysteresis in transition can be explained for the presence of strains due to anti-phase boundaries[13,14]. We have postulated that $Sr_2MgMoO_{6-\delta}$ has a high density of anti-phase boundaries in order to accommodate the presence of oxygen vacancies. These anti-phase boundaries could cause hysteresis and lead to an apparently first order transition due to the change produced by the anti-phase boundary.

Here the total thermal expansion coefficients were calculated using the relation,

$$\alpha_p^{Tot} = \frac{(p - p_o)}{p_o \Delta T}\Big|_{pO_2=cte} \qquad (1)$$

where p stands for the lattice parameters a, b and c and the unit cell volume V, p_o represents the values of the lattice parameters and the unit cell volume V at the reference state, and $\Delta T = T - T_o$ stands for the temperature range. The reference state was chosen to be T_o = 25 °C. The total expansion includes the thermal expansion, defined at constant oxygen content, and the chemical expansion, defined at constant temperature[15]. In the previous study

done by Huang et al.[16] the thermal expansion coefficient was determined by dilatometry measurements. The total expansion coefficient values calculated from Equation (1) are $\alpha_a = 19.46 \cdot 10^{-6}\ K^{-1}$, $\alpha_b = 15.98 \cdot 10^{-6}\ K^{-1}$, $\alpha_c = -26.99 \cdot 10^{-6}\ K^{-1}$ and $\alpha_v = 32.83 \cdot 10^{-6}\ K^{-1}$ for the temperatures below the transition and $\alpha_a = 17.38 \cdot 10^{-6}\ K^{-1}$, $\alpha_b = 16.29 \cdot 10^{-6}\ K^{-1}$, $\alpha_c = 4.08 \cdot 10^{-6}\ K^{-1}$ and $\alpha_v = 37.80 \cdot 10^{-6}\ K^{-1}$. The average of the coefficients for the three lattice parameters a, b and c or $\alpha_v/3$ can be compared with the values obtained by dilatometry measurements by Huang et al. The values obtained are very close to the dilatometry values: $\alpha_{mean} = 10.93 \cdot 10^{-6}\ K^{-1}$ vs. $\alpha_{Huang} = 11.70 \cdot 10^{-6}\ K^{-1}$ at low temperature and $\alpha_{mean} = 12.67 \cdot 10^{-6}\ K^{-1}$ vs. $\alpha_{Huang} = 12.70 \cdot 10^{-6}\ K^{-1}$ at high temperature. These values are also typical values of values for good solid oxide fuel cells components reported in the literature, for instance YSZ $\alpha = 10.00 \cdot 10^{-6} K^{-1}$.

4.5. Conclusion.

It has been shown that the double perovskite $Sr_2MgMoO_{6-\delta}$ transforms at high temperature from a triclinic $I\bar{1}$ structure to a cubic $Fm\bar{3}m$ structure. This phase transition is observed over a range of temperature between 200 °C and 300 °C with both phase coexisting in this range.

By analogy with known Sr_2MMoO_6 systems a continuous second-order phase transition might be expected. However, it was shown that the double perovskite $Sr_2MgMoO_{6-\delta}$ does not present a continuous phase transition but the data shows an apparently first order transition from the triclinic $I\bar{1}$ space group to the cubic $Fm\bar{3}m$ space group.

Thermal expansion coefficient values were obtained from the data at the different temperatures that are very close to the values reported in the literature obtained from dilatometry measurements.

4.6. References

(1) Bernuy-Lopez, C.; Allix, M.; Bridges, C. A.; Claridge, J. B.; Rosseinsky, M. J. *Chem. Mater.* **2007**, *19*, 1035-1043.

(2) Zhou, Q.; Kennedy, B. J.; Elcombe, M. M. *Physica B.* **2006**, *385-386 I*, 190-192.

(3) Gateshki, M.; Igartua, J. M. *J. Phys-Condens. Mat.* **2003**, *15*, 6749-6757.

(4) Chmaissem, O.; Kruk, R.; Dabrowski, B.; Brown, D. E.; Xiong, X.; Kolesnik, S.; Jorgensen, J. D.; Kimball, C. W. *Phys. Rev. B* **2000**, *62*, 14197-14206.

(5) Ivanov, S. A.; Eriksson, S. G.; Tellgren, R.; Rundlo?f, H.; Tseggai, M. *Mater. Res.Bull.* **2005**, *40*, 840-849.

(6) Eriksson, A. K.; Eriksson, S. G.; Ivanov, S. A.; Knee, C. S.; Eriksen, J.; Rundlo?f, H.; Tseggai, M. *Mater. Res. Bull.* **2006**, *41*, 144-157.

(7) Howard, C. J.; Kennedy, B. J.; Woodward, P. M. *Acta Crystallogr. B* **2003**, *59*, 463-471.

(8) Howard, C. J.; Stokes, H. T. *Acta Crystallogr.B* **1998**, *54*, 782-789.

(9) Landau L., D. *Stat Physics* **1980**, *CH14.*

(10) Hull, S.; Smith, R. I.; David, W. I. F.; Hannon, A. C.; Mayers, J.; Cywinski, R. *Physica B.* **2007**, 1000-1002.

(11) Ibberson, R. M.; David, W. I. F.; Knight, K. S. *The High Resolution Neutron Powder Diffractometer (HRPD) at ISIS - A user guide* **1992**, Report RAL-92-031.

(12) Gagulin, V. V.; Korchagina, S. K.; Ivanova, V. V.; Shevchuk, Y. A. *Inorg. Mater.* **2003**, *39*, 625-626.

(13) Cheng, S. Y.; Ho, N. J.; Lu, H. Y. *J. Amer. Cer. Soc.* **2006**, *89*, 3498-3506.

(14) Ding, Y.; Liang, D. D. *J. Appl. Phys.* **2002**, *92*, 5425-5428.

(15) Prado, F.; Manthiram, A. *J. Solid State Chem.* **2001**, *158*, 307-314.

(16) Huang, Y. H.; Dass, R. I.; Denyszyn, J. C.; Goodenough, J. B. *J. Electrochem. Soc.* **2006**, *153*, A1266-A1272.

Chapter 5:

Crystal structure and microstructural features of $Sr_3Mg_{0.5}Mo_{1.5}O_{7-\delta}$.

5.1. Introduction.

Ruddlesden-Popper (R-P) type structures of general formula $A_{n+1}B_nO_{3n+1}$ (A = lanthanoid, rare earth; B = transition metal)[1,2] have been the subject of numerous studies. They are structures consisting of alternating perovskite blocks *n* layers thick and a rock salt-type layer. This diverse family exhibits complex magnetic and electronic properties as a function of composition[3,4]. They support a large range of non stoichiometry[5-7] compounds and have been widely studied, because of their diverse photocatalytic activity, ionic conductivity, magnetic, dielectric, luminescence, and intercalation properties[8-11].

In chapter 3[12], the double perovskite $Sr_2MgMoO_{6-\delta}$ has been found to adopt a $\sqrt{2}\ a_p$ x $\sqrt{2}\ a_p$ x $2\ a_p$ superstructure of the simple perovskite cell,

derived from an $a^0a^0c^-$ tilt system via distortion of the Mg- and Mo centred octahedra. Reduction of Sr_2MgMoO_6 appears to be correlated with antisite disorder at either point or extended anti-phase defects. Upon further reduction above 900 °C, Sr_2MgMoO_6 begins to decompose into a reduced material related to an n = 2 Ruddlesden-Popper (R-P) structure with a significantly higher Mo:Mg ratio and MgO is detected as a secondary phase.

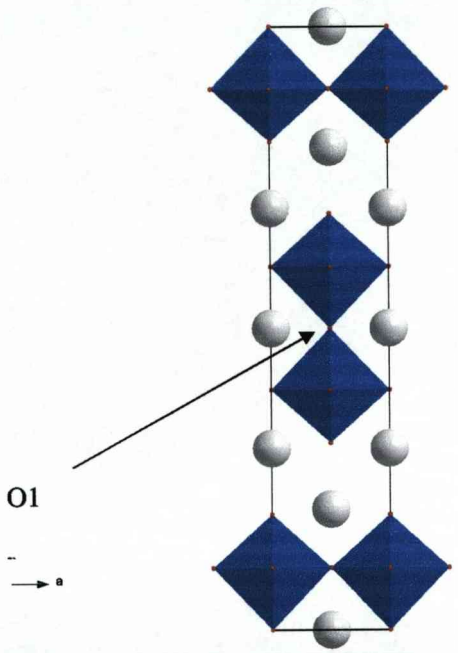

Figure 1. *Refined structure of the n = 2 Ruddlesden-Popper phase* $Sr_3(Mo_{1-x}Mg_x)_2O_{7-\delta}$ *(x = 0.215(9), δ = 0.49(3)) (sample III chapter 3) viewed along [010]. O1 is labeled to show the location of the oxygen vacancies.*

Preliminary TEM studies combining electron diffraction patterns with EDS analysis have confirmed the R-P type structures of the reduced

material with a Mg/Mo ratio close to 3. Based on these initial investigations attempts were made to synthesis pure phases based on the refined composition of the intergrowth in sample III chapter 3 ($Sr_3Mg_{0.5}Mo_{1.5}O_{7-\delta}$ Figure 1).

This chapter deals with the investigation in the Sr-Mg-Mo-O system at compositions close to those of from the generic formula $Sr_{n+1}(Mg,Mo)_nO_{3n+1}$.

5.2. Experimental.

The best result were achieved by direct reaction of SrO, MgO, MoO_3 and Mo as starting materials and by using sealed silica tubes in order to control the oxygen stoichiometry. The starting materials were handled in a dry box due to the utilisation of SrO and its instability in air. Molybdenum metal and MoO_3 are used in order to control the oxygen stoichiometry. The precursor materials are weighed and mixed in the dry box, pressed into pellets and introduced in silica tubes. These tubes were evacuated at vacuum of 10^{-5} torr and sealed.

Other experimental information can be found in chapter 2.

5.3. Results and discussion.

Table 1 shows a summary of all the different synthetic methods and samples protection used in the attempt of the synthesis of this R-P n = 2 phase.

Table 1. *Different methods and sample protection tried in the attempt of the synthesis of the R-P n = 2 phase. The best results are shown in yellow.*

Methods used	Sample protection
Normal solid state reaction in different atmospheres	Alumina crucible
Sol-gel route	**Pt tubes and foil**
"Mg/MgO" route	
$Sr_{1-x}Mg_xO$ as precursor	
Sealed tubes	

Other synthetic methods were tried such as the well-known sol-gel route, a named-"Mg/MgO" route equivalent to the one used by Steiner et al in the synthesis of $Sr_3Mo_{1.5}Zn_{0.5}O_{7-\delta}$[13] or the utilisation of a "$Sr_{1-x}Mg_xO$" oxide as precursor in order to improve the reactivity of the magnesium. The atmospheres used during these different methods were air, 5 % H_2/N_2 and H_2. None of these methods gave satisfactory results. X-Ray powder diffraction data showed the formation of the double perovskite $Sr_2MgMoO_{6-\delta}$ as main phase (Figure 2).

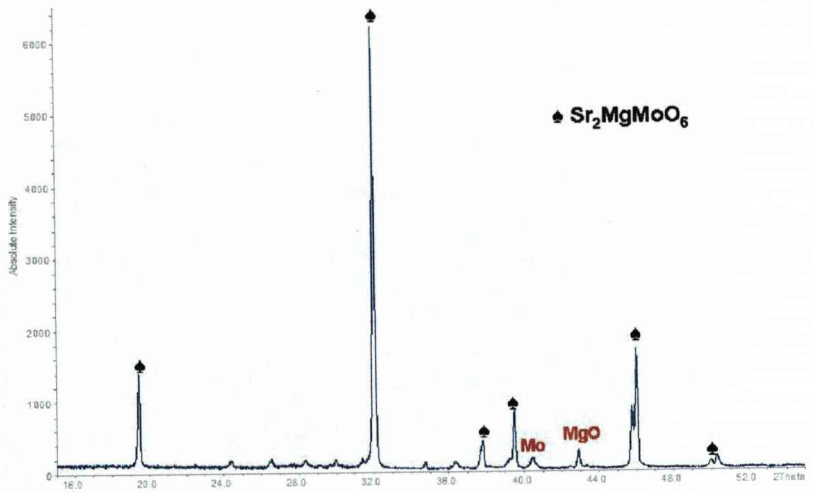

Figure 2. *Powder X-Ray diffraction pattern for* $Sr_3(Mo_{1-x}Mg_x)_2O_{7-\delta}$ *synthesised under 5 %* H_2/N_2.

Only reactions in sealed quartz tubes, in order to control the oxygen stoichiometry, were found to form significant quantities of the R-P 2. At this point, a systematic study was performed of different oxygen stoichiometries and Mg: Mo ratios in order to find the optimal composition. It was also observed that the quality of the product was improved when the sample was place inside a platinum tube instead of an alumina crucible within the sealed silica ampoule. Once the reaction was finished the tubes were opened inside the glove box and were checked by X-Ray powder diffraction using an air sensitive X-Ray sample holder.

Table 2 lists the different nominal chemical composition which were tried in order to isolate the R-P n = 2 phase pure.

Table 2. *Different nominal composition attempted for the synthesis of the Ruddlesden-Popper n = 2 phase. Mo oxidation state is marked for each compound. The best sample is highlighted in yellow.*

Composition tested Mg/Mo 1:1	Composition tested Mg/Mo 1:2	Composition tested Mg/Mo 1:3
$Sr_3MgMo^{5+}O_{6.5}$	$Sr_3Mg_{2/3}Mo_{4/3}{}^{4.27+}O_{6.5}$	$Sr_3Mg_{0.5}Mo_{1.5}{}^{3.33+}O_6$
$Sr_3MgMo^{4+}O_6$	$Sr_3Mg_{2/3}Mo_{4/3}{}^{3.52+}O_6$	$Sr_3Mg_{0.5}Mo_{1.5}{}^{4+}O_{6.5}$
		$Sr_3Mg_{0.5}Mo_{1.5}{}^{4.13+}O_{6.6}$
		$Sr_3Mg_{0.5}Mo_{1.5}{}^{4.4+}O_{6.8}$
		$Sr_3Mg_{0.5}Mo_{1.5}{}^{4.67+}O_7$

Figure 3 shows X-Ray diffraction data for three different samples as a function of the Mg: Mo ratio. Though not phase pure it can be seen that the impurities peaks are minimised for $Sr_3Mg_{0.5}Mo_{1.5}O_{7-\delta}$ where the R-P n=2 phase $Sr_3(Mg_xMo_{1-x})_2O_{7-\delta}$ is clearly the main phase and $Sr_2MgMoO_{6-\delta}$ and $Sr_{11}Mo_4O_{23}$ are impurity phases. In the other cases, "$Sr_3MgMoO_{7-\delta}$" and "$Sr_3Mg_{2/3}Mo_{4/3}O_{7-\delta}$", the double perovskite $Sr_2MgMoO_{6-\delta}$ is the main phase and the R-P n = 2 only a minor phase.

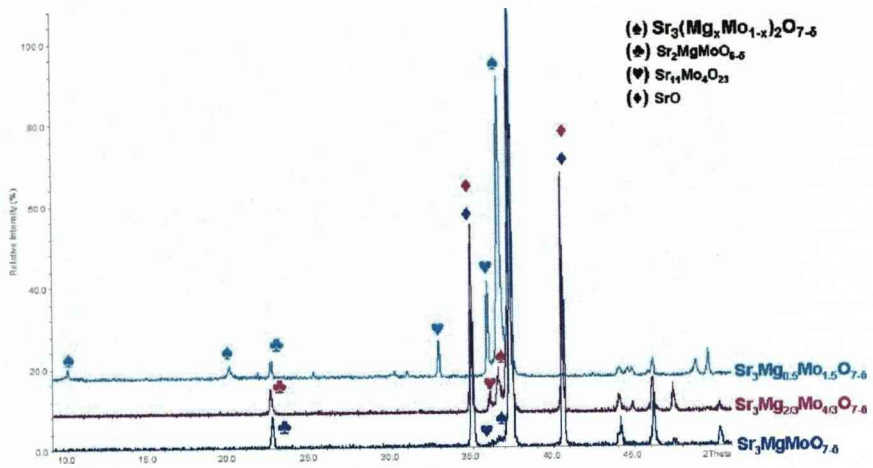

Figure 3. *X-Ray powder diffraction patterns from different nominal compositions tried in function of the Mg:Mo ratio,* $Sr_3MgMoO_{7-\delta}$, $Sr_3Mg_{2/3}Mo_{4/3}O_{7-\delta}$ *and* $Sr_3Mg_{0.5}Mo_{1.5}O_{7-\delta}$.

At this point, the presence of the impurity named $Sr_{11}Mo_4O_{23}$ should be noted, this phase will be discussed further in chapter 6. This phase was preliminarily identified as Sr_3MoO_6, based on reported diffraction profiles.

Once the optimum Mg: Mo ratio had been determined, a systematic study was performed in order to determine the correct oxygen stoichiometry. Table 2 lists the different nominal oxygen stoichiometries tested. The best result was found for $Sr_3Mg_{0.5}Mo_{1.5}O_{6.8}$. In the same manner, different time and temperature treatments were explored in an attempt to isolate the phase in a pure form. Table 3 summarizes conditions tried. The best result was obtained firing a sample of nominal composition $Sr_3Mg_{0.5}Mo_{1.5}O_{6.8}$ at 900 °C for 12 h., then at 1100 °C for 24 h. and finally at 1200 °C for 24 h in a single heat treatment.

Figure 4 shows X-Ray diffraction data for three different samples in function of the nominal oxygen stoichiometry. It can be seen how the samples with nominal composition $Sr_3Mg_{0.5}Mo_{1.5}O_{6.8}$ gives the best result. However, the double perovskite $Sr_2MgMoO_{6-\delta}$ and the pseudo-perovskite $Sr_{11}Mo_4O_{23}$ phase as impurity phases are always present.

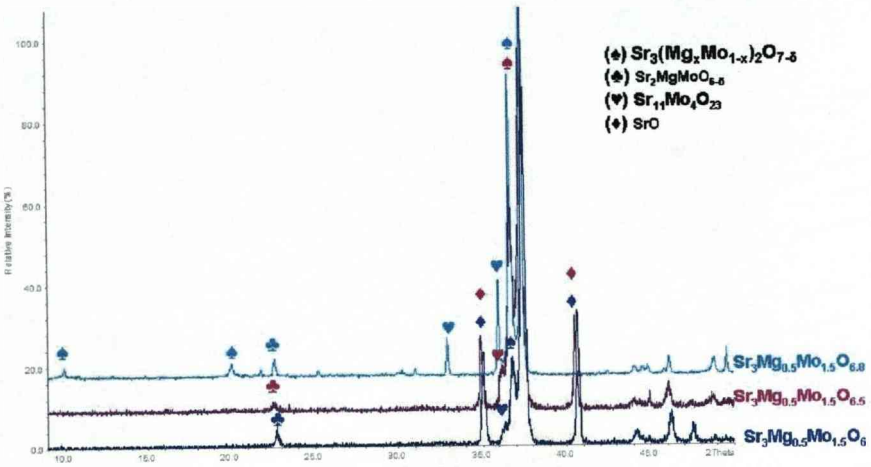

Figure 4. *X-Ray powder diffraction patterns from different nominal compositions tried in function of the oxygen stoichiometry,* $Sr_3Mg_{0.5}Mo_{1.5}O_6$, $Sr_3Mg_{0.5}Mo_{1.5}O_{6.5}$ *and* $Sr_3Mg_{0.5}Mo_{1.5}O_{6.8}$ *, in the attempt of the synthesis of the Ruddlesden-Popper n = 2 phase. They are marked the phases identified in each X-Ray powder diffraction pattern.*

Table 3. *Temperature programmes attempted for the synthesis of the R-P n = 2 phase. The purest sample is highlighted in yellow.*

Times and temperatures tried for $Sr_3Mg_{0.5}Mo_{1.5}O_{6.8}$		Main phase obtained	Refiring	Main phase obtained
900 C 12h		$Sr_2MgMoO_{6-\delta}$	1250C --> 24h	$Sr_2MgMoO_{6-\delta}$
900 C 36 h		$Sr_2MgMoO_{6-\delta}$	1275 C--> 24h	$Sr_2MgMoO_{6-\delta}$
1200 C 36 h		$Sr_2MgMoO_{6-\delta}$		
1200 C 24h		$Sr_2MgMoO_{6-\delta}$		
900C 12h --> 1200C 24h		$Sr_2MgMoO_{6-\delta}$ + $Sr_3Mg_{0.5}Mo_{1.5}O_{6.8}$	1200C --> 24 h	
900C 36h --> 1200C 24h		$Sr_2MgMoO_{6-\delta}$ + $Sr_3Mg_{0.5}Mo_{1.5}O_{6.8}$		
900C 12h --> 1100C 24h		$Sr_2MgMoO_{6-\delta}$ + $Sr_3Mg_{0.5}Mo_{1.5}O_{6.8}$		
900C 12h --> 1100C 48h		$Sr_2MgMoO_{6-\delta}$ + $Sr_3Mg_{0.5}Mo_{1.5}O_{6.8}$		
900C 36h --> 1100C 48h		$Sr_2MgMoO_{6-\delta}$ + $Sr_3Mg_{0.5}Mo_{1.5}O_{6.8}$		
900C 12h --> 1000C 24h	--> 1200C 24h	$Sr_3Mg_{0.5}Mo_{1.5}O_{6.8}$		
900C 12h --> 1100C 24h	**--> 1200C 24h**	**$Sr_3Mg_{0.5}Mo_{1.5}O_{6.8}$**	1200C --> 24 h	$Sr_3Mg_{0.5}Mo_{1.5}O_{6.8}$ + Mo + MgO
900C 12h --> 1100C 24h	--> 1200C 48h	$Sr_3Mg_{0.5}Mo_{1.5}O_{6.8}$		

The purest sample obtained for the composition $Sr_3Mg_{0.5}Mo_{1.5}O_{6.8}$ was further studied by TEM techniques. EDS analysis for this sample confirmed its poor homogeneity and lead to average chemical formula of $Sr_{2.68}Mg_{0.64}Mo_{1.67}$ considering a theoretical R-P n = 2 stacking mode. Reconstruction of the reciprocal space of $Sr_3Mg_{0.5}Mo_{1.5}O_{7-\delta}$ from electron diffraction patterns (Figure 5) revealed cell of dimensions of a_p x a_p x 20 Å and reflection condition of h+k+l=2n consistent with the tetragonal space group I4/mmm in good agreement with the lattice expected in the case of n = 2 members of R-P series (white arrows). However, it can also be seen from the electron diffraction study that extra spots or diffuse spots are often observed along c^*.

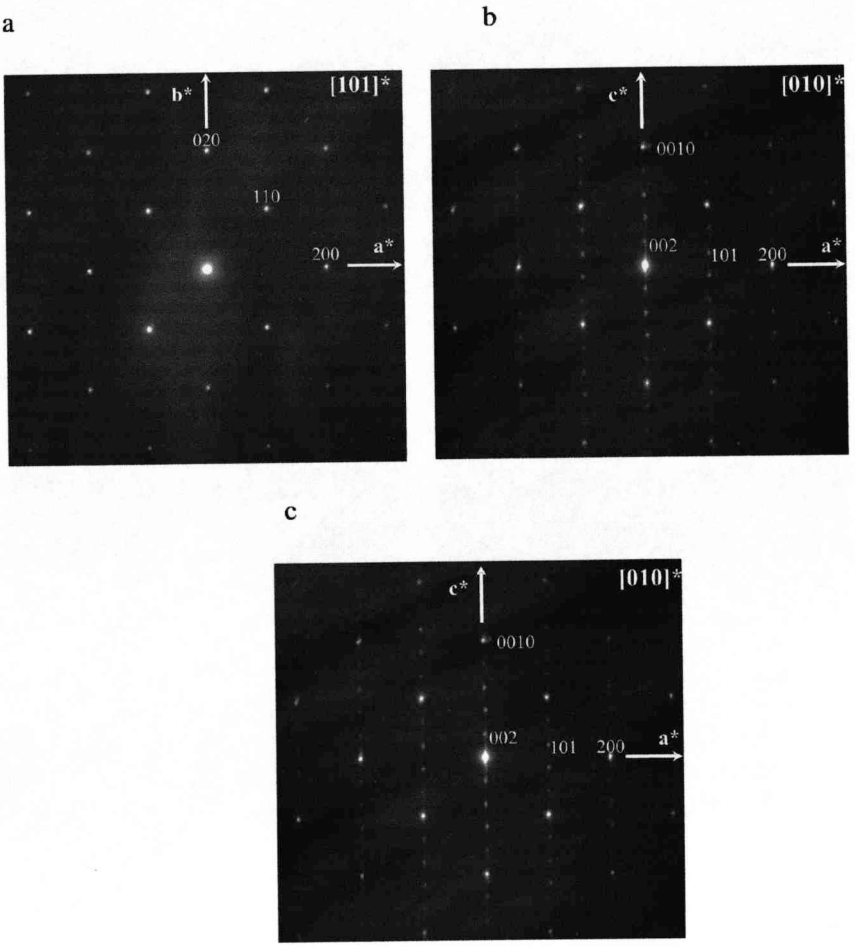

Figure 5. *Selected area electron diffractograms (ED) for* $Sr_3Mg_{0.5}Mo_{1.5}O_{7-\delta}$ *for the (a) [101], (b)* $[1\bar{1}0]$*, (c) [010] projections.*

Given the observations of extra spots a High Resolution Electron Microscopy study (HREM) was carried out on $Sr_3Mg_{0.5}Mo_{1.5}O_{6.8}$. This showed typical defects in the n = 2 R-P matrix. Figure 6 and Figure 7 show that these defects can be identified either as a Ruddlesden-Popper type

phase n=1 or as the double perovskite $Sr_2MgMoO_{6-\delta}$ intergrowth in the R-P n = 2 phase. Figure 8 shows an electron diffraction pattern of the Ruddlesden-Popper n=2 phase where spots from the double perovskite $Sr_2MgMoO_{6-\delta}$ are also apparent.

Thus it seems likely that the extra spots or diffuse scattering observed along the c^* can be interpreted as the superposition of diffraction spots belonging to different members of the R-P series in an R-P n = 2 matrix. In the case of $Sr_3Mg_{0.5}Mo_{1.5}O_{7-\delta}$ no ordering phenomena has been observed by HREM observations, contrary to the highly ordered phase $Sr_2MgMoO_{6-\delta}$ studied in chapter 3.

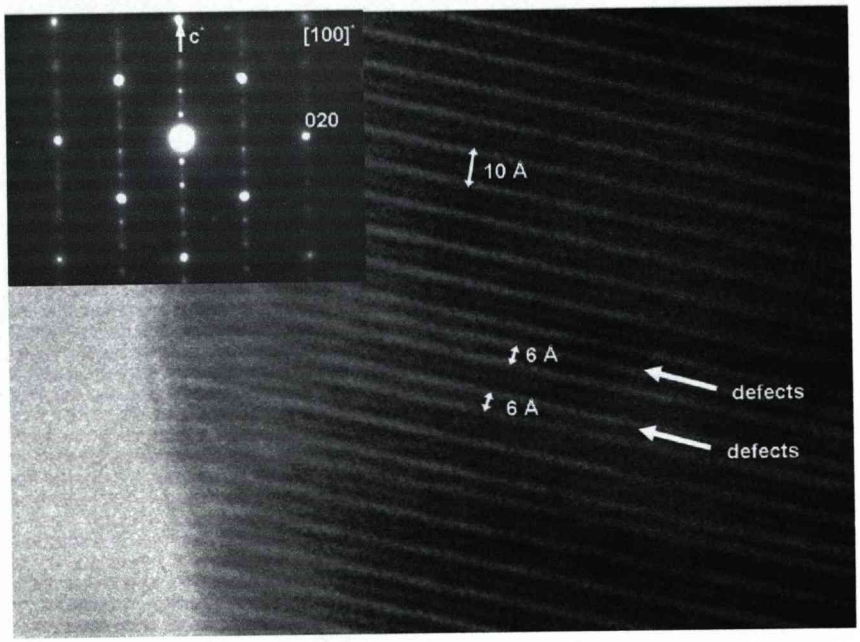

***Figure 6**. HREM image and ED pattern (insert) of $Sr_3Mg_{0.5}Mo_{1.5}O_{7-\delta}$ viewed in the [100] projection showing some defects which can be identified as R-P n=1 intergrowths.*

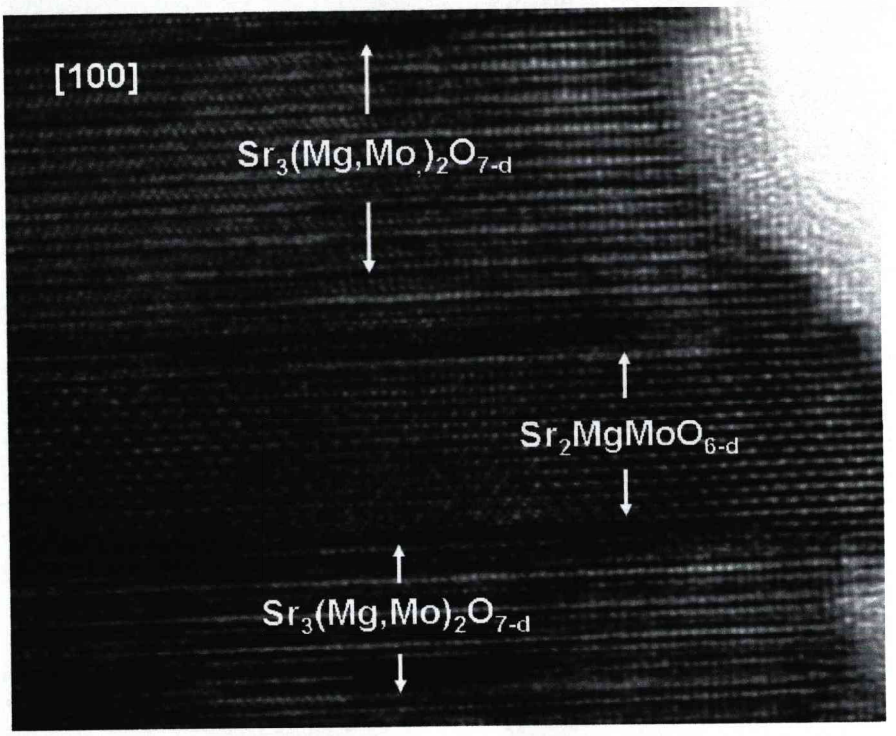

Figure 7. *HREM images of* $Sr_3Mg_{0.5}Mo_{1.5}O_{7-\delta}$ *viewed in the [100] projecting showing the double perovskite intergrowths in the R-P n=2 intergrowths.*

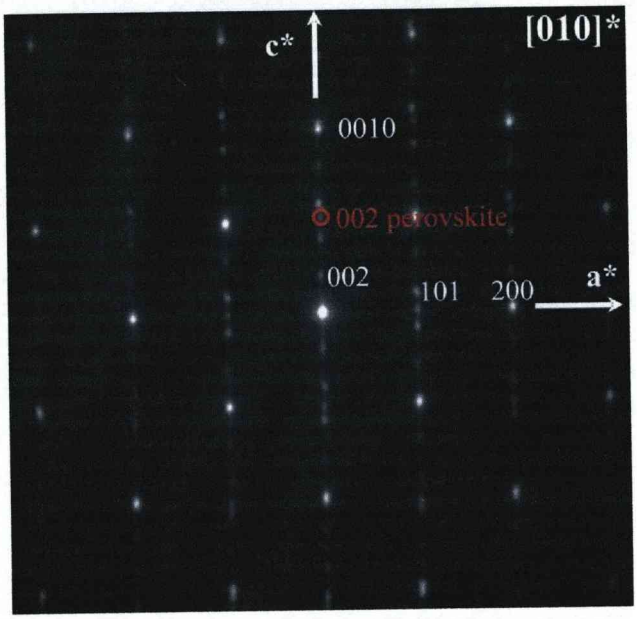

Figure 8. *ED pattern in the [010] projection of the* $Sr_3Mg_{0.5}Mo_{1.5}O_{7-\delta}$ *oxide where it is marked in red the* $Sr_2MgMoO_{6-\delta}$ *intergrowth.*

X-Ray powder diffraction refinements have been carried out on the best sample obtained for the Ruddlesden-Popper n = 2 phase $Sr_3Mg_{0.5}Mo_{1.5}O_{6.8}$. Figure 9 shows the powder XRD refinement in the tetragonal I4/mmm space group with a = 3.9477 (9) Å and c = 20.5544 (8) Å. The double perovskite $Sr_2MgMoO_{6-\delta}$ and the pseudo-perovskite $Sr_{11}Mo_4O_{23}$ were introduced as additional phases in the refinement in order to determine their weight fraction in the material. The double perovskite $Sr_2MgMoO_{6-\delta}$ was introduced with the cubic model in the $Fm\bar{3}m$ space group discussed in chapter 4. Other models such as a positionally fixed

triclinic model or a I2/m model were tried but the results were no better than those obtained using the cubic model. In the same manner, for the pseudo-perovskite $Sr_{11}Mo_4O_{23}$, the tetragonal model $I4_1/a$ (discussed in chapter 6) was used. The result obtained was 20.51 (21) wt% for the double perovskite $Sr_2MgMoO_{6-\delta}$ and 9.04 (15) wt% for the pseudo-perovskite $Sr_{11}Mo_4O_{23}$. Table 4 shows the cell parameters, cell volume, refinement parameters and phase fractions.

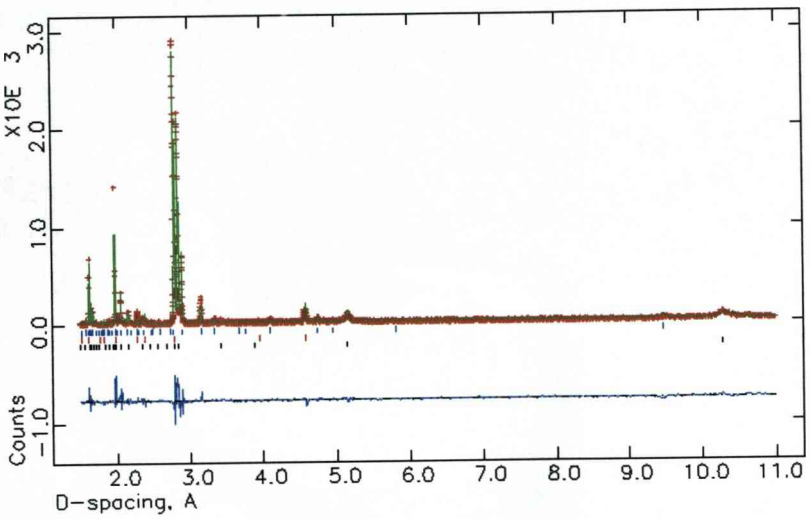

Figure 9. *X-Ray powder diffraction refinement plot for the Ruddlesden-Popper n = 2 $Sr_3Mg_{0.5}Mo_{1.5}O_{6.8}$. The tick marks show the Bragg peaks for, from top to bottom, the n = 2 R-P phase $Sr_3Mg_{0.5}Mo_{1.5}O_{7-\delta}$, the double perovskite $Sr_2MgMoO_{6-\delta}$ and the pseudo-perovskite $Sr_{11}Mo_4O_{23}$.*

Table 5 shows the refined atomic parameters and refined occupancy values for the $Sr_3Mg_{0.5}Mo_{1.5}O_{7-\delta}$. The refined occupancy appears to indicate

some deficiency on the strontium site as indicated by the EDS analysis. The refined strontium content is 2.67 (12). In the same manner, the occupancy value for the molybdenum and for the magnesium are 1.34 (12) and 0.66 (12) respectively. These values give a chemical formula for this phase of $Sr_{2.67}Mg_{0.66}Mo_{1.34}$. This chemical formula is more consistent with the average chemical formula observed by EDS: $Sr_{2.68}Mg_{0.64}Mo_{1.67}$. However the overall role of strontium vacancies and or substitution of other cations on the strontium site is still unclear. Given that syntheses carried out starting with $Sr_{2.75}Mg_{0.5}Mo_{1.5}O_{7-\delta}$ as the nominal composition and varying the oxygen stoichiometry yielded no improvement in the quality of the diffraction patterns was observed. All still yielded multiphase products comprising the double perovskite $Sr_2MgMoO_{6-\delta}$, the pseudo-perovskite $Sr_{11}Mo_4O_{23}$ and the n = 2 R-P phase $Sr_3Mg_{0.5}Mo_{1.5}O_{7-\delta}$ similar to those observed in the case of $Sr_3Mg_{0.5}Mo_{1.5}O_6$.

Table 4. *Refinement parameters, refined cell constants and phase fraction (quoted in weight %) for the* $Sr_3Mg_{0.5}Mo_{1.5}O_{7-\delta}$, $Sr_2MgMoO_{6-\delta}$ *and* $Sr_{11}Mo_4O_{23}$ *oxides present in the tetragonal I4/mmm space group.*

	$Sr_3Mg_{0.5}Mo_{1.5}O_{7-\delta}$	$Sr_2MgMoO_{6-\delta}$	$Sr_{11}Mo_4O_{23}$
χ^2	3.259		
R_{wp} (%)	23.24		
R_{exp} (%)	7.13		
a (Å)	3.9476 (1)	7.9144 (2)	11.5987 (12)
c (Å)	20.5546 (8)		16.3920 (33)
Phase fraction $Sr_3Mg_{0.5}Mo_{1.5}O_{7-\delta}$ (%)	71.11 (2.18)		
Phase fraction $Sr_2MgMoO_{6-\delta}$ (%)	19.28 (44)		
Phase fraction $Sr_{11}Mo_4O_{23}$ (%)	9.61 (16)		

Table 5. *Refined atomic parameters and refined occupancies for the* $Sr_3Mg_{0.5}Mo_{1.5}O_{7-\delta}$ *oxide in the tetragonal I4/mmm space group.*

atom	Site	x	y	z	Uiso (Å)	occupancy
Sr1	*2b*	0	0	0.5	0.035 (3)	0.88 (4)
Sr2	*4e*	0	0	0.3128 (3)	0.035 (3)	0.92 (4)
Mo1	*4e*	0	0	0.1010 (3)	*0.025*	0.70 (6)
Mg1	*4e*	0	0	0.1010 (3)	*0.025*	0.30 (6)
O1	*2a*	0	0	0	0.016 (20)	*0.9*
O2	*4e*	0	0	0.2182 (4)	0.020 (13)	*1*
O3	*8g*	0	0.5	0.0959 (9)	0.016 (11)	*1*

5.4. Conclusions.

Attempts to synthesis a new R-P n=2 phase of general formula $Sr_3(Mg_xMo_{1-x})_2O_{7-\delta}$ proved partially successful although it has not been possible to obtain a pure single phase. It has been obtained as the majority phase (which has been identified as a n = 2 Ruddlesden-Popper phase of formula $Sr_3Mg_{0.5}Mo_{1.5}O_{7-\delta}$) and the impurities identified as the double perovskite $Sr_2MgMoO_{6-\delta}$ and the pseudo perovskite $Sr_{11}Mo_4O_{23}$, both of them are discussed elsewhere in this thesis. The phase fraction in this sample has been calculated by Rietveld refinements and it has given a result of 71.11 (2.18) wt. % for the n=2 R-P $Sr_3Mg_{0.5}Mo_{1.5}O_{7-\delta}$, 19.28 (44) wt. % for the double perovskite $Sr_2MgMoO_{6-\delta}$ and 9.61 (16) % for the pseudo-perovskite $Sr_{11}Mo_4O_{23}$.

HRTEM of this compound shows numerous defects in the n=2 R-P phase which can be identified as isolated n=1 R-P type phase defects and the double perovskite $Sr_2MgMoO_{6-\delta}$, which appears as extended defects in the R-P n=2 matrix. In the same manner, EDS analysis in these crystals have given an average chemical formula $Sr_{2.68}Mg_{0.64}Mo_{1.67}$, a little different that the chemical formula expected $Sr_3Mg_{0.5}Mo_{1.5}O_{7-\delta}$. It appears from the synthetic work carried out that the n =2 R-P phase is only stable in conjunction with other phases which makes it's detailed analysis problematic.

5.5. References

(1) Ruddlesden, S. N.; Popper, P. *Acta Crystallogr.* **1958**, *11*, 54-55.

(2) Ruddlesden, S. N.; Popper, P. *Acta Crystallogr.* **1957**, *10*, 538-540.

(3) Prado, F.; Mogni, L.; Cuello, G. J.; Caneiro, A. *Solid State Ionics* **2007**, *178*, 77-82.

(4) Battle, P. D.; Rosseinsky, M. J. *Curr. Opin. Solid St. M.* **1999**, *4*, 163-170.

(5) Whaley, L. W.; Lobanov, M. V.; Sheptyakov, D.; Croft, M.; Ramanujachary, K. V.; Lofland, S.; Stephens, P. W.; Her, J. H.; Van Tendeloo, G.; Rossell, M.; Greenblatt, M. *Chem. Mater.* **2006**, *18*, 3448-3457.

(6) Veith, G. M.; Greenblatt, M.; Croft, M.; Ramanujachary, K. V.; Hattrick-Simpers, J.; Lofland, S. E.; Nowik, I. *Chem. Mater.* **2005**, *17*, 2562-2567.

(7) Chen, R.; Greenblatt, M.; Bendersky, L. A. *Chem.Mater.* **2001**, *13*, 4094-4100.

(8) Hungria, T.; MacLaren, I.; Fuess, H.; Galy, J.; Castro, A. *Mater. Lett.* **2008**.

(9) Boulahya, K.; Parras, M.; Gonzalez-Calbet, J. M. *Chem-Eur. J.* **2007**, *13*, 910-915.

(10) Prado, F.; Manthiram, A. *J. Solid St. Chem.* **2001**, *158*, 307-314.

(11) Sloan, J.; Battle, P. D.; Green, M. A.; Rosseinsky, M. J.; Vente, J. F. *J. Solid St. Chem.* **1998**, *138*, 135-140.

(12) Bernuy-Lopez, C.; Allix, M.; Bridges, C. A.; Claridge, J. B.; Rosseinsky, M. J. *Chem. Mater.* **2007**, *19*, 1035-1043.

(13) Steiner, U.; Reichelt, W.; Schmidt, M.; Schnelle, W. Z. *Anorg. Allg. Chem.* **2004**, *630*, 649-654.

Chapter 6:

$Sr_{11}Mo_4O_{23}$ a vacancy ordered variant of the cryolite structure

6.1. Introduction.

Perovskite are amongst the most heavily investigated structural families in solid state chemistry. The structure has been described in section 1.3.1. Many systems with mixed occupancy on cation sites form ordered superstructures, in general B cation-ordering is more common than A cation ordering[1,2]. Amongst the B site ordered systems is the cryolite structure A_3BO_6 (named after a mineral of composition Na_3AlF_6) where the larger cation adopts two distinct coordination environments. As discussed in chapter 5 we observed "Sr_3MoO_6" as an impurity during the attempted synthesis of $Sr_3Mg_{0.5}Mo_{1.5}O_{7-\delta}$. Given that these materials have the potential to be mixed conductors under suitable conditions a further investigation into the "Sr_3MoO_6" composition was carried out.

Cation deficiency has been observed in similar systems. A-site vacancy-orderings are found in compounds such as $Li_{0.18}La_{0.61}\square_{0.21}TiO_3$[3], $Sr_{1-3x/2}La_x\square_{x/2}TiO_3$[4], $(Ba_{7/4}\square_{1/4})BaOsO_6$[5], $(Sr_{7/4}\square_{1/4})SrReO_6$[6], $(La_{4/3}\square_{2/3})MgWO_6$[7] or $(Ba_{7/4}\square_{1/4})BaWO_{5.75}$[8,9]. Examples of B-site vacancy ordered perovskites include $Ba_2(B_{3/4}\square_{1/4}Sb)O_6$ (B = Ce[10,11], Zr[11]).

Prior to this study the compounds reported in the ternary system Sr-Mo-O are Sr_2MoO_4[12,13], $Sr_3Mo_2O_7$[14,15], $SrMoO_4$[16], $SrMoO_3$[17], $SrMo_5O_8$[17] and Sr_3MoO_6[18]. As it can be seen molybdenum can adopt several different oxidation states. This oxidation states richness provides the promise of interesting electric properties. Curiously, full structural determinations have been carried out for all the compounds except for the compounds named Sr_3MoO_6. Figure 1 shows the ternary Sr-Mo-O phase diagram, constructed from the reported phases[17]. Sr_3MoO_6 was first reported by McCarthy et al. in 1973[18]. In that report the X-Ray powder data have been indexed in a cubic cell with a= 16.39 (1) Å but the full structural determination was not attempted. In this chapter, the structural characterisation of a new cryolite-type material of chemical formula $Sr_{11}Mo_4O_{23}$ will be presented.

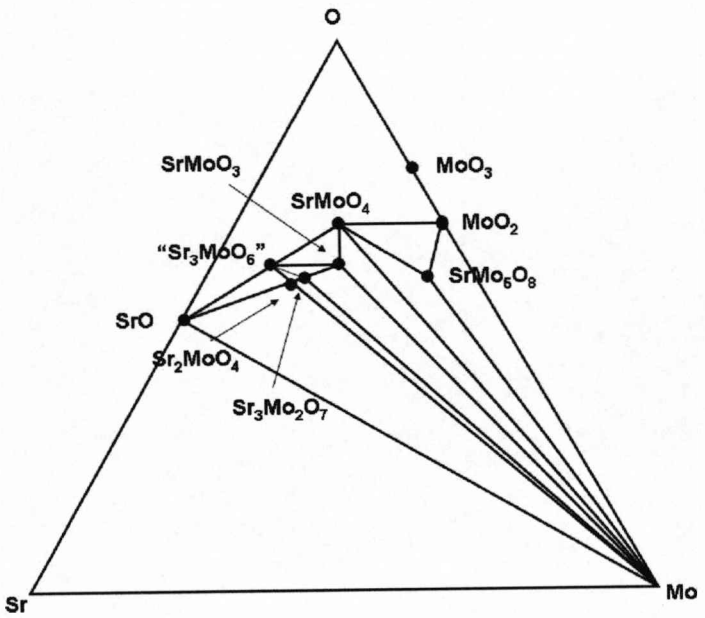

Figure 1. *The ternary phase diagram in the Sr-Mo-O system showing the different phases reported*[17].

6.2. Experimental.

Sr_3MoO_6 and $Sr_{11}Mo_4O_{23}$ samples were prepared by direct reaction of $SrCO_3$ and MoO_3 in stoichiometric quantities. The powder was pressed into bars and calcined at 900 °C for 12 h and 1200 °C for 24 h in air. The samples were reground, pressed into bars again and refired at 1300 °C for 24 h in air. At this point, powder X-ray diffraction indicated that $Sr_{11}Mo_4O_{23}$ sample was single phase while Sr_3MoO_6 showed multiphase formation.

In order to do the physical measurements, the compound was ground again and uniaxilly pressed into pellets under 300 MPa pressure. The pellets

were sintered at 1000 °C during 24 h. The relative densities of the pellets were calculated according to the weight and dimensions of the pellets. Density values of 85-90 % were obtained for the material.

Other experimental information can be found in chapter 2.

6.3. Results.

Initial attempted samples to synthesise "Sr_3MoO_6" were analysed by EDS. This confirmed the presence of a main phase with a Sr/Mo cation ratio close to 2.75 and the presence of some crystallites which had a Sr/Mo cation ratio close to 8. In an attempt to isolate a single phase the synthesis of $Sr_{11}Mo_4O_{23}$ (Sr/Mo = 2.75) was attempted. EDS analysis confirmed the homogeneity of the sample and that the Sr/Mo cation ratio is close to the starting 2.75 ratio. The presence of a very small number of crystallites with a Sr/Mo cation ratio close to 1 was detected indicating the presence of $SrMoO_4$[12,13]as a minor impurity. Attempting to isolate the phase with a Sr/Mo cation ratio close to 8 only yielded mixed phase products.

$Sr_{11}Mo_4O_{23}$ was observed by TEM techniques (ED and HREM images) in order to define the structural features. The analysis of the reciprocal space is not consistent with the previous cubic indexation reported for "Sr_3MoO_6". This is illustrated by the $[001]_{cubic}$ oriented ED pattern shown in Figure 2. From this experimental pattern we can see that the $[1\bar{1}0]_{cubic}$ and $[\bar{1}\bar{1}0]_{cubic}$ directions are not perfectly orthogonal due to a slightly distortion between *a* and *b* cell parameters.

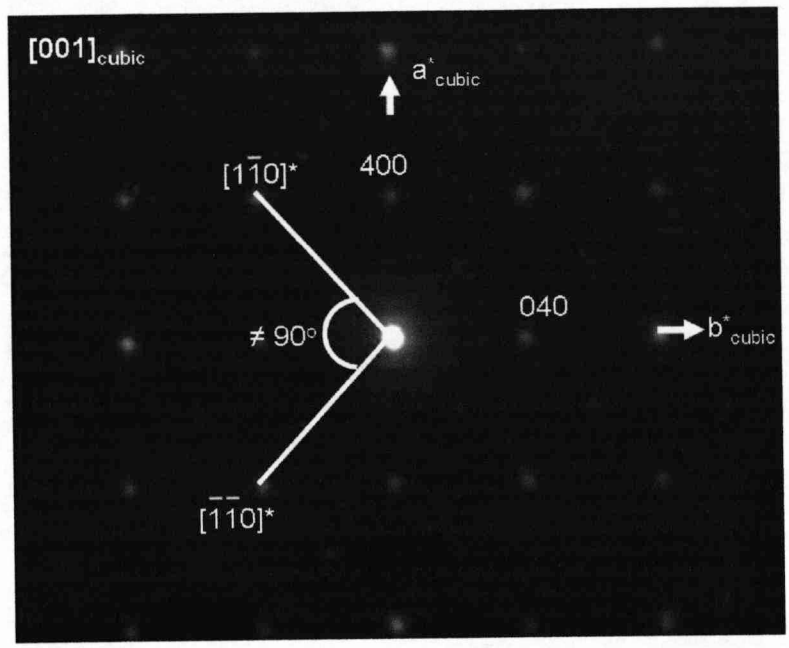

Figure 2. *Experimental Electron Diffraction patterns observed for* $Sr_{11}Mo_4O_{23}$ *along to the* $[001]_{cubic}$ *zone axis indexed in a cubic cell.*

Powder X-Ray diffraction data of $Sr_{11}Mo_4O_{23}$ can be indexed in the tetragonal $I4_1/a$ space group with a = 11.5974 (1) Å and c = 16.3986 (2) Å. The sample is yellow-greenish. Figure 3 (a) compares the powder X-Ray diffraction patterns of "Sr_3MoO_6" and "$Sr_{11}Mo_4O_{23}$" compositions. Figure 3 (b) shows an enlargement of the low angle region where it can be clearly seen that several reflections present in "Sr_3MoO_6" are absent in $Sr_{11}Mo_4O_{23}$. It can also be seen that the peaks of the main phase in $Sr_{11}Mo_4O_{23}$ are sharper than "Sr_3MoO_6" showing that the sample is more crystalline.

a

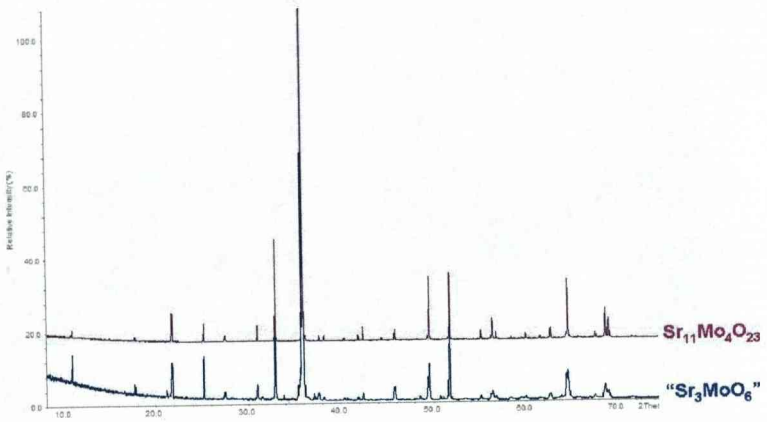

b

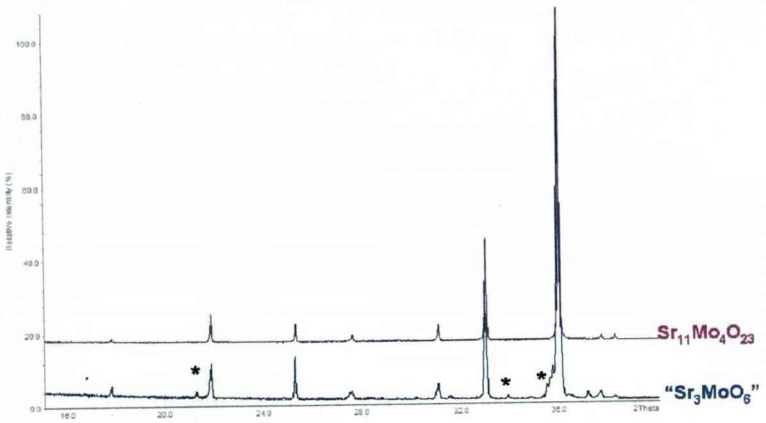

Figure 3. *(a) Powder X-Ray diffraction patterns showing the difference between the syntheses with composition "Sr_3MoO_6" and $Sr_{11}Mo_4O_{23}$. (b) Enlarged view of the low angle region. Stars highlight some of the peaks due to the minor impurity phases in "Sr_3MoO_6" not present in $Sr_{11}Mo_4O_{23}$.*

Initial attempts at structure solution were attempted in $I4_1/a$ using laboratory powder X-ray diffraction data (Figure 4 and Table 1). Figure 5

shows the structural model derived from this refinement. The perovskite structure is confirmed with a clear ordering between Sr and Mo species on the B-site and the presence of A-site vacancies leading to the formulation of the structure as $(Sr_7\square_1)Sr_4Mo_4O_{23}$ as in the related system $(Ba_{7/4}\square_{1/4})BaWO_{5.75}$[8,9]. Although it was possible to obtain a reasonable fit (χ^2 = 3.703) in this space group, it can be seen that the Mo-sites are very distorted leading to unreasonable Mo-O and O-O distances in the structure.

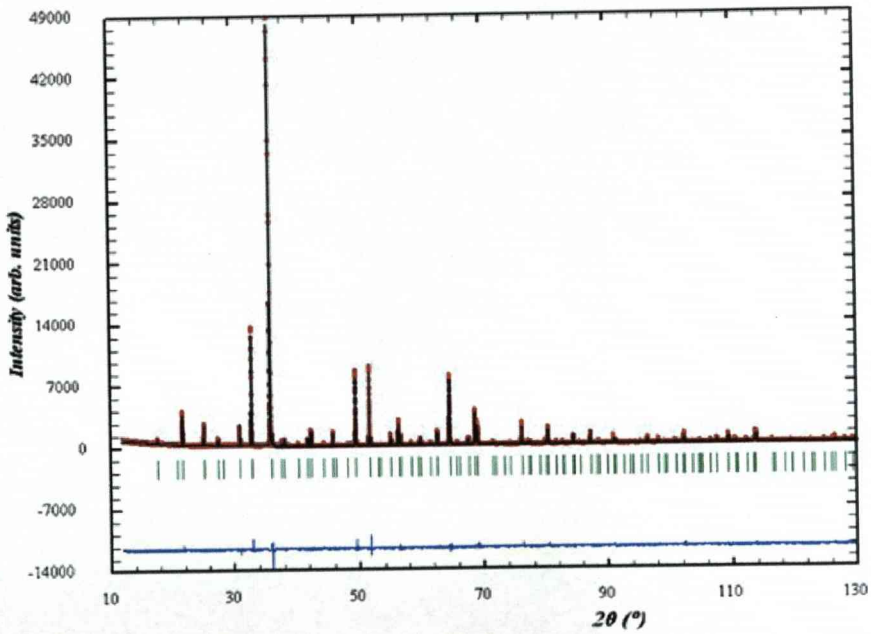

Figure 4. *Rietveld refinement plot of $Sr_{11}Mo_4O_{23}$ using the laboratory powder X-Ray diffraction data. Red crosses are the observed data, the solid black line is the calculated pattern the blue line is the difference and the green tick marks show the positions of the Bragg peaks.*

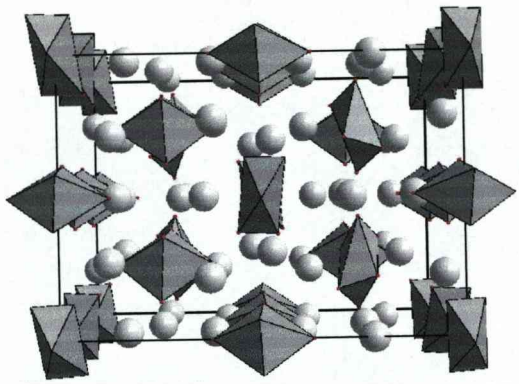

Figure 5. *Refined structure of $Sr_{11}Mo_4O_{23}$ obtained from the powder X-Ray diffraction data. Viewed along [010].*

Table 1. *Fit parameters, refined atomic positions, site occupancies and isotropic displacements for $Sr_{11}Mo_4O_{23}$ based on the laboratory powder X-Ray diffraction data.*

Atom	Site	x	y	z	B (Å^2)	Occupancy
Sr1	*16f*	0.2873 (8)	0.0245 (7)	0.8718 (8)	1.87 (25)	1.000
Sr2	*16f*	0.2070 (7)	0.2546 (11)	0.0259 (7)	2.64 (13)	1.000
Sr3	*8e*	0	0.2500	0.4083(10)	2.75 (58)	1.000
Sr4	*4b*	0	0.2500	0.6250	2.13 (23)	1.000
Mo1	*8c*	0	0	0	1.94 (11)	1.000
Mo2	*8d*	0	0	0.5	1.98 (12)	1.000
O1	*16f*	0.8657	0.4564	0.0403	1.50	0.875
O2	*16f*	0.4202	0.367	0.0094	1.50	1.000
O3	*16f*	0.5000	0	0.1257	1.50	1.000
O4	*16f*	0.3852	0.1055	0	1.50	1.000
O5	*16f*	0.9910	0.171	0	1.50	1.000
O6	*16f*	0.1304	0.5881	0.0594	1.50	0.875

Space group: $I4_1/a$. a = 11.5974 (1) Å, c = 16.3986 (2) Å, χ^2 = 3.703, R_p = 9.12 %.

Given the problems discussed above with the model neutron diffraction data was collected on the HRPD diffractometer at ISIS. All attempts to fit the data obtained using the model derived from the X-ray diffraction data were unsatisfactory. Rexamination of the electron diffraction patterns showed that it was also possible to index them based on a larger R centred cell derived from the originally reported $4a_p$ cubic perovskite superstructure ($\mathbf{a}_{rhom} = \frac{1}{2}\mathbf{a}_{cubic} - \frac{1}{2}\mathbf{c}_{cubic}$, $\mathbf{b}_{rhom} = -\frac{1}{2}\mathbf{a}_{cubic} + \frac{1}{2}\mathbf{b}_{cubic}$, $\mathbf{c}_{rhom} = 2(\mathbf{a}_{cubic} + \mathbf{b}_{cubic} + \mathbf{c}_{cubic})$. This yielded a better LeBail fit to the powder neutron diffraction data (Figure 6a) in $R\bar{3}m$. However as can be seen peak splitting could be observed clearly in the difference plot. Whilst this was improved using the monoclinic subgroup C2/m (Figure 6b) misfits are still noticeable on several peaks. Thus the structure was reduced to triclinic ($\mathbf{a}_{tric} = \frac{2}{3}\mathbf{a}_{rhom} + \frac{1}{3}\mathbf{b}_{rhom} + \frac{1}{3}\mathbf{c}_{rhom}$, $\mathbf{b}_{tric} = -\frac{1}{3}\mathbf{a}_{rhom} + \frac{1}{3}\mathbf{b}_{rhom} + \frac{1}{3}\mathbf{c}_{rhom}$, $\mathbf{c}_{tric} = -\frac{1}{3}\mathbf{a}_{rhom} - \frac{2}{3}\mathbf{b}_{rhom} + \frac{1}{3}\mathbf{c}_{rhom}$) and this yielded a significantly better fit (Figure 7).

a

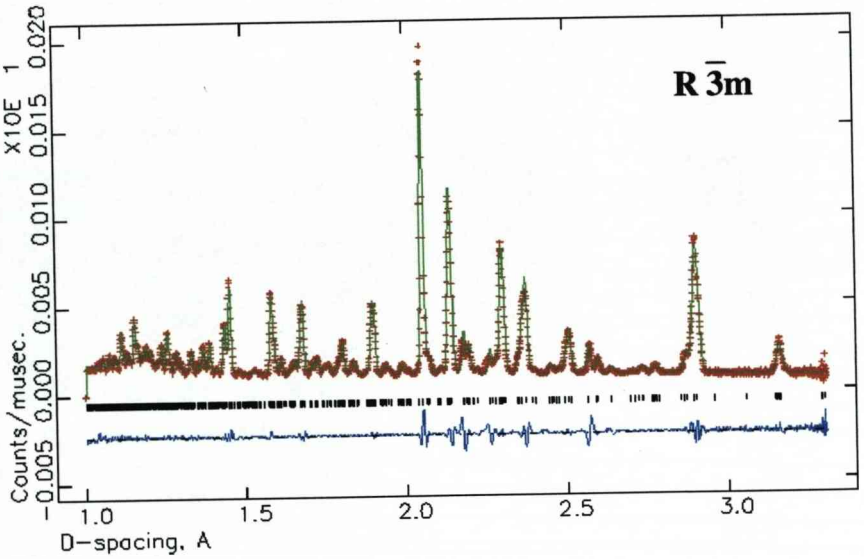

b

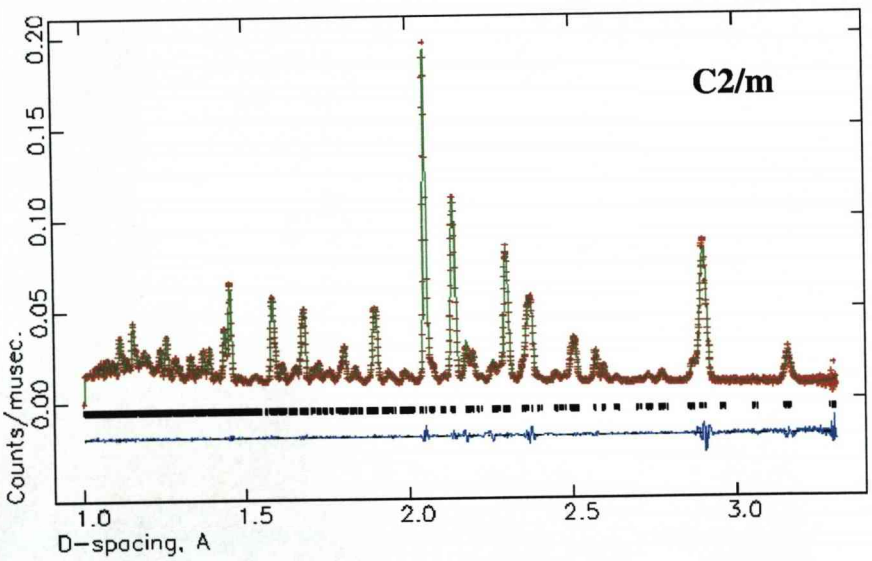

Figure 6. *Plots of the Le Bail fits for $Sr_{11}Mo_4O_{23}$ compound in space groups (a) $R\bar{3}m$ and (b) C2/m space group respectively. Crosses are observed data, the solid red line is the calculated pattern and the blue line is the difference.*

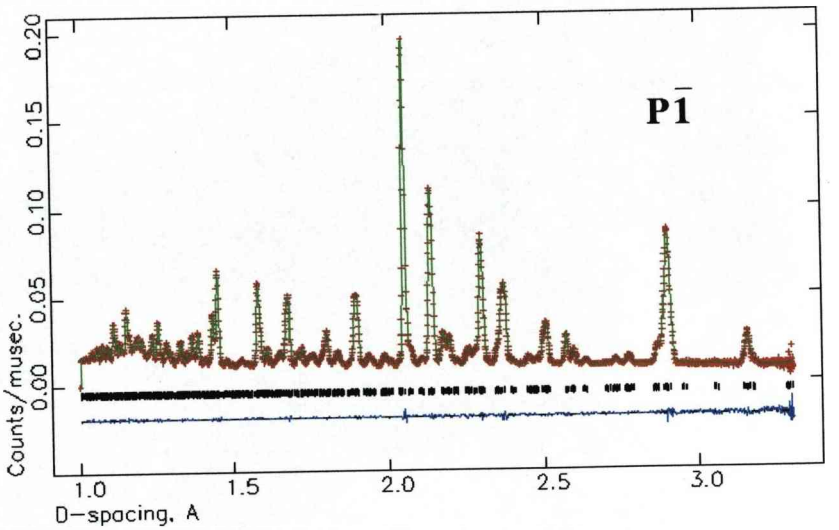

Figure 7. *Plots of the Le Bail fits for $Sr_{11}Mo_4O_{23}$ in $P\bar{1}$. Crosses are observed data, the solid red line is the calculated pattern and the blue line is the difference.*

Table 2. *Fit parameters and refined cell parameters for the Le Bail fits rhombohedral, monoclinic and triclinic cells for $Sr_{11}Mo_4O_{23}$.*

	Rhombohedral	**Monoclinic**	**Triclinic**
$\mathbf{R_{exp}}$	1.966	1.705	2.325
$\mathbf{R_{wp}}$	33.32	5.77	4.89
$\boldsymbol{\chi^2}$	16.95	3.384	2.116
a (Å)	11.6279 (1)	38.4058 (2)	20.1720 (1)
b (Å)		11.5837 (1)	20.1463 (1)
c (Å)	56.6595 (7)	20.0466 (1)	20.1323 (1)
V ($Å^3$)	6634.45 (12)	4414.09 (3)	2211.62 (1)
α (degrees)	90	90	33.505 (1)
β (degrees)	120	150.334 (1)	33.456 (1)
γ (degrees)	90	90	33.336 (1)

Table 2 summarizes fit parameters and refined cell parameters for the rhombohedral ($R\bar{3}m$), monoclinic (C2/m) and triclinic ($P\bar{1}$) Le Bail fits. At this point it is worth noting that the various cells $R\bar{3}m$, C2/m, $P\bar{1}$ and $I4_1/a$ are all subgroups of the $Fd\bar{3}m$ 16 fold perovskite superstructure reported for the analogous compound $Ba_{11}W_4O_{23}$. Though not derived in this manner the $P\bar{1}$ cell is also a subgroup of the $I4_1/a$ cell. The tetragonal $I4_1/a$ structural model describes the XRD data reasonably but not the neutron diffraction data. It can however provide a reasonable model for the heavy atom positions. To date the details of the light atom position in the triclinic structure have yet to be determined.

Variable temperature XRD and NPD data were collected for $Sr_{11}Mo_4O_{23}$ in order to ascertain whether any transitions to higher symmetry structures occurred above ambient temperature. Figure 8 shows the XRD data collected between RT and 425 °C. No obvious phase transition is visible in this data. Figure 9 shows the NPD data collected on the POLARIS diffractometer at ISIS between RT and 700 °C. It can be clearly seen that several peaks disappear between the 500 °C and 600 °C and that the material has begun to decompose at 700 °C due to the reducing atmosphere produced by the vanadium can used.

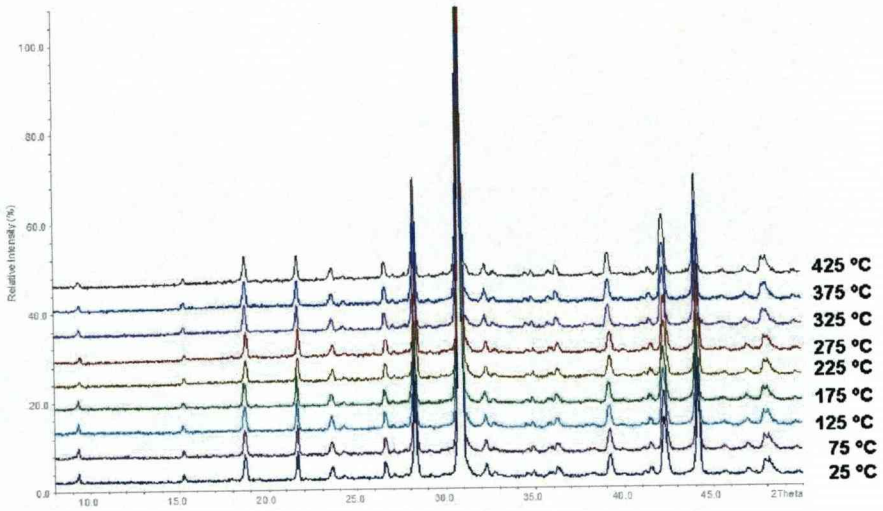

Figure 8. *Variable temperature powder X-Ray diffraction patterns for the* $Sr_{11}Mo_4O_{23}$ *in the range 25 °C-425 °C.*

a

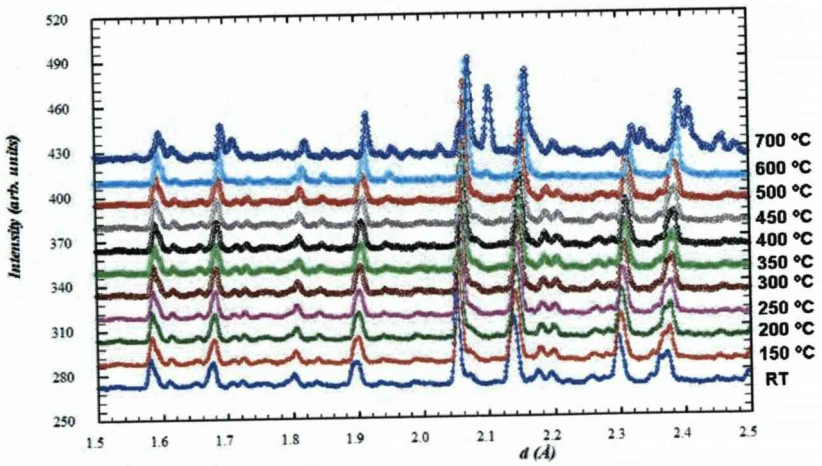

b

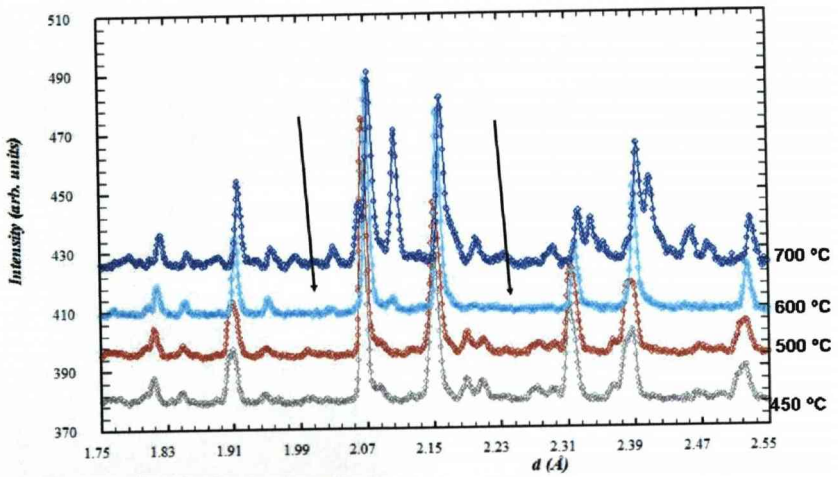

Figure 9. *(a) Variable temperature neutron powder diffraction data collected on the Polaris diffractometer at ISIS over the temperature range RT-700 °C for $Sr_{11}Mo_4O_{23}$. (b) Selected temperatures and d-spacing region showing the phase transition between 500 °C and 600 °C for $Sr_{11}Mo_4O_{23}$.*

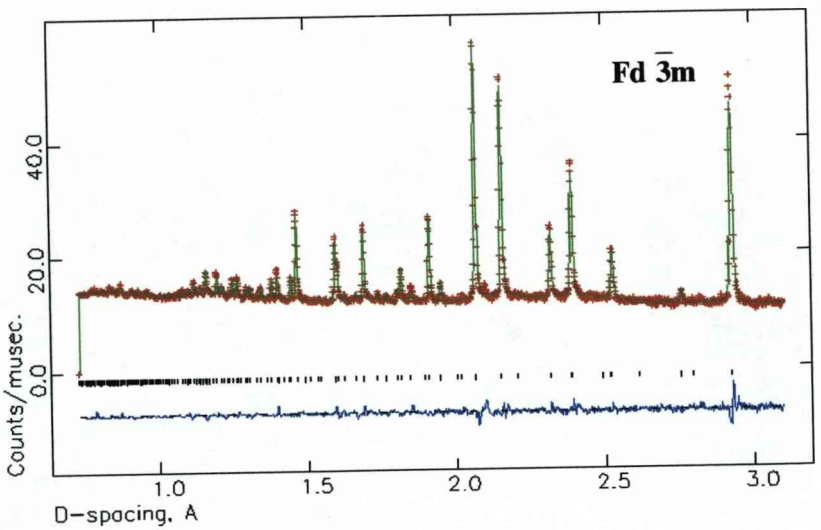

Figure 10. *Rietveld refinement plot of the backscattering bank data for* $Sr_{11}Mo_4O_{23}$ *at 600 °C in the cubic* $Fd\bar{3}m$ *space group.* $\chi^2 = 1.538$, $wR_p = 1.59$ %, $R_p = 2.48$ %, $a = 16.5571$ (1) Å. *Crosses are observed data, the solid red line is the calculated pattern and the blue line is the difference.*

The 600 °C data was used in order to probe the refine the structure of the high temperature phase. This data can be fitted using the $Fd\bar{3}m$ cubic model reported for the analogous compound $Ba_{11}W_4O_{23}$[8,9]. Figure 10 shows the NPD data refinement. Table 3 gives the refined structural parameters for this structural model.

Table 3. *Refined atomic positions, site occupancies and isotropic displacements for* $Sr_{11}Mo_4O_{23}$ *at 600 °C.*

Atom	Site	x	y	z	Uiso (Å x 10^2)	Occupancy
Sr1	*8b*	0.375	0.375	0.375	3.59 (20)	1
Sr2	*48f*	0.3998 (1)	0.125	0.125	5.09 (14)	1
Sr3	*32e*	0.2279 (1)	0.2279 (1)	0.2279 (1)	6.68 (13)	1
Mo1	*16d*	0.5	0.5	0.5	2.09 (10)	1
Mo2	*16c*	0	0	0	3.12 (13)	1
O1	*96g*	0.4983 (1)	0.4983 (1)	0.6148 (1)	5.11 (10)	1
O2	*96g*	0.0785 (3)	0.0785 (3)	–0.0149 (5)	5.68 (40)	0.750
O3	*96h*	0	0.0798 (2)	–0.0798 (2)	5.68 (40)	0.083
O4	*96g*	0.0096 (6)	0.0096 (6)	–0.1094 (11)	5.68 (40)	0.083

In order to probe the electrical properties of $Sr_{11}Mo_4O_{23}$ alternating current (AC) impedance spectroscopy was carried on $Sr_{11}Mo_4O_{23}$. Figure 11 shows the result of AC impedance spectroscopy measurements for $Sr_{11}Mo_4O_{23}$ between 200 °C and 800 °C. Impedance data in the 500-700 °C temperature range exhibit a significant Warburg electrode response[19,20] with an associated large capacitance (> 10^{-7} F cm^{-1}) in the low frequency range (< 10 Hz), which is diagnostic of ionic conduction with partially blocking electrodes. The bulk and grain boundaries responses at higher frequencies overlap to form an asymmetric semicircular arc. The total resistivity (R_b + R_{gb}) for $Sr_{11}Mo_4O_{23}$ was extracted from the intercept of the semicircular arc at low. Above 700 °C, the electrode response dominated the impedance data and the semicircular arc collapsed; the intercept of the electrode response at high frequency was extracted as the total resistivity in this case.

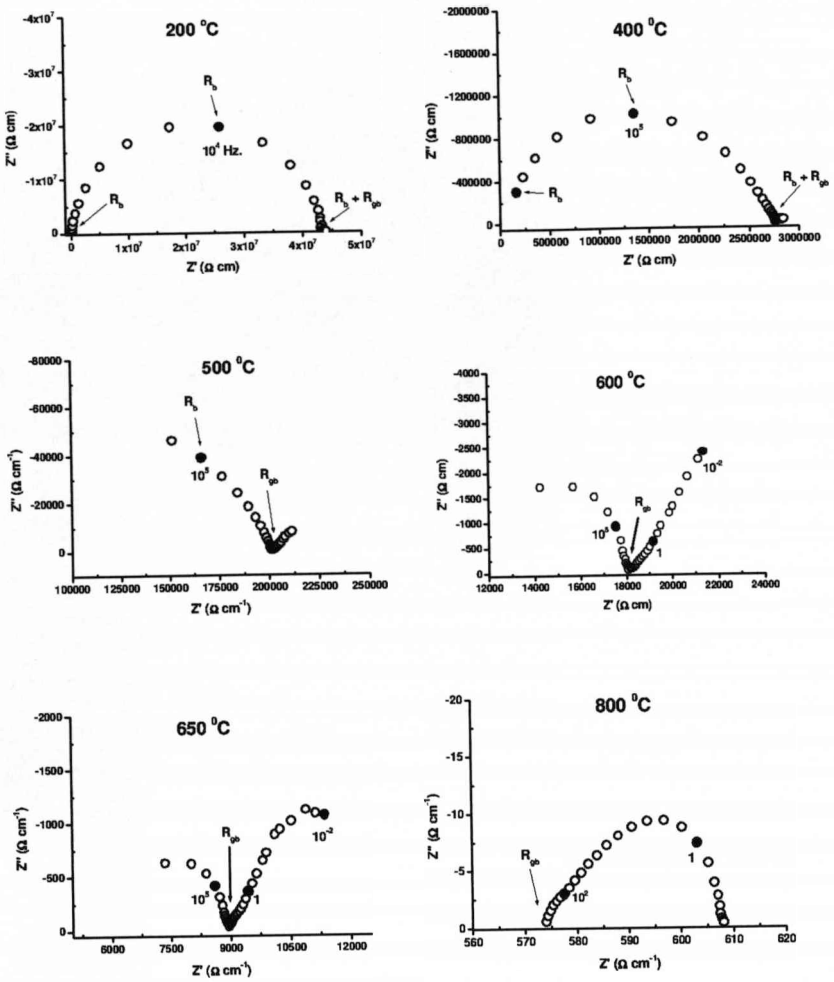

Figure 11. *AC impedance spectroscopy measurements in air over the 200 °C-800 °C temperature range for* $Sr_{11}Mo_4O_{23}$.

Figure 12 shows the Arrhenius plot calculated from the impedance data at low frequencies (<1 Hz) measured in air. From 500-800 °C this material shows a conductivity of ~10^{-3} S cm^{-1}. This conductivity is slightly lower than those for the silicate apatites and YSZ (10^{-2} S cm^{-1}) which have been reported as good ionic conductors[21]. These data show that $Sr_{11}Mo_4O_{23}$

is a poor oxide-ion conductor with very small ionic contribution to the overall conductivity.

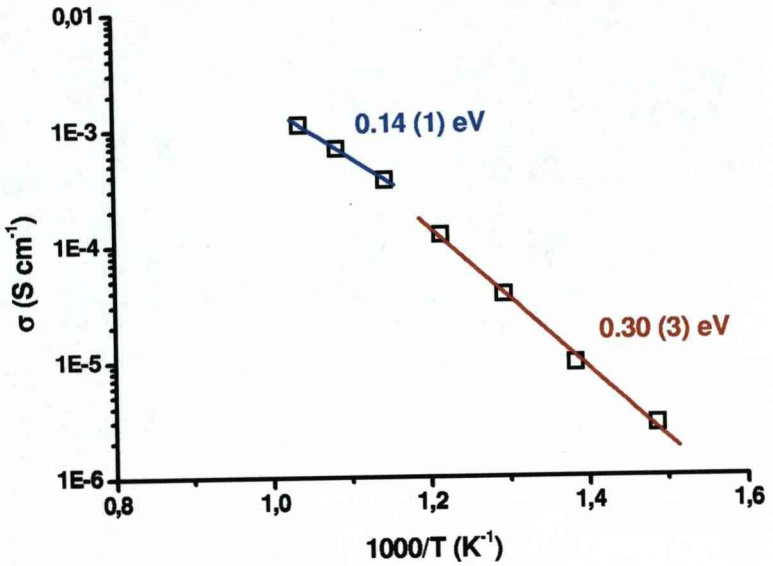

Figure 12. *Arrhenius plot of the total conductivity for $Sr_{11}Mo_4O_{23}$. The activation energies are marked on the graph.*

6.4. Discussion.

It has been shown above that $Sr_{11}Mo_4O_{23}$ is the correct composition of the previously reported phase "Sr_3MoO_6" [18]. Above 600 °C the material appears isostructural with the analogous compound $Ba_{11}W_4O_{23}$[8,9]. The low temperature structure of $Sr_{11}Mo_4O_{23}$ is still unresolved. Attempts to verify the proposed symmetry derived from Le Bail fits of the neutron powder

diffraction by ED and HREM are hampered by complex twinning phenomena as shown in Figure 13. Extra spots are observed on the ED patterns (marked with a red circle in Figure 13) that are not observed in some Fourier transformers of selected areas of the HRTEM images Figure 13.

Other defects can be observed as shown in Figure 14 for $[100]_{cubic}$ and Figure 15 for $[111]_{cubic}$. In both cases one would expect the Fast Fourier Transform (FFT) would be the same for different areas. However, it can be seen that these FFT images are different for each projection which show that this compound presents numerous different twin domains exhibiting small domain sizes. At room temperature the neutron diffraction data can only be fit using a triclinic cell. This structure has not yet been solved. Some similarities should be noted with $Ca_3Nb_{2-x}V_xO_8$ compound reported by Cranswick et al[22]. This compound was described with vacancies in both the anion sites and A-cation sites. This report shows the complexity of the room temperature structure and outlines some of the difficulties that need to be overcome to solve the structure.

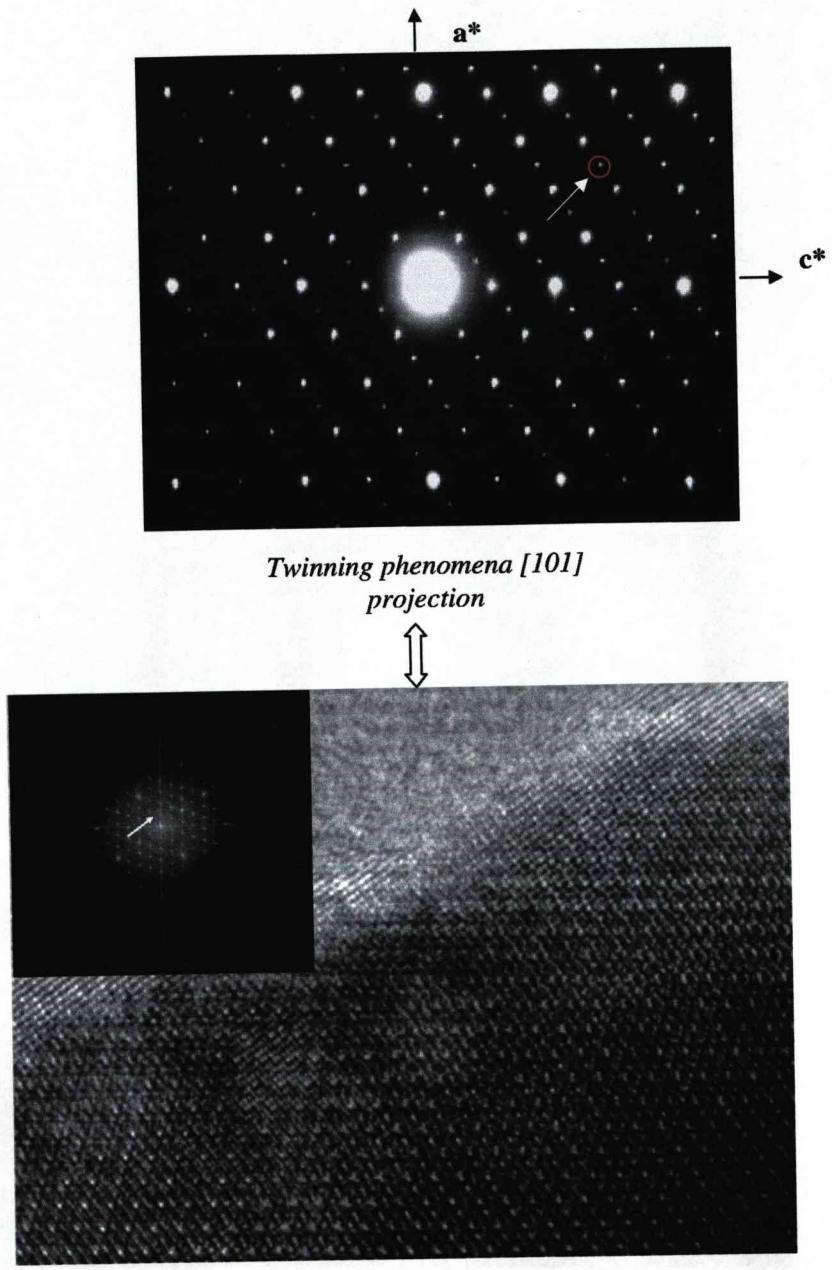

Figure 13. *Electron diffraction pattern (top) and the HREM (bottom) image of the [101] projection for* $Sr_{11}Mo_4O_{23}$*. The insert shows the Fast Fourier transform (FFT) of the HREM. The extra peaks observed in the ED patterns are absent in the FFT (it's location is marked by the arrow).*

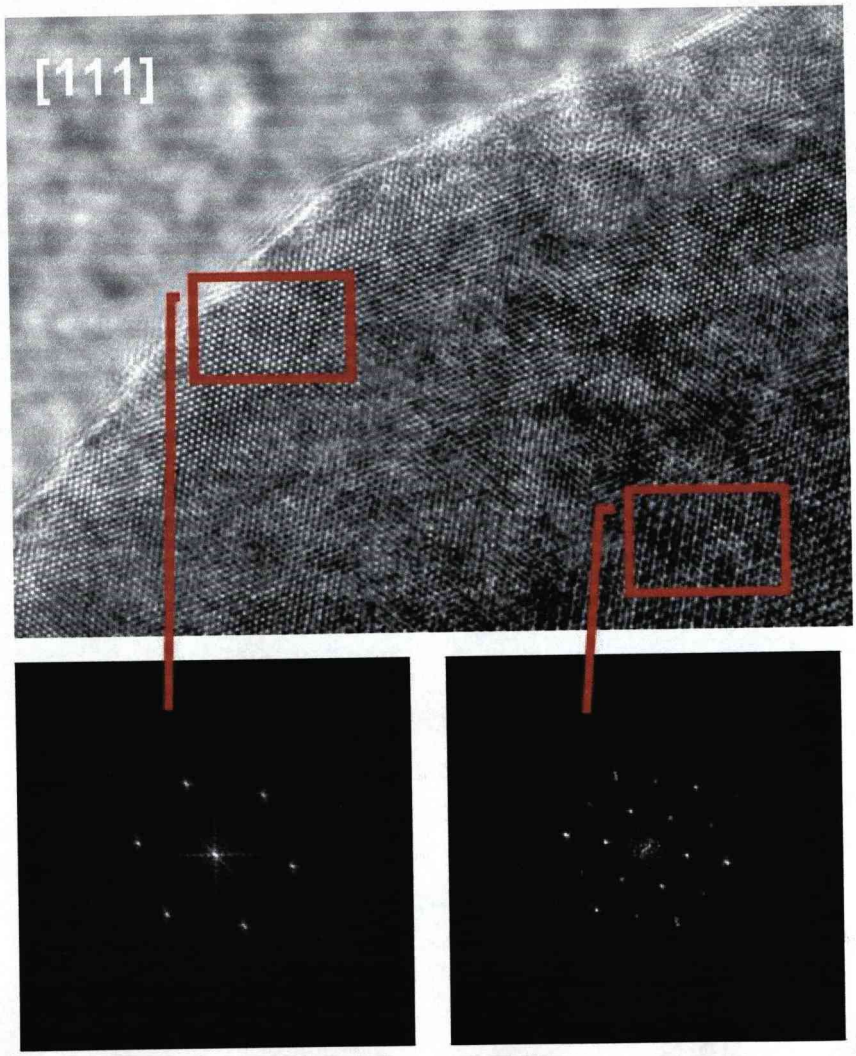

Figure 14. *HREM image of $Sr_{11}Mo_4O_{23}$ in the $[100]_{cubic}$ projection top and below FFT images of selected areas showing two different orientations.*

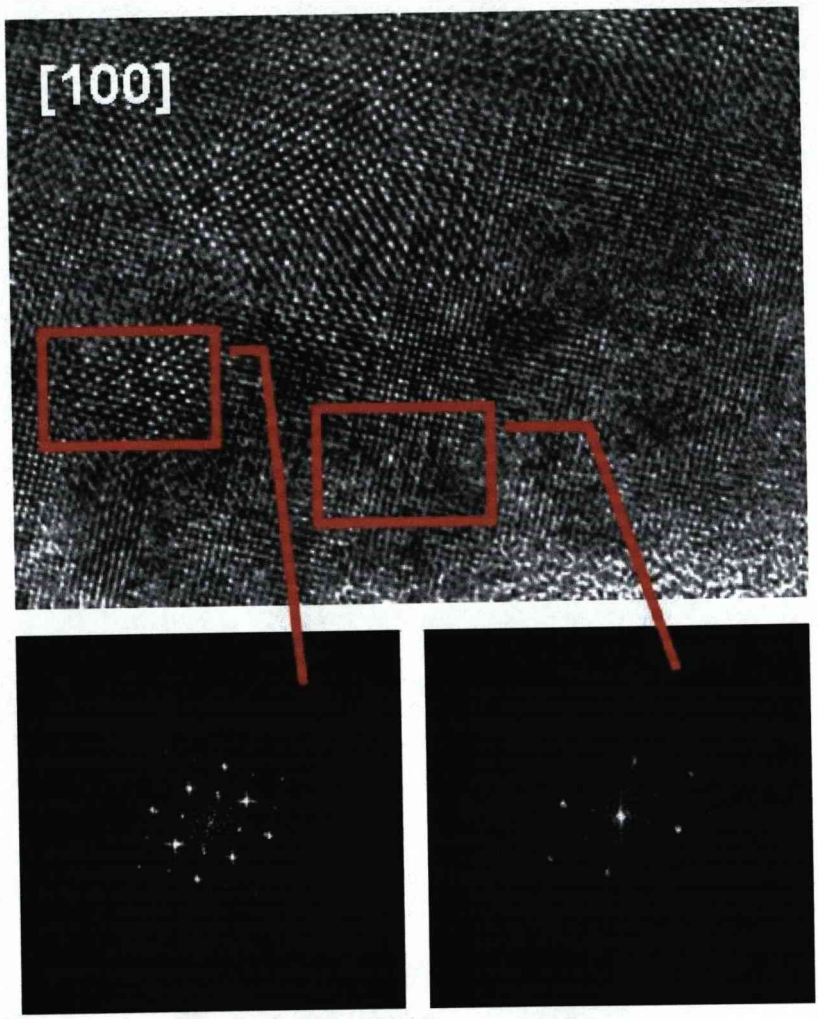

Figure 15. *HREM image of $Sr_{11}Mo_4O_{23}$ in the $[111]_{cubic}$ projection top and below FFT images of selected areas showing two different orientation.*

Above 500 °C the material adopts a simpler structure. Rietveld refinements showed that the material is isostructural with $Ba_{11}W_4O_{23}$. Figure 16 shows the derived structural model of $Sr_{11}Mo_4O_{23}$ oxide at 600

°C. The coordination around Mo2 is complex and very similar to that reported for W by Hong[9] in $Ba_{11}W_4O_{23}$. As for W, the Mo would adopt a polyhedron that could be decomposed into an octahedron and four different tetrahedral orientations as shown by Hong[9], although other polyhedral environments such as square pyramidal MoO_5 can not be excluded. One problem in this structural model is that the oxygen content is a little overestimated. This model leads when freely refined to an oxygen content of 24.5 O per formula unit which would suppose an unphysical oxidation state for the Mo of greater than +6. As this is not physical reasonable, the oxygen content was fixed to 23 O as in the fully oxidised formula $Sr_{11}Mo_4O_{23}$, though the fit was slightly worse (χ^2 (24.5O) = 1.354 vs χ^2 (23O) = 1.538) Table 4 shows the bond length for the cubic model for $Sr_{11}Mo_4O_{23}$.

Table 4. *Refined bond lengths distances for $Sr_{11}Mo_4O_{23}$ in the $F\,d\,\bar{3}\,m$ cubic space group at 600 C.*

Bond	Distance (Å)
Sr1_O1 x 12	2.9714 (31)
Sr2_O1 x 4	2.6629 (12)
Sr2_O1 x 2	2.8972 (31)
Sr2_O2 x 2	2.485 (8)
Sr2_O3 x 4	2.4875 (32)
Sr2_O4 x 2	2.784 (13)
Sr2_O4 x 4	3.2278 (21)
Sr3_O1 x 3	2.6489 (25)
Sr3_O2 x 6	2.714 (4)
Sr3_O3 x 6	2.999 (1)
Sr3_O4 x 3	2.097 (20)
Mo1_O1 x 6	1.9007 (20)
Mo2_O2 x 6	1.853 (6)
Mo2_O3 x 6	1.868 (6)
Mo2_O4 x 6	1.826 (18)

a

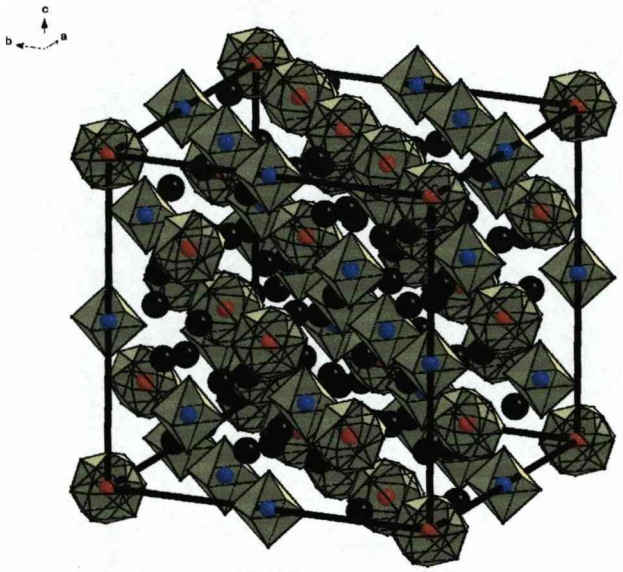

b

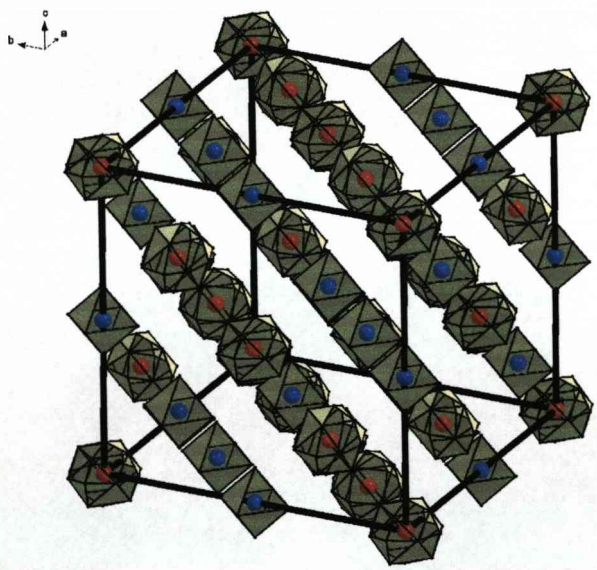

Figure 16. *(a) Refined structure of* $Sr_{11}Mo_4O_{23}$ *in the cubic* $F\,d\,\bar{3}\,m$ *space group. (b) Refined structure showing only the Mo positions. Black spheres are Sr, blue spheres Mo1 at the centre of an octahedron and red spheres Mo2 at the centre of a complex oxygen polyhedron.*

6.5. Conclusions

$Sr_{11}Mo_4O_{23}$ was successfully synthesised and it has been shown that it is the main phase in the named-"Sr_3MoO_6" oxide discovered in the 70's. The NPD data can be Le Bail fitted using a triclinic cell $P\bar{1}$ with the parameters a = 20.1720 (1) Å, b = 20.1463 (1) Å, c = 20.1323 (1) Å, α = 33.505 (1) °, β = 33.456 (1) ° and γ = 33.336 (1) °. This complexity can be related to the presence of several defects and twining phenomena in the structure observed by HREM images. Further studies are ongoing in order to find a correct structural model for this compound at room temperature.

The presence of a structural transition between 500 °C and 600 °C from this complex structure to a simpler structure is observed from NPD data. This high temperature phase can be refined in a cubic $Fd\bar{3}m$ space group with a = 16.5571 (1) Å. This structure is similar to the one described by Hong et al. for the analogous compound $Ba_{11}W_4O_{23}$.

Finally, $Sr_{11}Mo_4O_{23}$ has been studied by AC Impedance Spectroscopy and it was shown to be an ionic conductor behaviour over the 500-600 °C temperature range, with an oxide ion conductivity of 10^{-3} S cm^{-1}.

6.6. References

(1) Mitchell, R., H. *Perovskite:Modern and Ancient, Almaz Press, Inc., Thunder Bay, Ont.*, **2002**.

(2) Anderson, M. T.; Greenwood, K. B.; Taylor, G. A.; Poeppelmeier, K. R. *Prog. Solid State Ch.* **1993**, *22*, 197-233.

(3) Varez, A.; Inaguma, Y.; Fernandez-Diaz, M. T.; Alonso, J. A.; Sanz, J. *Chem. Mater.* **2003**, *15*, 4637-4641.

(4) Battle, P. D.; Bennett, J. E.; Sloan, J.; Tilley, R. J. D.; Vente, J. F. *J. Solid St. Chem.* **2000**, *149*, 360-369.

(5) Wakeshima, M.; Hinatsu, Y. *Solid State Commun.* **2005**, *136*, 499-503.

(6) Bramnik, K. G.; Miehe, G.; Ehrenberg, H.; Fuess, H.; Abakumov, A. M.; Shpanchenko, R. V.; Pomjakushin, V. Y.; Balagurov, A. M. *J. Solid St. Chem.* **2000**, *149*, 49-55.

(7) Khalyavin, D. D.; Senos, A. M. R.; Mantas, P. Q. *Journal of Phys-Condens. Mat.* **2005**, *17*, 2585-2595.

(8) Ha, J. S.; Lee, E.; Hong, S. T.; Yoo, H. I. *Solid State Ionics* **2008**.

(9) Hong, S. T. *J. Solid St. Chem.* **2007**, *180*, 3039-3048.

(10) Ijdo, D. J. W.; Helmholdt, R. B. *Acta Crystallogr. C* **1993**, *49*, 652-654.

(11) Treiber, U.; Kemmlersack, S. Z. *Anorg. Allg. Chem.* **1980**, *463*, 132-136.

(12) Shirakawa, N.; Ikeda, S. I.; Matsuhata, H.; Bando, H. *Jpn. J. Appl.Phys.* **2001**, *40*, L741-L743.

(13) Shirakawa, N.; Ikeda, S. I. *Physica C* **2001**, *364-365*, 309-312.

(14) Kouno, S.; Shirakawa, N.; Nagai, I.; Umeyama, N.; Tokiwa, K.; Watanabe, T. *Physica B* **2008**, *403*, 1029-1031.

(15) Kouno, S.; Shirakawa, N.; Nagai, I.; Umeyama, N.; Tokiwa, K.; Watanabe, T. *J. Phys. Soc. Jpn.* **2007**, *76*.

(16) Azad, A. K.; Eriksson, S. G.; Ivanov, S. A.; Mathieu, R.; Svedlindh, P.; Eriksen, J.; Rundlof, H. *J. Alloy. Compd.* **2004**, *364*, 77-82.

(17) Steiner, U.; Reichelt, W. *Z. Natursforsch. B.* **1998**, *53*, 110-116.

(18) McCarthy, G. J.; Gooden, C. E. *J. Inorg. Nucl. Chem.* **1973**, *35*, 2669-2672.

(19) West, A. R.; Sinclair, D. C.; Hirose, N. *J. Electrocer.* **1997**, *1*, 65-71.

(20) MacDonald, J., R., *Impedance Spectroscopy Emphasizing Solid Materials and Systems (Wiley, New York, 1987).*

(21) Kawada, T.; Sakai, N.; Yokokawa, H.; Dokiya, M. *Solid State Ionics* **1992**, *53-56*, 418-425.

(22) Cranswick, L. M. D.; Mumme, W. G.; Grey, I. E.; Roth, R. S.; Bordet, P. *J. Solid St. Chem.* **2003**, *172*, 178-187.

Chapter 7:

Synthesis and characterisation in the doping of the Ruddlesden-Popper system $LaSrAlO_4$

7.1. Introduction.

Ruddlesden-Popper (R-P) phases of general formula $A_{n+1}B_nO_{3n+1}$ have been the subject of considerable research[1,2] and are described in detail in section 1.3.2. They can be described as perovskite-like blocks *n* octahedra thick, separated by a rock-salt-type (A_2O_2) layer. Perovskite exemplifies the $n = \infty$ end member, whilst K_2NiF_4 exemplifies the n =1 structure. $LaSrAlO_4$ has been reported to adopt the K_2NiF_4 structure[3] (Figure 1). $LaSrAlO_4$ shows a n-type conduction at low oxygen partial pressure and a p-type

conduction close to $p(O_2) = 1$[4], though the parent compound is highly insulating at low temperature making these measurements rather difficult.

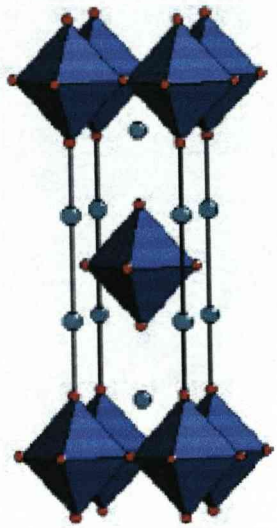

Figure 1. *Schematic illustration of $LaSrAlO_4$ where AlO_6 octahedra are drawn in blue and the (Sr,La) in green and the oxygen in red.*

Magnesium doped compositions compensated by lanthanum for strontium substitution with the general formula $La_{1+x}Sr_{1-x}Mg_xAl_{1-x}O_4$ ($0 \leq x \leq 0.7$) have recently been reported as promising ionic conductors[5-7]. In these compounds the magnesium is introduced in the B-site of the R-P structure without any significant change in the K_2NiF_4-type structure due to the charge compensation by varying the Sr/La ratio. In addition, $(La,Sr)_3(Fe,Ni)_2O_{7-\delta}$[8] and $La_{n+1}Ni_nO_{3n+1}$[9,10] have been reported as promising materials for solid oxide fuel cells cathodes. In these materials the variable nature of the Ni oxidation state can lead to the presence of oxygen interstitials or vacancies and increasing both electronic and ionic

conductivity. $La_2NiO_{4+\delta}$ is a typical example of this kind of materials where the possibility of oxidation states higher than nickel 2+ lead to an excess oxygen ($\delta \leq 0,14$), improving considerably their properties as mixed conducting oxides[11].

This chapter will discuss attempts to dope on the B-site of the $LaSrAlO_4$ system with cations such as Ni^{2+}, Co^{3+}, Ti^{4+}. This doping leads to the formation of materials with general formula $La_{1+x}Sr_{1-x}B_xAl_{1-x}O_{4\pm\delta}$ for which values $0 \leq x \leq 0.4$ were attempted. The aim of the introduction of these cations is the improvement of the electrical and ionic conductivity by means of the introduction of this 3d cations elements and the creation of oxygen vacancies or interstitial oxygen by adjusting the oxidation of these cations introduced. Two new materials $La_{1.1}Sr_{0.9}Ni_{0.1}Al_{0.9}O_{4\pm\delta}$ and $La_{1.2}Sr_{0.8}Ni_{0.2}Al_{0.8}O_{4\pm\delta}$ were synthesised and the structural data and physical characterization for both materials are presented.

7.2. Experimental.

$La_{1+x}Sr_{1-x}B_xAl_{1-x}O_4$ (B = Ni^{2+}, Co^{2+}, Ti^{4+}) for values $0 \leq x \leq 0.4$ were prepared by direct reaction of La_2O_3, $SrCO_3$, Co_3O_4, TiO_2, NiO and Al_2O_3 in stoichiometric quantities. The powders were ground in acetone in order to improve the homogeneity of the mix. Once the acetone was evaporated the powders were pressed into pellets and calcined at 900 °C for 8 h and 1300 °C for 24 h. Then, the samples were ground again, pressed into

pellets and refired at 1300 °C for 24 h. Finally, the materials were ground again, pressed into pellets and calcined at 1300 °C for 24 h.

In order to do the physical measurements the materials were ground again and uniaxilly pressed into pellets under 300 MPa pressure. The pellets were sintered at 1320 C for 24 h. The relative densities of the pellets were calculated according to their weight and dimension. Density values of 70 % were obtained for both materials.

Samples were prepared for synchrotron X-Ray diffraction in a 0.5 mm capillary and data were collected at room temperature on Station 9.1 of the SRS, Daresbury Laboratories, at a wavelength of 0.801717(1) Å.

Other experimental information can be found in chapter 2.

7.3. Results.

Powder X-Ray diffraction patterns of $La_{1+x}Sr_{1-x}Ni_xAl_{1-x}O_4$ (LSNAO) for $0 \leq x \leq 0.2$ show that these samples are single-phase having the tetragonal I4/mmm crystal structure of the n=1 member of the Ruddlesden-Popper series. For $0.3 \leq x \leq 0.4$ significant "$LaAlO_3$"-type and La_2O_3 oxides impurities are present. Figure 2 shows a comparison between the four samples in the system LSNAO. In the other cases, $La_{1+x}Sr_{1-x}B_xAl_{1-x}O_4$ (B = Co^{2+}, Ti^{4+}) for values $0 \leq x \leq 0.4$ and $La_{1+x}Sr_{1-x}Ni_xAl_{1-x}O_4$ for values $0.3 \leq x \leq 0.4$, the formation of a Ruddlesden-Popper phase was observed, however in all case a significant amount of "$LaAlO_3$" type phases and other unidentified impurities were always observed. Attempts to improve the

homogeneity of the mixture and avoid the formation of $LaAlO_3$ by ball milling proved unsuccessful and the presence of the $LaAlO_3$ as impurity was not reduced significantly. Further characterisations was not carried out on these materials due to the impossibility of de-convoluting any observed properties from those of doped $LaAlO_3$[12].

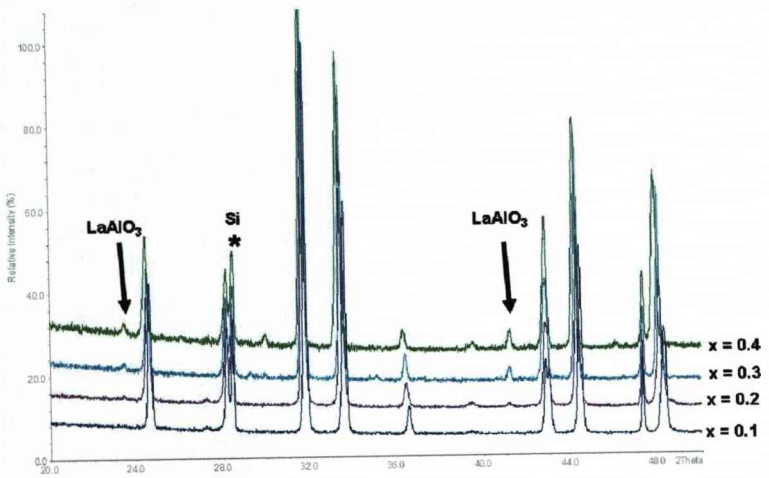

Figure 2. *XRD patterns for the system LSNAO for $0 \leq x \leq 0.4$. The level of the "$LaAlO_3$" impurity increases as x increases. The peaks marked with a star correspond to silicon ("Si-640c-NIST standard").*

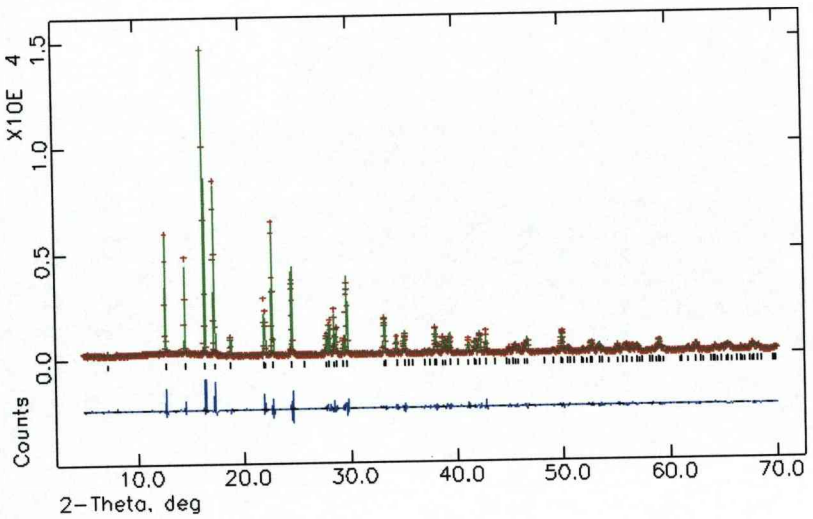

Figure 3. *Rietveld refinement of Synchrotron X-Ray of LSNAO_0.1. Crosses are observed data, the solid red line is the calculated pattern and the blue line is the difference. The tick marks correspond to Bragg reflections.*

The samples with composition $La_{1+x}Sr_{1-x}Ni_xAl_xO_4$ (LSNAO x = 0.1, 0.2) were analysed by EDS. The results of this analysis confirmed its homogeneity and the correct cation ratio in both materials.

Rietveld refinements of Synchrotron X-Ray data confirmed the structural model with space group I4/mmm for $La_{1.1}Sr_{0.9}Ni_{0.1}Al_{0.9}O_4$ (LSNAO_0.1) and $La_{1.2}Sr_{0.8}Ni_{0.2}Al_{0.8}O_4$ (LSNAO_0.2) (Figure 3 and 4). Satisfactory χ^2 values were obtained for both materials, χ^2 = 2.800 for LSNAO_0.1 and χ^2=3.117 for LSNAO_0.2. Table 1 and Table 2 show the refined parameters, refined cell and atomic parameters respectively. In the case of LSNAO_0.1 no additional reflections stemming from impurities are observed. On the other hand, in the case of LSNAO_0.2, a minor "$LaAlO_3$"-type oxide impurity was also included in the refinement and the impurity

contents (wt %) were determined directly from the Rietveld refinement obtaining a result of 2.91 (11) % weight per cent "$LaAlO_3$"-type oxide.

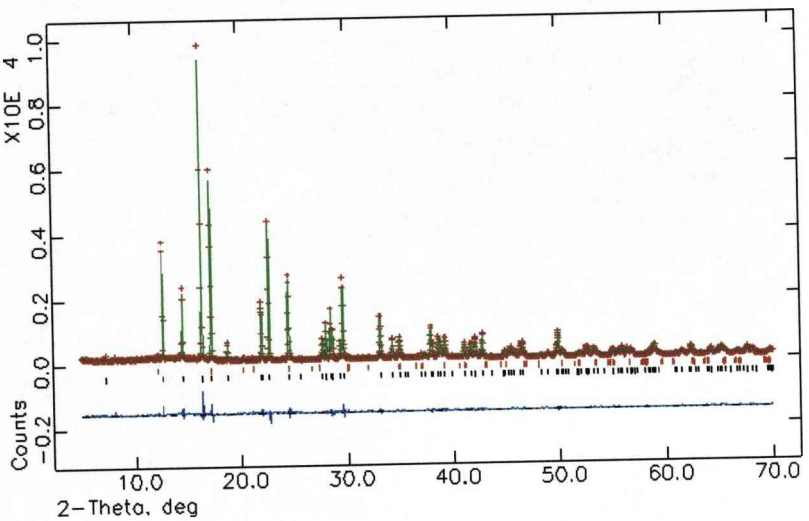

Figure 4. *Rietveld refinement of Synchrotron X-Ray of LSNAO_0.2. Crosses are observed data, the solid red line is the calculated pattern and the pink line is the difference. The upper set of tick marks correspond to the positions of the Bragg peaks for "$LaAlO_3$"-type oxide impurity and the lower ones correspond to the Bragg peaks for $La_{1.2}Sr_{0.8}Ni_{0.2}Al_{0.8}O_4$. The phase fraction for "$LaAlO_3$"-type oxide from the refinement is 2.91 (11) %.*

Table 1. *Refined parameters and refined cell constants for* $LaSrAlO_4$[7], $La_{1.1}Sr_{0.9}Ni_{0.1}Al_{0.9}O_4$ *(LSNAO_0.1) and* $La_{1.2}Sr_{0.8}Ni_{0.2}Al_{0.8}O_4$ *(LSNAO_0.2).*

	$LaSrAlO_4$[7]	LSNAO_0.1	LSNAO_0.2
wRp (%)	--	8.87	7.75
Rp (%)	--	7.02	6.7
χ^2	--	3.344	2.8
R_f^2 (%)	--	2.86	3.98
a / Å	3.7564	3.7670 (1)	3.7789 (1)
c / Å	12.6357	12.6505 (1)	12.6575 (1)
V / Å^3	178.3	179.513 (3)	180.745 (4)

Table 2. *Refined atomic parameters for both LSNAO_0.1 and LSNAO_0.2 oxides in the tetragonal I4/mmm space group.*

	LSNAO_0.1	LSNAO_0.2
La/Sr 1 *4e* (0 0 z)		
z	0.3592 (1)	0.3599 (1)
U	0.0061 (2)	0.0097 (1)
Al/Ni 1 *2a* (1/2 1/2 1/2)		
U	0.0041 (7)	0.0034 (3)
O 1 *4d* (1/2 0 1/2)		
U	0.0080 (13)	0.0144 (10)
O 2 *4e* (0 0 z)		
z	0.1640 (3)	0.1642 (3)
U	0.0191 (14)	0.0165 (10)

TGA experiments were carried out for both compositions under both oxidised and reduced atmospheres in order to establish if oxygen vacancies or interstitial oxygen were present in these materials. Both oxidation of Ni^{2+} to Ni^{3+} or reduction to Ni^{+} are possible which would create oxygen interstitial or oxygen vacancies respectively. Reduction is much less likely

though there are some examples[13] so the interest is to create interstitial oxygen. No significant weight loss or gain (0.15 % expected for full oxidation to Ni^{3+} and 0.02 % observed, which is close to the instrumental error +/- 0.02%) was observed.

The oxidation state appears to be close to +2 as confirmed by the XAS data (Figure 5) which shows nearly the same absorption edge energies (8345.1 eV for LSNAO_0.1 and 8345.5 eV for LSNAO_0.2) for both LSNAO materials (8345.1 eV and 8346.9 eV were observed for La_2NiO_4 and $LaSrNiO_4$ respectively).

The electrical conductivities of LSNAO_0.1 and LSNAO_0.2 were investigated by AC impedance spectroscopy and DC electrical conductivity measurements. Figure 6 and 7 show AC impedance spectroscopy measurements for LSNAO_0.1 and LSNAO_0.2 at 300 °C. In the case of the lower nickel content LSNAO_0.1, only one semicircle typical of an ionic conductivity contribution is observed. The capacitance values are also indicative of the bulk response (2.16×10^{-12} F/cm at $\nu = 10^6$ Hz) at high frequencies and grain boundary response (3.80×10^{-10} F/cm at $\nu = 1$ Hz) at low frequencies. LSNAO_0.2 is significantly more conducting. From the capacitance values, this conductivity can also be interpreted as a bulk response (5.43×10^{-12} F/cm at $\nu = 10^6$ Hz) at high frequencies and as a grain boundary response (1.04×10^{-8} F/cm at $\nu = 1$ Hz) at low frequencies. Due to the high conductivity of these materials AC impedance spectroscopy is not reliable at high temperature and thus duplicate DC measurements were carried out at high temperature.

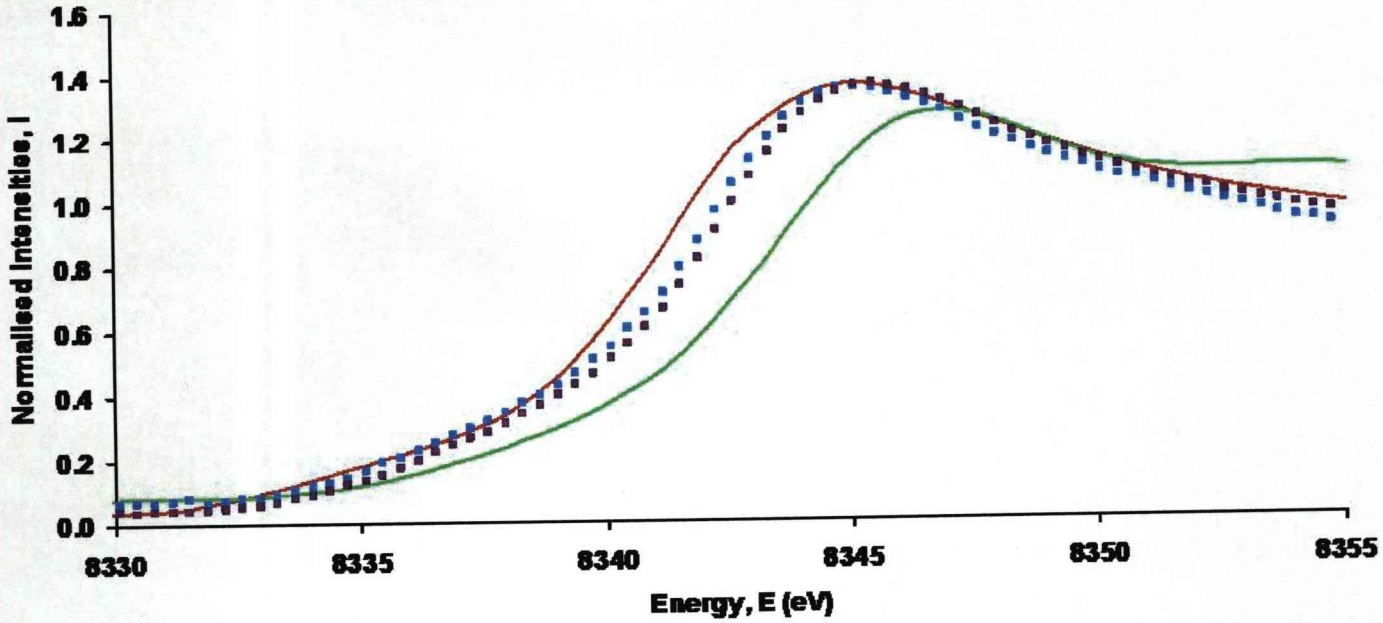

Figure 5. *X-ray absorption spectroscopy (XAS) data for LSNAO_0.1 (blue) and LSNAO_0.2 (violet) with La_2NiO_4 (red) and $LaSrNiO_4$ (green) as Ni^{2+} and Ni^{3+} standards respectively.*

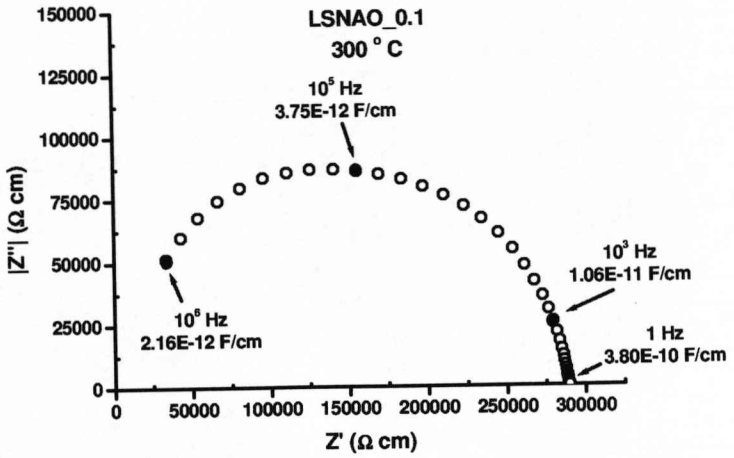

Figure 6. *Two-probe AC Impedance spectroscopy plot for LSNAO_0.1 material at 300 °C. The capacitances values for different frequencies are marked on the figure.*

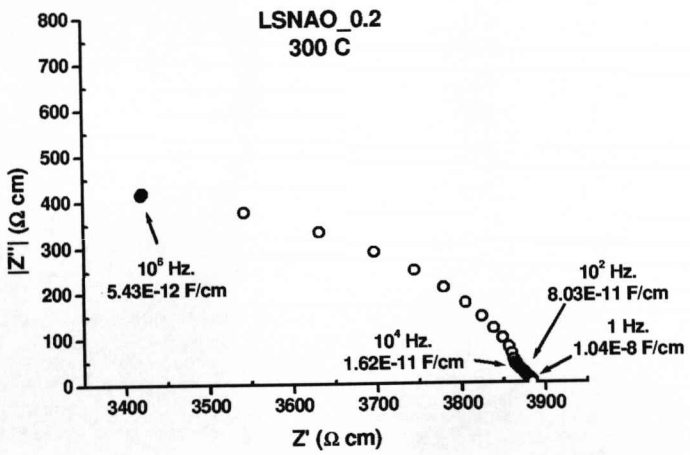

Figure 7. *Two-probe AC Impedance spectroscopy plot for LSNAO_0.2 material at 300 °C. The capacitances values for different frequencies are marked on the figure.*

Figure 8 shows a representation of the conductivity against the temperature. These data yield equivalent overall resistivities to Impedance Spectroscopy (IS) data. It can be seen how the conductivity increases with the temperature as a typical behaviour of a semiconductor material. It can also be observed that the conductivity increases with the level of nickel doping.

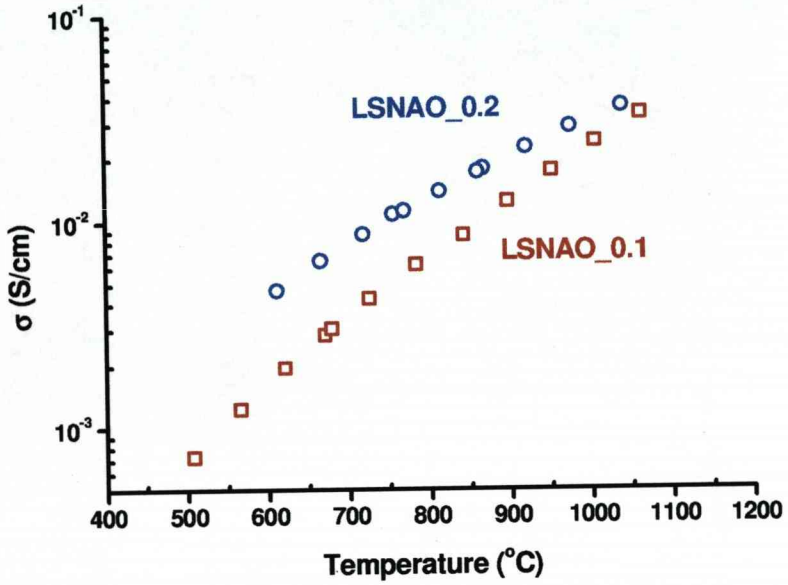

Figure 8. *Four-probe DC resistivity measurements for both LSNAO_0.1 and LSNAO_0.2 materials showing the increase of the conductivity as the temperature and level of nickel doping increases.*

7.4. Discussion.

The variations of the unit cell volume for LSNAO_0.1 and LSNAO_0.2 at RT are shown in Figure 9 and compared with the undoped material. It can be seen that both the unit cell volume and *a* and *c* parameters increase steadily with increasing Ni content. This data confirms the introduction of nickel species and the substitution of Ni^{2+} for Al^{3+} due to the larger ionic radius of Ni^{2+} (0.69 Å) in comparison with Al^{3+} (0.53 Å).

Table 3 shows the refined bond lengths and calculated bond valence sums for LSNAO_0.1 and LSNAO_0.2. It can be seen how the distances Sr-O, La-O, Ni-O and Al-O increases as the level of nickel increases.

It could be expected that we could have a level of oxidation in the Ni similar to the one found in the case of the well-known solid oxide fuel cell compound $La_2NiO_{4+\delta}$ where a oxidation state for the nickel close to 2.3 (30 % of Ni^{3+} and 70 % of Ni^{2+}) is observed . It can be seen from the bond valences sums how there are significant local distortions, therefore in the average structure the aluminium is underbonded and the nickel is overbonded as the XAS data show that the nickel is close to 2+ though possibly slightly shifted. These data are consistent with the absence of excess oxygen found by the TGA measurements. We can therefore conclude that the Nickel oxidation state is close to 2 and the oxygen stoichiometry close to 4 for both materials.

a

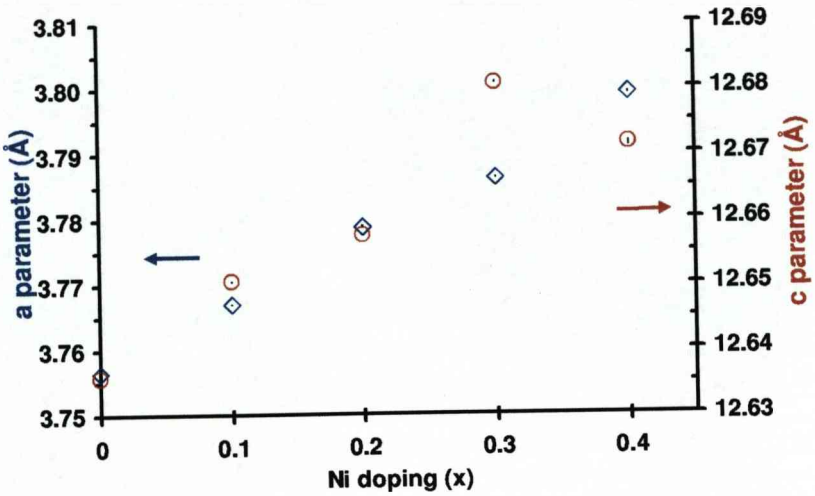

b

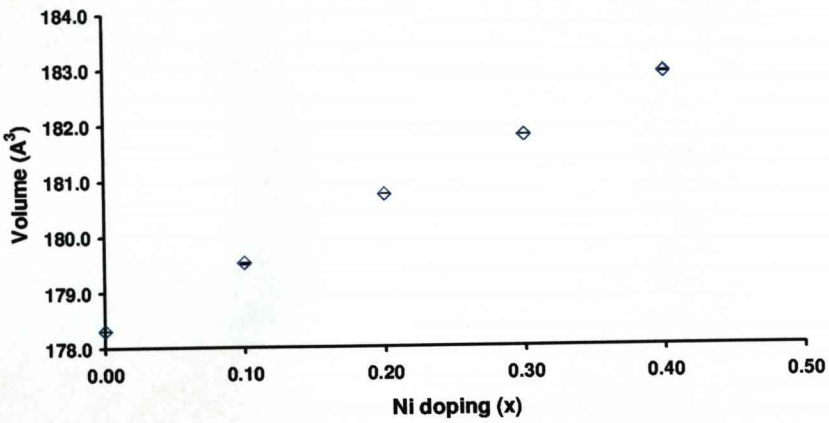

Figure 9. *Lattice parameters (a) and unit cell volume (b) versus nickel doping for* $La_{1+x}Sr_{1-x}Ni_xAl_{1-x}O_4$

Table 3. *Refined bond lengths and calculated bond valence sums for both LSNAO_0.1 and LSNAO_0.2.*

Bond (Å)	LSNAO_0.1	LSNAO_0.2
Sr-O1 x 4	2.5921 (5)	2.5915 (4)
Sr-O2 x 4	2.6791 (4)	2.6893 (5)
Sr-O2 x 4	2.47 (5)	2.477 (4)
La-O1 x 4	2.5921 (5)	2.5915 (4)
La-O2 x 4	2.6791 (4)	2.6893 (5)
La-O2 x 4	2.471 (50)	2.477 (4)
Al1-O1 x 4	1.8831 (1)	1.8894 (1)
Al1-O2 x 2	2.075 (4)	2.0780 (4)
Ni-O1 x 4	1.8831 (1)	1.8894 (1)
Ni-O2 x 2	2.0751 (4)	2.0780 (4)
Sr BVS	2.37 (2)	2.35 (2)
La BVS	2.75 (2)	2.71 (2)
Al BVS	2.55 (1)	2.51 (1)
Ni BVS	2.79 (1)	2.75 (1)

Both LSNAO materials were studied by AC impedance spectroscopy and DC resistivity measurements in order to characterize their physical properties. It was found from the four-probe DC conductivity measurements (Figure 8) that these materials are moderate electric conductors (6.18×10^{-3} S/cm LSNAO_0.1 at 783 °C and 1.08×10^{-2} S/cm for LSNAO_0.2 at 813 °C) and the introduction of Ni in the $LaSrAlO_4$ structure increases its conductivity.

From the data given above it appears that the conductivity is mainly electronic and that very little ionic conductivity has been introduced. Figure

10 and Figure 11 show log conductivity versus the inverse of the temperature for both materials. The activation energy can be calculated from the DC measurement data using the Arrhenius equation (1):

$$Log\sigma = A - \frac{E_a}{kT}$$ where k is the Boltzman constant. (1)

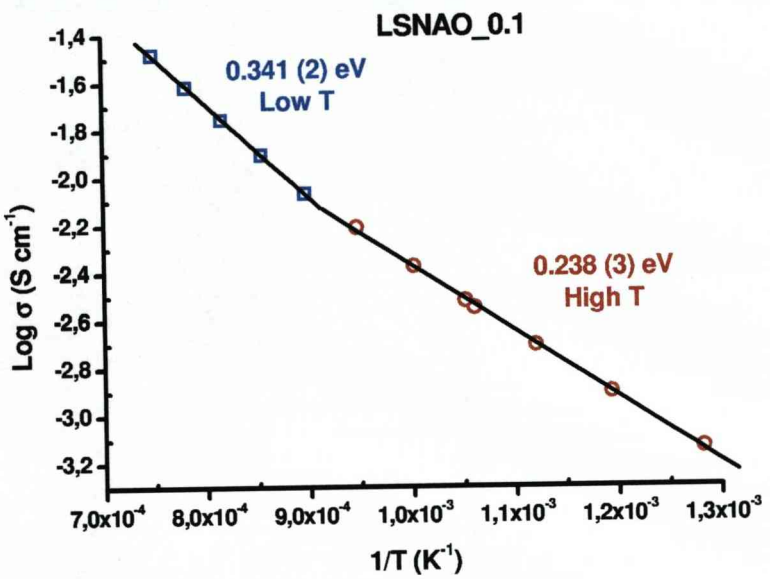

Figure 10. *Logarithm of the conductivity versus the inverse of the temperature for LSNAO_0.1.*

In both cases two different slopes were observed, at high temperature and at low temperature. The values of activation energy are 0.341(2) eV at low T and 0.238(3) eV at high T for LSNAO_0.1 and 0.222(2) eV at low T and 0.198(6) eV at high T for LSNAO_0.2. These

values are lower than would be expected for a typical ionic conductor. Given the lack of evidence for oxygen nonstoichiometry it's reasonable to assume that the conductivity observed is dominated by the electrical contribution due to the nature of the nickel.

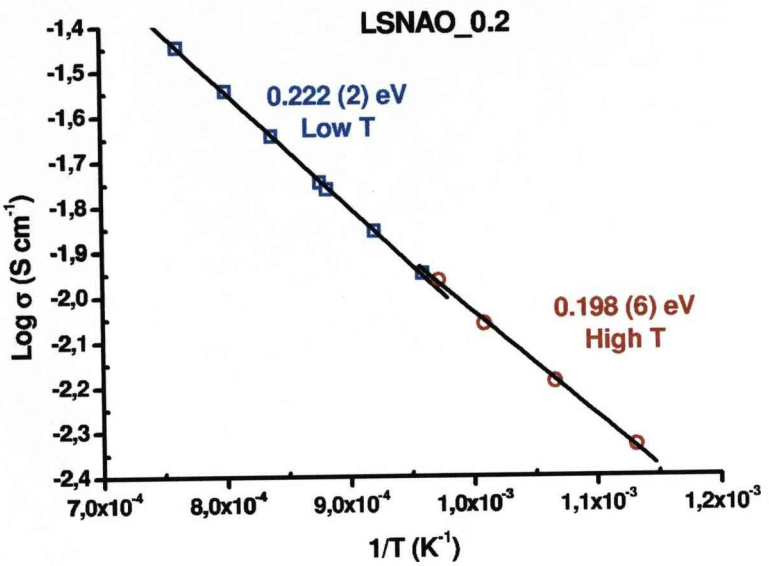

Figure 11. *Logarithm of the conductivity versus the inverse of the temperature for LSNAO_0.2.*

7.5. Conclusions.

Doping in the system $La_{1+x}Sr_{1-x}B_xAl_{1-x}O_4$ (B = Ni^{2+}, Co^{3+}, Ti^{4+}) for values $0 \leq x \leq 0.4$ was studied in air. Two compositions were successfully synthesized and characterised, $La_{1.1}Sr_{0.9}Ni_{0.1}Al_{0.9}O_4$ and $La_{1.2}Sr_{0.8}Ni_{0.2}Al_{0.8}O_4$. Synthesis of compounds with different cation such as Co or Ti and larger values of x, in the case of the Ni did not succeed. The materials adopt a tetragonal structure in the space group I4/mmm typical of the Ruddlesden-Popper family compounds. It has also been shown that these compounds do not present any significant value of interstitial oxygen or oxygen vacancies.

These materials show a significant increase in the electric conductivity in comparison with the parent material. This electrical conductivity behaviour is due to the nickel. AC impedance spectroscopy and DC resistivity measurements on both LSNAO_0.1 and LSNAO_0.2 are consistent with the materials being electric conductors without any significant ionic contribution.

7.6. References.

(1) Ruddlesden, S. N.; Popper, P. *Acta Crystallogr.* **1957**, *10*, 538-540.

(2) Ruddlesden, S. N.; Popper, P. *Acta Crystallogr.* **1958**, *11*, 54-55.

(3) Shannon, R. D.; Oswald, R. A.; Parise, J. B.; Chai, B. H. T.; Byszewski, P.; Pajaczkowska, A.; Sobolewski, R. *J. Solid St. Chem.* **1992**, *98*, 90-98.

(4) Raj, E. S.; Skinner, S. J.; Kilner, J. A. *Solid State Sci.* **2004**, *6*, 825-829.

(5) Magrez, A.; Cochet, M.; Joubert, O.; Louarn, G.; Ganne, M.; Chauvet, O. *Chem. Mater.* **2001**, *13*, 3893-3898.

(6) Magrez, A.; Caldes, M.; Joubert, O.; Ganne, M. *Solid State Ionics* **2002**, *151*, 365-370.

(7) Magrez, A.; Morniroli, J. P.; Caldes, M. T.; Marie, A. M.; Joubert, O.; Brohan, L. *J. Solid St. Chem.* **2003**, *172*, 243-251.

(8) Mogni, L.; Prado, F.; Caneiro, A.; Manthiram, A. *Solid State Ionics* **2006**, *177*, 1807-1810.

(9) Amow, G.; Au, J.; Davidson, I. *Solid State Ionics* **2006**, *177*, 1837-1841.

(10) Amow, G.; Davidson, I. J.; Skinner, S. J. *Solid State Ionics* **2006**, *177*, 1205-1210.

(11) Aguadero, A.; Alonso, J. A.; Martinez-Lope, M. J.; Fernandez-Diaz, M. T.; Escudero, M. J.; Daza, L. *J. Mater. Chem.* **2006**, *16*, 3402-3408.

(12) Park, J. Y.; Choi, G. M. *Solid State Ionics* **2002**, *154*, 535-540.

(13) Crespin, M.; Landron, C.; Odier, P.; Bassat, J. M.; Mouron, P.; Choisnet, J. *J. Solid St. Chem.* **1992**, *100*, 281-91.

Chapter 8:

$Bi_8Cr_7O_{22.5}$ and

$Bi_{17}Cr_8Sr_7O_{44.5}$: Complex intergrowths derived from fluorite

8.1. Introduction.

Many compounds adopting the fluorite-type structure have been reported as promising ionic conductors and as potential anodes for solid oxide fuel cells. Amongst these doped-Bi_2O_3 oxides such as $Bi_4Ln_2O_9$ (Ln = La,Pr,Nd)[1], $Bi_{18-4m}M_{4m}O_{27+4m}$ (M = P, V)[2,3], $Bi_{0.775}La_{0.225}O_{1.5}$[4], $Bi_{2n+4}Mo_nO_{6(n+1)}$ (n = 3, 4, 5, 6)[5], $(Bi_2O_3)_{1-x}(WO_3)_x$[6] or $Bi_{0.45}Sr_{2.5}Cr_{1.05}O_{4.95}$[7] have been reported to have promising properties.

Both the Bi-Cr-O and Bi-Cr-Sr-O systems have been previously studied[8,9] and the properties of several compositions reported[7,10-12]. Several

compounds in the pseudo binary system Bi_2O_3-Cr_2O_3 have also been reported as good ionic conductors $Bi_{1-x}Cr_xO_{1.5+1.5x}$ $(0.05 \leq x \leq 0.15)$[13], $Bi_{14}CrO_{24}$[14], Bi_8CrO_{15}[15] and $Bi_6Cr_2O_{15}$[16]. Figure 1 shows the pseudo binary phase diagram in the system reported by Masuno et al[9].

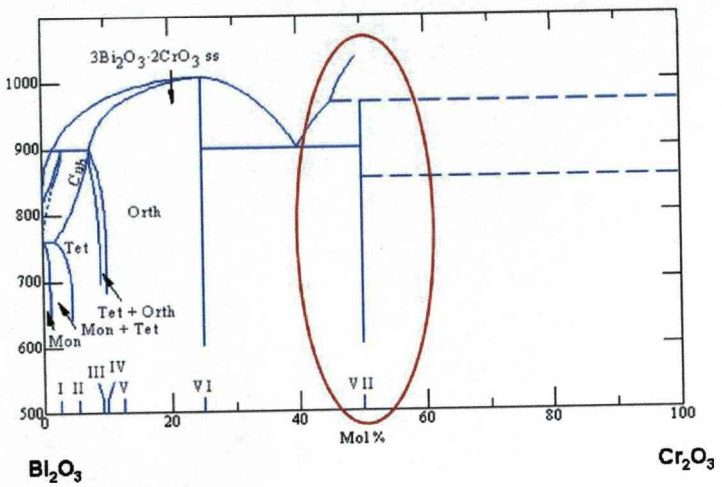

Figure 1. *Pseudo binary phase diagram in the Bi_2O_3-Cr_2O_3 system reported by Masuno et al[9]. The highlighted area is the subject of the current study.*

In this chapter, an investigation in the ternary Bi_2O_3-Cr_2O_3-SrO system will be presented.

8.2. Experimental.

$Bi_8Cr_7O_{22.5}$ and $Bi_{17}Cr_8Sr_7O_{44.5}$ materials were prepared by direct reaction of Bi_2O_3, SrO and Cr_2O_3 in stoichiometric quantities respectively. SrO was prepared by heating SrO_2 to 1100 °C for 24 h and was transferred

whilst still incandescent into a glove box under an inert atmosphere to avoid reaction with atmospheric carbon dioxide and water. The powders were then pressed into bars and placed in silica tube. The tubes were then sealed under 10^{-4} torr. vacuum and heated to 800 °C for 12 h. Heating and cooling to room temperature were performed over a period of 6 h.

Samples for physical measurements were ground again and uniaxilly pressed into pellets and bars at a pressure of 300 MPa. The relative densities of the pellets and bars were calculated from the dimensions and weight of the samples. Densities of 70-75 % were obtained for the material.

Other experimental information can be found in chapter 2.

8.3. Results and discussion.

Several syntheses in the Bi_2O_3-Cr_2O_3 system were attempted with a starting Bi/Cr cation ratio close to 1. Powder X-ray diffraction indicated that a single phase was obtained starting with a nominal composition of $Bi_{0.55}Cr_{0.45}O_{1.5}$. EDS analysis confirmed the cation ratio and the homogeneity of the sample. Electron Diffraction (ED) patterns recorded for the $Bi_{0.55}Cr_{0.45}O_{1.5}$ (equivalent to $Bi_8Cr_7O_{22.5}$) exhibit streaking and diffuse features along the c axes which could indicate the presence of defects or disorder in the structure (Figure 2). The ED patterns could be indexed based on an R centred hexagonal cell lattice parameters a ~ 7.5 Å, c ~ 28 Å omitting the diffuse features.

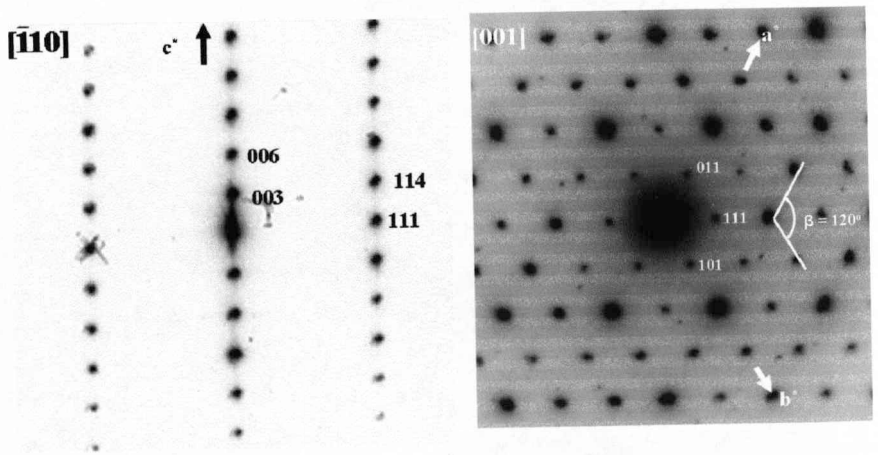

Figure 2. *Selected ED patterns for $Bi_8Cr_7O_{22.5}$ oxide for the [$\bar{1}$10] (left) and [001] (right) projections. Streaking and diffuse features along the c^* is clearly visible on the left*

At this point, a close correspondence with $Bi_{0.78}Sr_{0.4}RhO_3$[17] was noted which has been described in a similar hexagonal cell. Figure 3 shows powder X-Ray diffraction pattern for superimposition on the peak position for an $R\bar{3}$ cell derived from ED. It can be seen that this accounts for the sharp reflections but does not explain several broad peaks presents in the powder X-Ray diffraction pattern. LeBail fits for the $R\bar{3}$ cell did not account for some weak peaks as well as the diffuse feature indicating that the compound adopts a structure of lower symmetry though attempts to index these proved unsatisfactory due to the difficulty in assigning the number of peaks under the broad features.

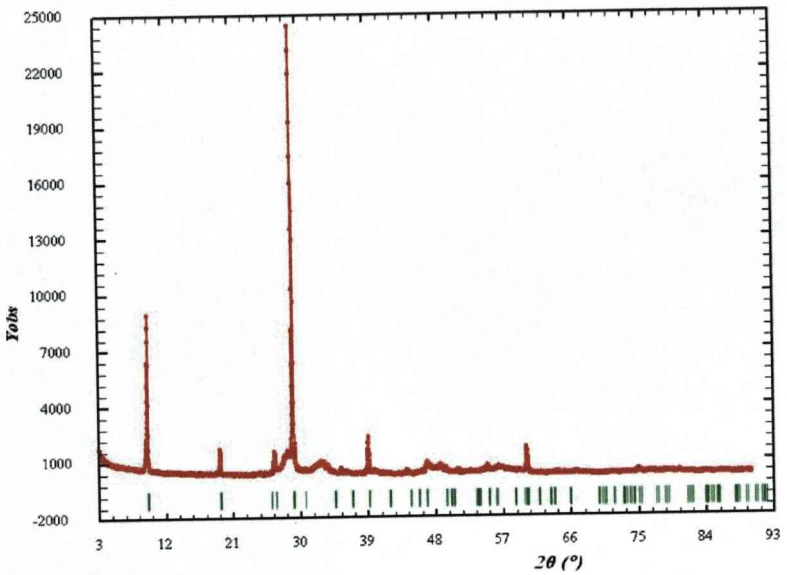

Figure 3. *Powder X-Ray diffraction pattern for $Bi_8Cr_7O_{22.5}$.Tick marks show the location peaks for an* $R\bar{3}$ *cell a = b = 7.77181 (381) Å, c = 27.70304 (75) Å.*

One possible origin of these peaks might be impurity phases or complex micro structural effects such as Cr_2O_3 or Bi_2O_3 intergrowths. The possible presence of such impurities and intergrowths was discounted after EDS of approximately 50 crystallites revealed no such crystallites or secondary phases indicating that the material is compositionally homogenous. Prolonged annealing did not lead to the sharpening of these peaks.

Due to the inability to improve the quality of $Bi_{0.55}Cr_{0.45}O_{1.5}$, the Bi-Cr-Sr-O system was investigated in parallel and its analogy with the compound $Bi_{0.78}Sr_{0.4}RhO_3$ mentioned previously. Several synthesis were attempted and EDS showed that a main phase of composition

$Bi_{0.55}Cr_{0.25}Sr_{0.20}O_{1.4}$ was present, however it could not be obtained as a pure phase with $Bi_{0.55}Cr_{0.45}O_{1.5}$ always present as secondary phase.

Figure 4 shows the powder X-Ray diffraction for the sample with the greatest content of $Bi_{0.55}Cr_{0.25}Sr_{0.20}O_{1.4}$. Figure 5 shows a comparison of the powder X-ray diffraction patterns for $Bi_{0.55}Cr_{0.25}Sr_{0.20}O_{1.4}$ and $Bi_{0.55}Cr_{0.45}O_{1.5}$ given the significant overlap and width of the $Bi_{0.55}Cr_{0.25}Sr_{0.20}O_{1.4}$ peaks it was not possible to index the pattern. In this chapter we have been focused on the structural features of $Bi_8Cr_7O_{22.5}$. The structural features of this $Bi_{0.55}Cr_{0.25}Sr_{0.20}O_{1.4}$ oxide will be investigated in a future work.

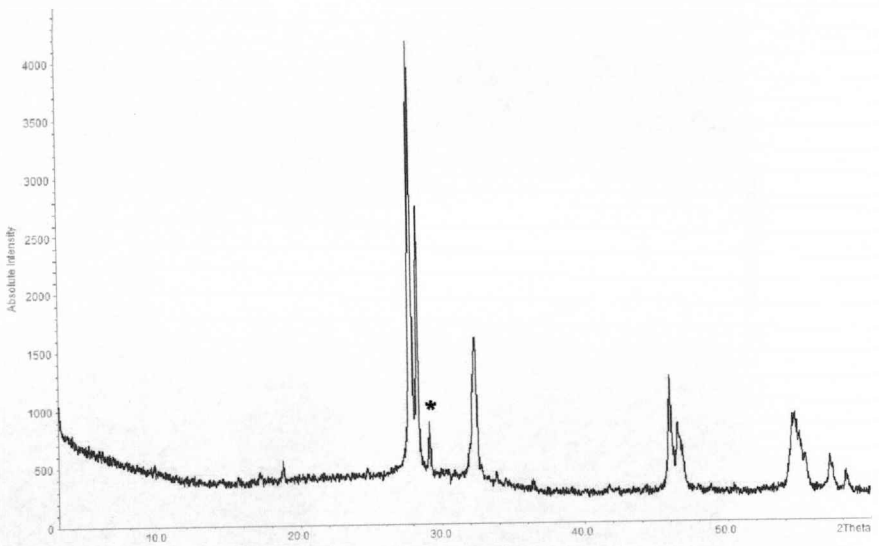

Figure 4. *Powder X-Ray diffraction pattern of* $Bi_{0.55}Cr_{0.25}Sr_{0.20}O_{1.4}$. *The asterisk marks the strongest reflection due to the* $Bi_{0.55}Cr_{0.45}O_{1.5}$ *impurity.*

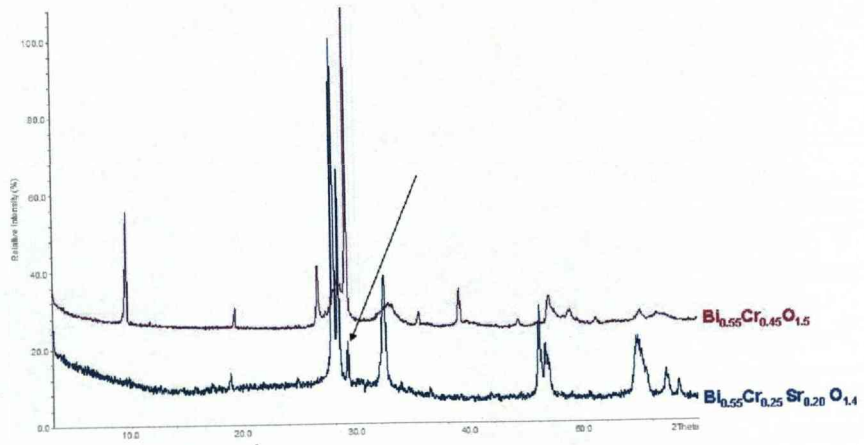

Figure 5. *Powder X-Ray diffraction patterns of both* $Bi_{0.55}Cr_{0.45}O_{1.5}$ *and* $Bi_{0.55}Cr_{0.25}Sr_{0.20}O_{1.4}$. *The arrow indicates the strongest common reflection.*

$Bi_8Cr_7O_{22.5}$ was examined by High Resolution Electron Microscopy studies in order to try and better understand its structure. Figure 6 shows an image where two different domains, which is consistent with the stacking features observed in the ED patterns can be observed. Similar domain boundaries are commonly observed and could partially explain the difficulties in interpreting the diffraction results.

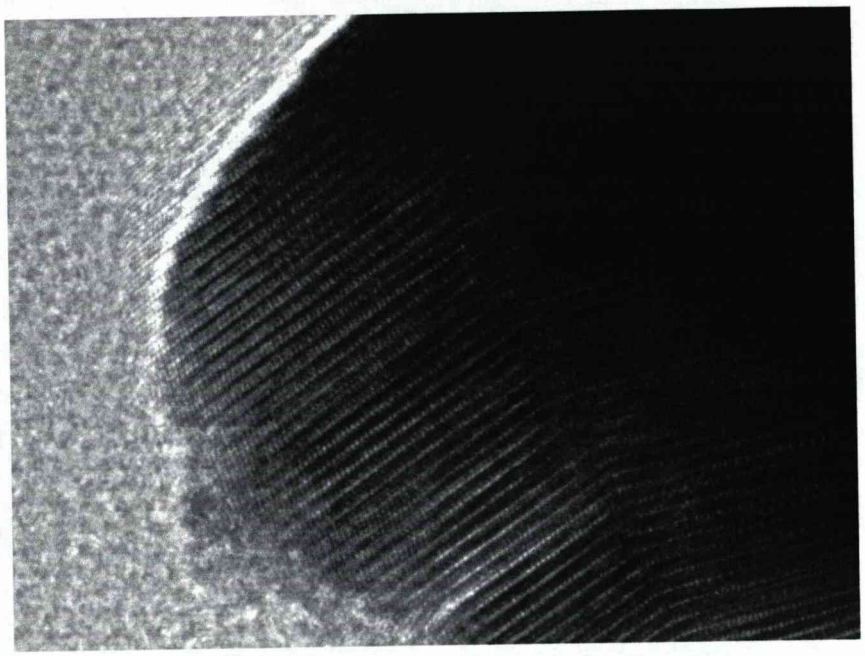

Figure 6. *High Resolution Electron Microscopy (HREM) images for the* $Bi_8Cr_7O_{22.5}$ *oxide showing different domains present in the structure.*

Figure 7 shows another HREM image which contains a significant number of defects. These defects could also contribute to the broad reflections observed by powder X-Ray diffraction. One structural model that at least can act as a model for the observed contrast is the presence of complex intergrowth between the bismuth based fluorite-type structural blocks and a chromium based CdI_2-type layer as it was reported in the case of $Bi_{0.78}Sr_{0.4}RhO_3$ by Kobayashi et al.[17]. This chromium based CdI_2-type layer would be the dark lines of contrast in Figure 7. Figure 8 shows a schematic drawing of the idealised structural model. Any final model would need to take into account the overall oxygen stoichiometry.

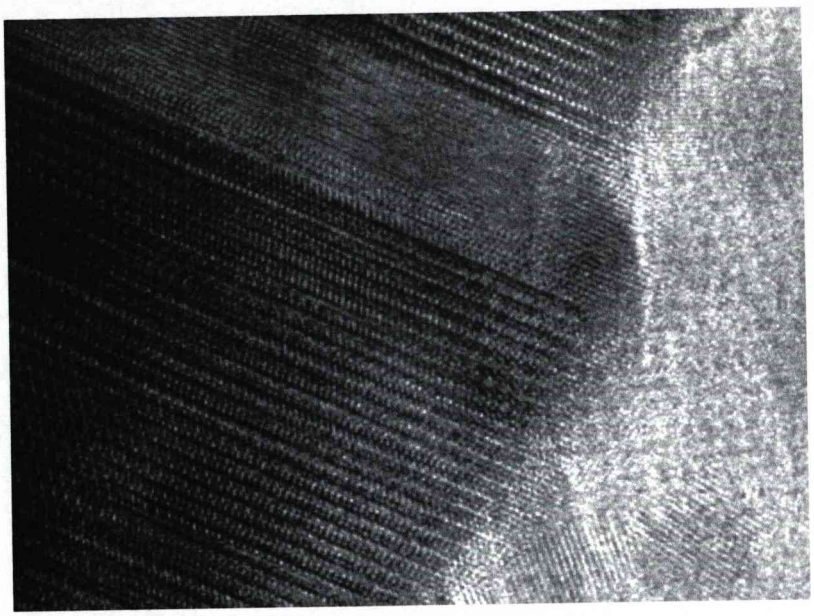

Figure 7. *High Resolution Electron Microscopy (HREM) images for the* $Bi_8Cr_7O_{22.5}$ *oxide showing different numerous defects present in the structure.*

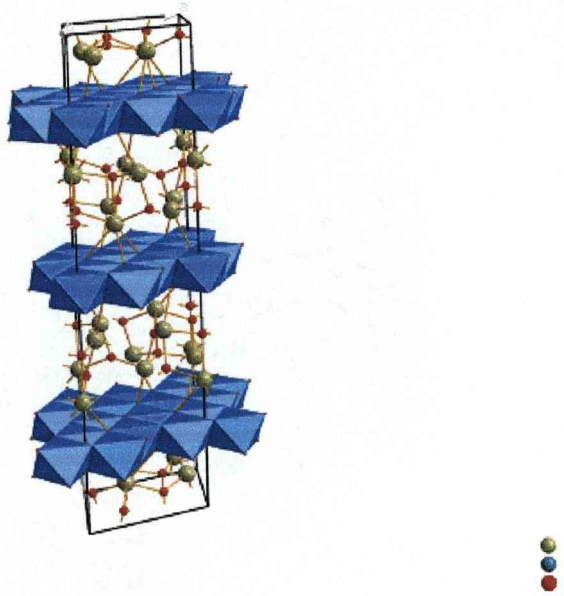

Figure 8. *Structural model for $Bi_8Cr_7O_{22.5}$. It is made up of chromium based CdI_2-type layers in blue and the Bi_2O_3 fluorite-type layer between them.*

AC Impedance Spectroscopy measurements were carried out for both $Bi_8Cr_7O_{22.5}$ and $Bi_{17}Cr_8Sr_7O_{44.5}$ oxides in order to investigate their conductivity.

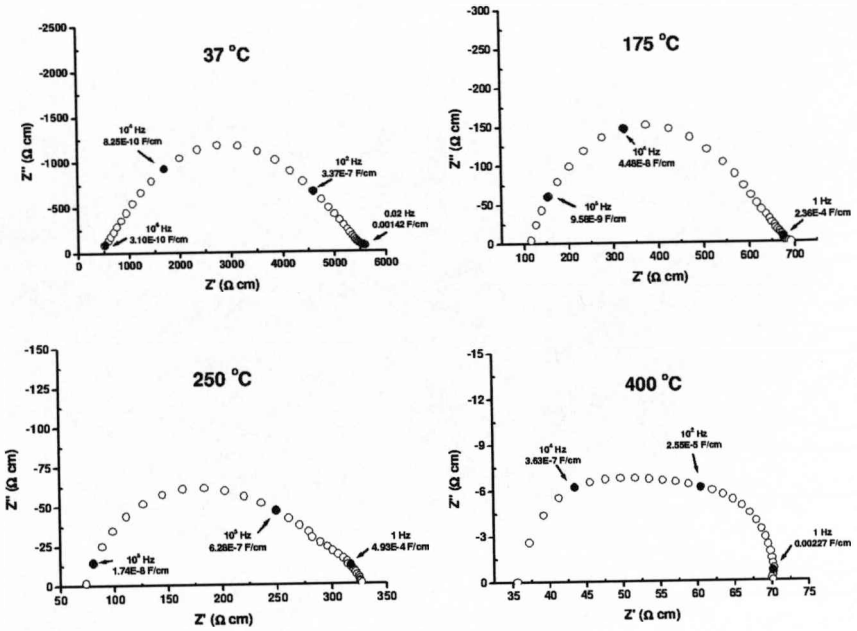

Figure 9. *AC Impedance Spectroscopy plots for the $Bi_8Cr_7O_{22}$ oxide at 37 °C, 175 °C, 250 °C and 400 °C.*

Figure 9 shows the impedance spectroscopy plots for $Bi_8Cr_7O_{22}$ compound at various temperatures. The compound shows only a very small ionic contribution to the overall conductivity observed as a single semicircle. At all the temperatures measured the observed conductivity was dominated for the electronic contribution to the overall conductivity as described in section 2.5.1. The observed response is mainly due to the grain boundary response due to the observed capacitance values (1.74×10^{-8} F/cm at 250 °C). The higher capacitance values observed at low frequencies are due to electrode effects.

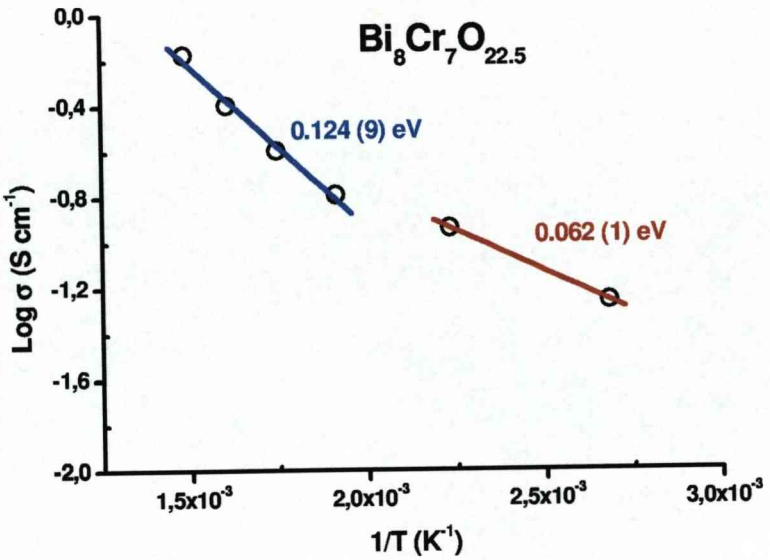

Figure 10. *Arrhenius plot for the $Bi_8Cr_7O_{22.5}$.*

Figure 10 shows an activation energy plot for the total conductivity measured at low frequency (1 Hz). It can be seen that the activation energy at high temperature is 0.124 (9) eV which is lower than expected for ionic conductors. The conductivity of this compound is 0.162 S cm^{-1} at 250 °C.

Figure 11 shows the AC Impedance Spectroscopy plots for $Bi_{17}Cr_8Sr_7O_{44}$ as a function of temperature. The observed semicircles are due to the grain boundary response given the capacitance values (3.32 x 10^{-9} F/cm at 453 °C). As in the case of the $Bi_8Cr_7O_{22}$ oxide, the electrode response can be seen at lower frequencies with larger capacitance values (2.48 x 10^{-5} F/cm at 473 °C).

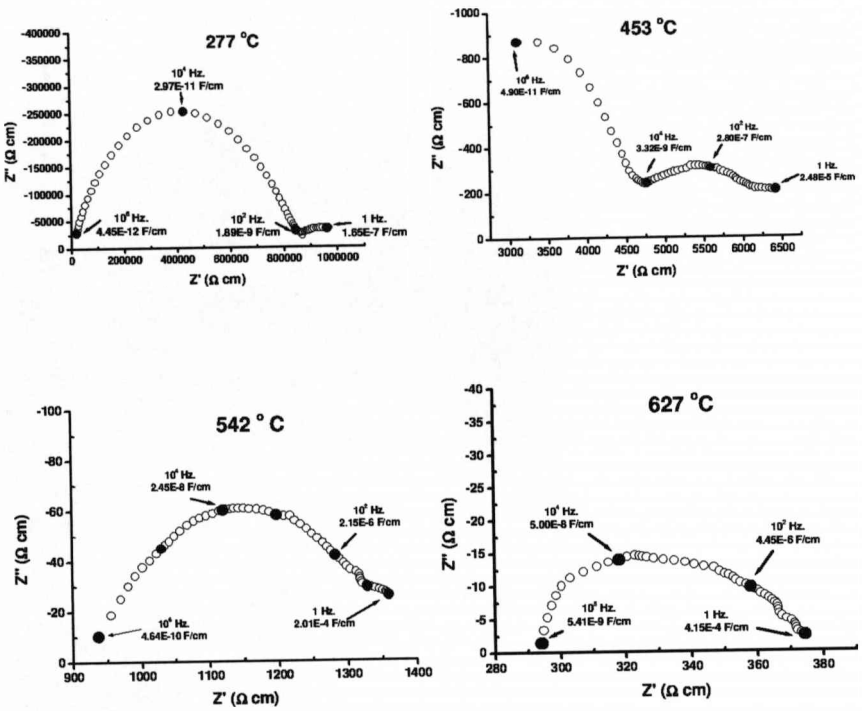

Figure 11. *AC Impedance Spectroscopy plots for $Bi_{17}Cr_8Sr_7O_{44.5}$ at 277 °C, 453 °C, 542 °C and 627 °C.*

Figure 13 shows an Arrhenius plot for the total conductivity taken at 1 Hz for the $Bi_{17}Cr_8Sr_7O_{44.5}$. It can be seen from the activation energy (0.490 (39) eV) that is considerably higher than in $Bi_8Cr_7O_{22.5}$ and are close to those expected for ionic conductors, however further measurements of transport number would be required to confirm whether this is ionic conductivity.

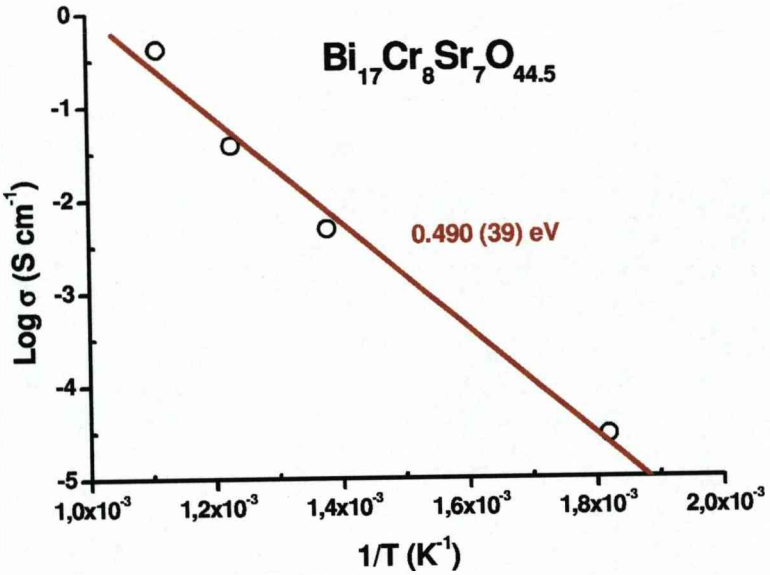

Figure 12. *Arrhenius plot for* $Bi_{17}Cr_8Sr_7O_{44.5}$

8.4. Conclusions.

In this chapter, we have investigated both Bi-Cr-O and Bi-Cr-Sr-O systems in an attempt to find new mixed conducting oxides. Two new compositions were isolated: $Bi_8Cr_7O_{22.5}$ and $Bi_{17}Cr_8Sr_7O_{44.5}$. The former appears to be best described as a fluorite-type structure with numerous defects. These defects are only poorly ordered leading to diffuse features in both the electron diffraction and powder X-Ray diffraction. Currently it is suggested that the structure is an intergrowth between the fluorite-type

layers and the CdI_2-type layers which is consistent with the observed micrographs.

The electrical conductivity of both compounds was determined by AC Impedance Spectroscopy. For $Bi_8Cr_7O_{22}$ the electronic contribution dominates in the overall conductivity. $Bi_{17}Cr_8Sr_7O_{44}$ is much less conducting and may show significant oxide ion conductivity At higher temperatures the conductivity is dominated by the electronic contribution to the overall conductivity.

8.5. References.

(1) Drache, M.; Huve, M.; Roussel, P.; Conflant, P. *Mater. Res. Bull.* **2003**, *38*, 113-124.

(2) Mauvy, F.; Launay, J. C.; Darriet, J. *J. Solid St. Chem.* **2005**, *178*, 2015-2023.

(3) Darriet, J.; Launay, J. C.; Zuniga, F. J. *J. Solid St. Chem.* **2005**, *178*, 1753-1764.

(4) Ahi, A.; Mellerga?rd, A.; Eriksson, S. G. *Solid State Ionics* **2006**, *177*, 289-297.

(5) Vila, E.; Landa-Canovas, A. R.; Galy, J.; Iglesias, J. E.; Castro, A. *J. Solid St. Chem.* **2007**, *180*, 661-669.

(6) Takahashi, T.; Iwahara, H. *J. Appl. Electrochem.* **1973**, *3*, 65-72.

(7) Allix, M.; Pelloquin, D.; Studer, F.; Nguyen, N.; Wahl, A.; Maignan, A.; Raveau, B. *J. Solid St. Chem.* **2002**, *167*, 48-58.

(8) Vstavskaya, E. Y.; Zuev, A. Y.; Cherepanov, V. A.; Sutton, S. D.; Abell, J. S. *J. Phase Equilib.* **1994**, *15*, 573-576.

(9) Masuno, K. *J. Chem. Soc. Jpn.* **1969**, *90*, 1122-1127.

(10) Be?gue, P.; Rojo, J. M.; Iglesias, J. E.; Castro, A. *J. Solid St. Chem.* **2002**, *166*, 7-14.

(11) Pelloquin, D.; Wahl, A.; Masset, A. C.; Maignan, A.; Michel, C.; Raveau, B. *J. Solid St. Chem.* **2000**, *154*, 375-383.

(12) Mercurio, D.; Champarnaud-Mesjard, J. C.; Frit, B.; Conflant, P.; Boivin, J. C.; Vogt, T. *J. Solid St. Chem.* **1994**, *112*, 1-8.

(13) Esmaeilzadeh, S.; Lundgren, S.; Ha?lenius, U.; Grins, J. *J. Solid St. Chem.* **2001**, *156*, 168-180.

(14) Warda, S. A.; Pietzuch, W.; Massa, W.; Kesper, U.; Reinen, D. *J. Solid St. Chem.* **2000**, *149*, 209-217.

(15) Kumada, N.; Takei, T.; Kinomura, N.; Wallez, G. *J. Solid St. Chem.* **2006**, *179*, 793-799.

(16) Grins, J.; Esmaeilzadeh, S.; Hull, S. *J. Solid St. Chem.* **2002**, *163*, 144-150.

(17) Kobayashi, W.; Hebert, S.; Pelloquin, D.; Perez, O.; Maignan, A. *Phys. Rev. B* **2007**, *76*.

Chapter 9:

General Conclusions and Perspectives

Solid oxide fuel cells (SOFC) have been the subject of considerable amounts of research in the past few years. Solid State Chemistry plays an important role in developing materials for uses as cathode and anodes. In this thesis, the synthesis, structural and physical characterisation of new mixed conducting oxides which could be used as cathodes or anodes for solid oxide fuel cells have been presented.

In Chapter 1 a general introduction to solid oxide fuel cells was presented, including the potential application of solid oxide fuel cells and some structural considerations. Chapter 2 presented the experimental techniques used during this thesis.

The bulk of the thesis describes investigations of several molybdenum containing compounds. Chapter 3 showed that $Sr_2MgMoO_{6-\delta}$ adopts a $\sqrt{2}\ a_p \times \sqrt{2}\ a_p \times 2\ a_p\ I\bar{1}$ superstructure of the simple perovskite cell, derived from an $a^0a^0c^-$ tilt system via distortion of the Mg- and Mo-centred octahedra. It was also shown that the reduction of $Sr_2MgMoO_{6-\delta}$ appears to be correlated with antisite disorder at either point or extended

anti-phase defects. The degree of reduction is small at temperatures below 900 °C. Upon further reduction above 900 °C, $Sr_2MgMoO_{6-\delta}$ begins to decompose into $Sr_{2.75}Mg_{0.5}Mo_{1.5}O_{7-\delta}$ an n = 2 R-P phase and MgO, and Mo materials. TEM analysis are consistent with the reduced material which is a complex intergrowth since the main phase obtained, $Sr_{2.75}Mg_{0.5}Mo_{1.5}O_{7-\delta}$ seems always to be intergrown with the perovskite starting $Sr_2MgMoO_{6-\delta}$ structure.

Chapter 4 presented the high temperature structural behaviour of $Sr_2MgMoO_{6-\delta}$ with a phase transition at 200-300 °C from triclinic ($I\bar{1}$) to cubic ($Fm\bar{3}m$).

Chapter 5 presented the attempted synthesis the R-P n = 2 phase of general formula $Sr_3(Mg_xMo_{1-x})_2O_{7-\delta}$ which had appeared as an impurity phase in the study of the double perovskite $Sr_2MgMoO_{6-\delta}$. It was shown a majority phase identified as a n = 2 R-P phase of formula $Sr_3Mg_{0.5}Mo_{1.5}O_{7-\delta}$ however impurities phases were always present and these were identified as $Sr_2MgMoO_{6-\delta}$ and the pseudo-perovskite $Sr_{11}Mo_4O_{23}$. TEM investigations showed the presence of numerous defects in the n = 2 R-P phase matrix which can be identified as n = 1 R-P type or $Sr_2MgMoO_{6-\delta}$ defects. It seems difficult to obtain a single phase without the formation of this complex intergrowth.

Chapter 6 presented that $Sr_{11}Mo_4O_{23}$ initially reported as Sr_3MoO_6 has been isolated and reported as a new pseudo-perovskite type structure phase which adopts a complex structure at ambient temperature. This structure seems to adopt a complex triclinic cell with the $P\bar{1}$ space group but HREM images evidence numerous defects and twining phenomena

which highlight the complexity of this structure. It undergoes a structural transition at 600 °C to a simpler structure. This high temperature form can be refined in a cubic $Fd\bar{3}m$ space group with a = 16.5571 (1) Å as cell parameter. $Sr_{11}Mo_4O_{23}$ was also described as a mixed conductor over the 500-600 °C temperature range, affording an oxide ion conductivity of 10^{-3} S cm^{-1}. Investigations about the structure of this material at RT are still ongoing.

The final two experimental chapters describe work on other systems as potential mixed conductors. Chapter 7 described investigations carried out in the system $La_{1+x}Sr_{1-x}B_xAl_{1-x}O_4$ ($B = Ni^{2+}$, Co^{3+}, Ti^{4+}) for values $0 \leq x \leq 0.4$. $La_{1.1}Sr_{0.9}Ni_{0.1}Al_{0.9}O_4$ (LSNAO_0.1) and $La_{1.2}Sr_{0.8}Ni_{0.2}Al_{0.8}O_4$ (LSNAO_0.2) oxides were successfully synthesized and characterised. These materials adopt a tetragonal structure in the I4/mmm space group and they do not present any significant value of interstitial oxygen or oxygen vacancies. These compounds showed a significant increase in the electric conductivity in comparison with the parent material. This electrical conductor behaviour is due to the nickel. Both LSNAO_0.1 and LSNAO_0.2 materials were characterised as electric conductors without any or very low ionic contribution.

Chapter 8 presented the synthesis of both $Bi_8Cr_7O_{22.5}$ and $Bi_{17}Cr_8Sr_7O_{44.5}$ compounds. These compounds can be described as a complex intergrowth derivated to the fluorite-type structure with numerous stacking defects. In the case of the $Bi_8Cr_7O_{22.5}$ oxide, it was shown that the electrical contribution domains in the overall conductivity (0.162 S cm^{-1} at 250 °C). For the $Bi_{17}Cr_8Sr_7O_{44.5}$ oxide presents a small ionic contribution to

the overall conductivity at 453 °C (0.00482 S cm^{-1}). At higher temperatures the conductivity is dominated for the electrical contribution to the overall conductivity. Structural refinements of these compounds are in progress based on a model derived from a complex intergrowth between the bismuth based fluorite-type layers and the chromium based CdI_2-type layers like observed from HREM images. The structural features of the $Bi_{17}Cr_8Sr_7O_{44.5}$ will be also investigated in a future work.

In summary, this manuscript presents several compounds which have been characterised as mixed conducting oxides. New oxides and new stacking modes have been identified and isolated in the Sr-Mo-O and Bi-(Sr)-Cr-O systems respectively. The latter results open the way to a new generation of layered oxides.